Università di Pisa

Dipartimento di Fisica
"E.Fermi"

Corso di Dottorato in Fisica Applicata

Ph.D. Thesis

Experimental study of stable propagation and efficient electron acceleration in plasmas with ultra-short laser pulses

Candidate: Andrea Gamucci

Supervisor: Prof. **Danilo Giulietti**

Contents

Acknowledgements

I would like to thank the people who helped and guided me for this work, in particular my PhD supervisor, Danilo Giulietti, and the whole staff of the Intensa Laser Irradiation Laboratory of CNR, Pisa. In particular, I'm indebted with Antonio Giulietti and Leonida A. Gizzi, who guided me with many fruitful advices. Moreover, I must thank Luca Labate, Petra Köster, Paolo Tomassini and Marco Galimberti, without whom the work would have been harder and much more difficult.

I have also to acknowledge the fruitful collaboration with the PHI (Physique à Haute Intensité) group at the CEA/Saclay Laser-matter Interaction Centre (SLIC) facility, in the framework of several experiments jointly conducted. Among the whole staff, to which I'm grateful for the nice collaboration, I'm indebted with Philippe Martin and Tiberio Ceccotti for their valuable scientific support.

I would like to thank also Jean-Raphaël Marquès and Nicolas Bourgeois of the LULI laboratory of the École Polytechnique for their efficient and expert contribution to the french experiments, Erik Lefebvre of CEA/CEA/Bruyères-le-Châtel for the PIC simulations and David Hamilton and Jean Galy of the Institute for Transuranium Elements of Karlsruhe for the nuclear activation measurements.

Last, but not least, I acknowledge the Istituto Nazionale di Fisica Nucleare (INFN) for the support of the experiments and the possiblity to attend several international conferences and symposia, in particular in the framework of the PLASMON-X Strategic Project.

Introduction

The new frontier of particle acceleration points to compact, room-sized accelerators able to counter the unsustainable expansion in terms of dimension and costs of standard radiofrequency-based facilities. Laser-driven electron acceleration in plasmas has been first proposed by Tajima and Dawson in 1979: a ultra-short and ultra-intense laser pulse that propagates in a plasma can excite high-amplitude plasma waves in its wake by means of its radiation (ponderomotive) pressure [1]. Such relativistic plasma waves can travel with phase velocity $\sim$ c and can sustain huge electric fields, with amplitude exceeding 1 TV/m: a charged particle that travels in phase with them can thus be accelerated to relativistic energies in millimetric distances. This process is called laser wake-field acceleration (LWFA).

The experimental demonstration of the feasibility of LWFA (in the following, electron acceleration will be principally considered) opened to a rapid boost towards record results in terms of gained energy, low energy spread and bunch emittance, driven by the scientific and technological progress in numerical modelization, laser system development and targets fabrication. Laser systems with peak power of hundreds of terawatt are now at disposal in several laboratories worldwide. However, beyond this kind of pushed-to-extremes research, there is a parallel class of experiments, performed with laser systems with peak power in the TW range up to a few tens of TW, that aims to investigate in detail the basic mechanisms of laser pulse propagation in plasmas and electron acceleration in the LWFA scheme. Results in this intermediate condition identify interesting regimes to be systematically explored, in order to enhance the total charge and the maximum energy of the produced electron bunches. Further, to become a stable tool in providing high-energy particles for many applications, laser-plasma based accelerators demand for a complete and detailed control of the mechanisms that rule the acceleration process. The major issues to be pursued are the stability and the operational reproducibility, as well as the tunability of the generated particle bunches characteristics in term of energy, energy spread, collimation and charge.

Two of the main tasks in this framework are: (i) the in-depth study of high-power laser pulses propagation in plasmas, aimed to optimize the excitement of

large amplitude plasma waves to extend the acceleration length beyond the so-called Rayleigh length, which is limited by optical diffraction; (*ii*) the injection of electrons in regions of the plasma associated with accelerating electric field and their efficient acceleration over many Rayleigh lengths.

In this work, the above mentioned tasks have been addressed through the detailed study of the interaction of ultra-short high-intensity laser pulses with underdense plasmas produced in gas-jets.

The thesis is organized as follows: chapter 1 introduces the basics of laser-driven acceleration of electrons, presenting a survey of the most recent results and of the advanced technique developed worldwide to optimize the LWFA. Chapter 2 presents the experimental results concerning the propagation of laser pulses with different intensity in subsonic helium gas-jets: the effects of precursors of the main laser pulse and ionization of the medium can deeply change the propagation of a 10 TW laser pulse, and can pre-form the plasma density distribution in a suitable way for acceleration purposes. Presented data are from an experimental campaign carried out at CEA Centre of Saclay (France) and from a former experiment performed at the Intense Laser Irradiation Laboratory of IPCF-CNR in Pisa (Italy). In chapter 3, results of a second experimental campaign carried out at CEA/Saclay, based to find conditions for efficient acceleration of electrons with a few tens of MeV, are shown. Finally, chapter 4 introduces a discussion on the application of a laser-plasma accelerator for medical radio-therapy of tumors and nuclear studies, in which advantages and limits are considered and some classes of usage are reviewed. The adopted techniques for the deconvolution of quantitative information from experimental data are described in appendix A for what concerns the ultra-fast interferometry of plasmas, and in appendix B for what concerns the measurements of electron bunches properties with an advanced spatial and spectral diagnostics.

The experimental campaign at the CEA/Saclay Laser-matter Interaction Centre (SLIC) facility have been performed in collaboration with the host PHI (Physique à Haute Intensité) group, headed by Philippe Martin, and has been coordinated by Antonio Giulietti (IPCF-CNR, Pisa). The acceleration experiment has been performed also in collaboration with J.-R. Marquès and N. Bourgeois of the LULI laboratory of the École Polytechnique (Palaiseau, France) and with J. Galy and D. Hamilton from the Institute for Transuranium Elements of Karlsruhe (Germany). The 3D-PIC numerical simulations presented in section 3.4 have been performed by N. Bourgeois and X. Davoine under the supervision of E. Lefebvre of CEA/Bruyères-le-Châtel (France).

Chapter 1

The laser-driven acceleration of particles: theory and experimental evidence

1.1 Introduction

The research in laser technology development has always been accompanied by the opening of new scenarios in the study of laser-matter interactions. Starting from the 1960s, a variety of scientific fields has benefited from the possibility to reach ever higher radiation intensities on target, capable of igniting processes of interest for atomic to nuclear and plasma physics, as well as astrophysics and fundamental interactions of particles.

An epochal breakthrough has been determined by the development of the so-called "chirped pulse amplification" (CPA) technique [2]. With this technique, laser pulses of few tens of femtosecond duration and intensity exceeding 10^{19} W/cm^2 have become accessible even in table-top laser systems. In a CPA-working laser system, a broadband, mode-locked oscillator produces a ultrafast pulse with femtosecond duration and energy of few nJ; then, the pulse is stretched by a pair of diffraction gratings, with the effect of lengthening the original duration by a factor of 10^3 to 10^5. In this way the input energy contained in the pulse is not affected, and neither is the fluence arriving on the amplifier medium, while the peak intensity is dramatically lowered. After the amplification, the pulse is finally recompressed in time to the initial duration by means of other two diffraction gratings. A sketch of the CPA process is showed

in fig 1.1. The CPA technology allows the overcoming of two major problems:

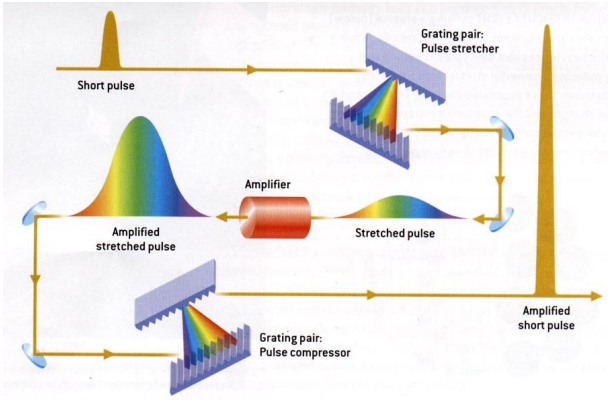

FIGURE 1.1: Operating principle of Chirped Pulse Amplification (CPA) of ultra-short laser pulses (from `http://www.eecs.umich.edu/USL/HERCULES/index/index.html`)

the damage of optical components in the laser chain and wavefront distortions of the pulse, which depend on the non-linear phase shifts experienced by the pulse in its passage through an optical device via the so-called B-integral:

$$B = \frac{2\pi}{\lambda} \int_0^L n_2 I dl \tag{1.1}$$

where $n_2 I$ is the intensity-dependent change in the refractive index. As an amplifier medium, titanium-doped sapphire crystal (Ti:Sa) offers a high gain bandwidth and therefore a narrow pulse width, and is by this time employed in nearly all the multi-TW high-power laser systems worldwide. Among the laboratories that are equipped with table-top terawatt (T^3) systems, it is worth naming Italy's INFN Frascati National Laboratories, in which a ultra-high intensity laser called FLAME (Frascati Laser for Acceleration and Multidisciplinary Experiments) will produce pulses with 6 J energy, 20 fs duration at 10 Hz repetition rate[1].

The huge electric field associated to a CPA laser pulse well exceeds the binding electric field E_b of a hydrogen-like atom, for which the threshold ionization intensity is:

$$I_{thr}^{ion} = \frac{c \cdot E_b^2}{8\pi} = \frac{c \cdot e^2}{8\pi \cdot r_B^4} \approx 3.4 \cdot 10^{16} \frac{W}{cm^2} \tag{1.2}$$

in which r_B is the Bohr radius ($r_B \sim 5 \cdot 10^{-9}$ cm). This is the case of above threshold ionization (ATI). However, it can happen that a laser pulse with lower intensity than I_{thr}^{ion} can ionize the target by means of different mechanisms. Multiphoton ionization (MPI) or optical field ionization (OFI, e.g. the case

[1] http://www.lnf.it/acceleratori/plasmonx/

in which ionization occurs via the suppression by the laser electric field of the potential barrier in which electrons are bound) can occur for laser intensities I$\leq 10^{14}$W/cm^2 or I$\leq 10^{16}$W/cm^2, respectively. The so-called Keldysh parameter Γ is used to discriminate among the two limiting nonlinear photo-ionization processes [3]. Γ is defined as:

$$\Gamma = \sqrt{\frac{E_i}{2 \cdot E_q}} \tag{1.3}$$

where E_i is the ionization potential for the given target and E_q is the oscillation energy acquired by an electron that experiences the ponderomotive potential associated to the laser pulse (called *quiver* energy):

$$E_q = \left\langle \frac{e^2 E_L^2}{2 m_e \omega^2} \right\rangle \approx 9.337 \cdot 10^{-14} I_{[W/cm^2]} \cdot \lambda^2_{[\mu m]} \tag{1.4}$$

. Equation 1.4, in which E_L is the laser electric field, ω is its frequency, m_e stands for the electron mass and the acute brackets denote a time average over one optical cycle, accounts for the oscillations that a detached electron starts immediately to do at the frequency ω of the electromagnetic laser field. When $\Gamma \gg 1$, ionization is predominantly driven by MPI, while for $\Gamma \ll 1$ OFI occurs in the very first optical cycles.

All present laser systems employed in plasma based acceleration experiment well exceed the ATI threshold of $\sim 10^{15}$W/cm^2 for the most commonly used gas species [4]. This implies that even in case of the front and rear edges of the pulse, their lower intensity with respect to the peak can be above threshold for ionization. This task has very important effects on the study of a high-intensity laser pulse propagating in a ionizing target.

Characteristic space and time scales of the plasma

For the description of the plasma medium, two different electric field regimes can be identified: the one relevant for the interparticle interaction (local field, driven by collisions among the single particles) and the one relevant for the global system (mean field). The discrimination among this two-fold description can be made considering as a limiting scale-length the distance over which the electric field of a charge is shielded by the surrounding distribution of charges. This distance is called "Debye length" and can be expressed as follows [5]:

$$\lambda_D = \sqrt{\frac{T}{4\pi \cdot n \cdot e^2}} \tag{1.5}$$

in which T is the plasma temperature in energy units, n is the particle number density and e is the electron charge. When the number of particles N in a

sphere with radius λ_D is much larger than 1, collective interactions dominate over interparticle interactions, and the plasma as a whole is distinct from a collection of charges. A system of charged particles that extends over linear dimensions $d \gg \lambda_D$ and such that $N \propto n \cdot \lambda_D^3 \gg 1$ is defined as *high-temperature plasma*.

A temporal scale parameter related to λ_D can then be introduced:

$$\omega_{pe} = \sqrt{\frac{4\pi \cdot n_e e^2}{m_e}} \tag{1.6}$$

where n_e is the plasma electron density and m_e is the electron mass. ω_{pe} is thus the plasma frequency, and describes the collective oscillation motion of the electrons in the plasma [6]. This behavior is ascribed to the global field action, while on the microscopic scale the local interparticle motion can be described by the collision frequency ν_c of the particles that undergo Coulomb deflections and scattering. It is worth noting that in the assumptions made before of $N \gg 1$ fits a variety of plasmas in real physical conditions, and imply that $\nu_c/\omega_{pe} \ll 1$ and so the plasma collective motion is dominant [7]. Table 1.1 summarizes the values of the cited parameters for a typical laser produced plasma.

n (cm^{-3})	T (eV)	ω_{pe} (s^{-1})	λ_D (cm)	$n \cdot \lambda_D^3$
10^{20}	10^2	$6{\cdot}10^{14}$	$7{\cdot}10^{-7}$	40

TABLE 1.1: Approximate magnitude of relevant parameters for a typical laser produced plasma [8].

1.2 Basics of laser-plasma acceleration of electrons

CPA-based, table-top laser systems provide pulses of peak intensity well above 10^{18} W/cm^2 and duration of tens of femtoseconds. The interaction of such a pulse with a plasma (often pre-produced by its raising edge via OFI or ATI of the target material) can excite electronic perturbations in its wake, displacing them to form an oscillating wave that can couple with the energy released by the pulse itself in its propagation [9]. In the so-called laser wake-field regime (LWF), first proposed by Tajima and Dawson in 1979 [1], large amplitude plasma waves can be resonantly excited by the ponderomotive force of an ultra-short laser pulse, provided its duration τ_L matches the condition:

$$c \cdot \tau_L \simeq \frac{\lambda_{pe}}{2}, \tag{1.7}$$

where c is the light speed and λ_{pe} is the plasma wave length ($\lambda_{pe} = 2\pi c/\omega_{pe} = \sqrt{\pi/r_e n_e}$ in which r_e is the classical electron radius and n_e is the plasma elec-

tron density). The electric field that is associated to plasma waves has two fundamental advantages: it is longitudinal and its amplitude can reach high values ($E_{pw} \geq 200$ GeV/m), it can thus be fruitfully exploited to accelerate electrons that can "surf" the excited waves in the wake of the propagating laser pulse.

In the following, the main aspects and challenging issues of the LWF mechanism for electron acceleration are introduced, including the enhancement of electron plasma waves in a laser field, the guiding of an ultra-intense laser pulse over long distances, the injection of seed electrons in the accelerating electric field and the requisites for an efficient plasma-based accelerator.

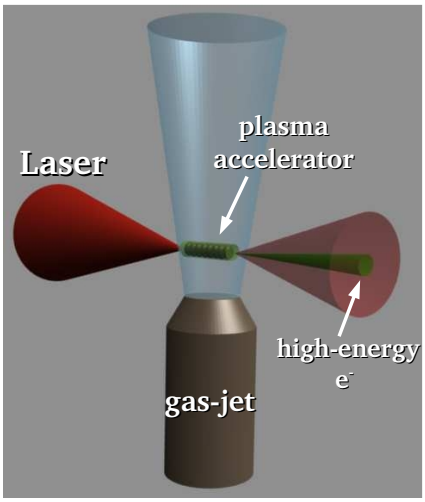

FIGURE 1.2: Sketch of a laser-driven acceleration process in a gas-jet target set-up

1.2.1 The wakefield issue

An analytical treatment of wakefield generation in laser-plasma interactions is possible only for up to 3D linear regime and for unidimensional nonlinear regime. The formulation of the problem in 3D nonlinear regime requires the use of numerical simulations usually executed on large parallel computer systems. The description of the laser wakefield generation issue can be done by using the cold fluid model of laser-plasma interaction, in which the plasma is assumed as fluid with zero temperature and the ions are assumed as immobile.
The laser pulse can be described by its vector potential:

$$\mathbf{A}(\mathbf{r}, t) = \Re\left\{\mathbf{A_0} e^{i\varphi}\right\} \tag{1.8}$$

in which $\mathbf{r}$ and t are the spatial and temporal coordinates, $\mathbf{A_0} = A_0 \hat{e}_\perp$ is the amplitude of the laser (for a linearly polarized pulse in the transverse direction),

and $\varphi = \mathbf{k} \cdot \mathbf{r} - \omega t$ is the phase. The laser electric and magnetic fields can then be expressed via the vector potential: $\mathbf{E} = -\partial \mathbf{A}/c\partial t$, $\mathbf{B} = \nabla \times \mathbf{A}$.
It can be useful to build a dimensionless field amplitude parameter $\mathbf{a}$ from the normalization of the vector potential, often used to establish a discriminating threshold between relativistic and non-relativistic regimes and to express the laser strength:

$$a_0 = |\mathbf{a}| = \frac{e|\mathbf{A}|}{m_e c^2}. \tag{1.9}$$

For a linearly polarized laser pulse, a_0 can be calculated from its peak intensity I and wavelength λ in a straightforward way:

$$a_0 \simeq 0.85 \cdot 10^{-9} \lambda[\mu m] \sqrt{I[W/cm^2]}. \tag{1.10}$$

The growth and excitation of plasma waves in the wake of an intense electromagnetic pulse results from the ponderomotive force exerted by the pulse on the particles in the plasma during its propagation. In the 3D linear regime ($a_0 \ll 1$), electrons in the plasma background experiencing the passage of an electromagnetic pulse oscillate with a quiver velocity $v_q = e \cdot E/m_e\omega = a_0 \cdot c$ (see eq.(1.4)), as the leading order equation of motion is $m_e \partial \mathbf{v_q}/\partial t = -e\mathbf{E}$.
At second order, expressing the velocity of electrons in the laser field as $\mathbf{v} = \mathbf{v_q} + \delta\mathbf{v}$, the equation of motion becomes [10]:

$$\begin{aligned} m_e \frac{d\delta\mathbf{v}}{dt} &= -m_e \left[(\mathbf{v_q} \cdot \nabla)\mathbf{v_q} + c \cdot \mathbf{v_q} \times (\nabla \times \mathbf{a})\right] = \\ &= -m_e \cdot c^2 \cdot \nabla \left(\frac{a_0^2}{2}\right) \equiv \mathbf{F}_p \end{aligned} \tag{1.11}$$

Here the expression for ponderomotive force F_p associated to the laser pulse is obtained, and one can see that F_p is related to the laser strength (intensity) via the parameter a_0. The ponderomotive force can be viewed as the gradient of the radiation pressure of an intense laser pulse, and acts on the background plasma electrons by expelling them from regions of higher laser intensity. The displacement of electrons from their rest position results thus in an oscillation of the plasma density and in the formation of a wake wave behind the pulse.

The ponderomotive force is more effective on electrons than on ions, because of the ions' greater mass. In the relativistic non-linear regime, the quiver velocity is corrected by the relativistic factor $\gamma = \sqrt{1 - v^2/c^2}$, so that $v_q = a_0 \cdot c/\gamma$ and the unidimensional ponderomotive force becomes $F_{p_z} = -(m_e \cdot c^2/2\gamma)\partial a_0^2/\partial z$.

The electric field associated to an electron plasma wave excited by the ponderomotive force of a high-intensity laser pulse is limited by a maximum threshold value. This value can be found considering the limit at which the electron trajectories in the wave mix (this condition implies that the electrons density

distribution departs from a sinusoid and reaches a singularity [11]), resulting in a breaking of the wave itself (*wavebreaking*). In the cold non-relativistic regime, this limit follows from the Gauss' law applied to the displacement $\xi(x_0, t)$ of a plasma electron from its initial position x_0 and it is found to be:

$$E_{wb}^0 = \frac{m_e v_p \omega_{pe}}{e} \tag{1.12}$$

in which v_p is the wave phase velocity. For waves that move with a phase velocity close to the speed of light c, relativistic corrections in the fluid motion equations have to be added. In this case, the Lorentz factor $\gamma_p = 1/\sqrt{1 - v_p^2/c^2}$ must be introduced and the corrected wavebreaking electric field amplitude becomes:

$$E_{wb} = E_{wb}^0 \cdot \sqrt{2(\gamma_p - 1)}. \tag{1.13}$$

It is worth noting that E_{wb} behaves like $\sqrt{n_e}$ and that for $v_p/c \ll 1$ eq. (1.13) turns back to eq. (1.12).

The evaluation of such a relativistic threshold value was first performed by Akhiezer and Polovin in 1956 [12] for the cold-fluid relativistic regime considering the Eulerian formulation of the problem. Few years later, Dawson demonstrated that the relation (1.13) could be obtained using Lagrangian equations [13, 14], and its 1962 paper was one of the firsts that reported results from computer simulations.
A very simple calculation using eq. (1.13) shows that, for a plasma with electron density of 10^{19} cm^{-3} and a laser pulse from a Ti:Sa system with 0.8 μm wavelength, $\gamma_p \simeq 13$ and $E_{wb} \simeq 1.5$ GV/cm.

From the experimental point of view, the difficulty of observation of electron density perturbations produced in the wake of a laser pulse relies on two main intrinsic aspects of the wake wave: (a) due to the microscopic size of such structures, the optical probing spatial resolution must be much better than λ_{pe} ($\lambda_{pe} \approx 10\mu$m for a plasma with electron density 10^{19} cm^{-3}); (b) due to their luminal velocity, the optical probe transit time through the region of interest must be much lower than the time the wake takes to propagate for λ_{pe}. Laser wakefield plasma waves have been observed experimentally with frequency-domain interferometry [15] and recently with single-shot, frequency-domain holography technique [16].

The value of γ_p, which can be also expressed as $\gamma_p \approx \lambda_{pe}/\lambda$, has implications on the shape of plasma waves: in the wake of laser pulses with $a_0 \gtrsim 1$, on the longitudinal axis the plasma wave is excited much more strongly than off-axis, due to the transverse intensity distribution of the driving beam (i.e. a Gaussian beam). On axis, due to the much strong relativistic quiver motion of the electrons making up the wave, the plasma frequency ω_{pe} is lower of a factor

$\sqrt{\gamma_p}$ with respect to off-axis regions, and consequently there is a dependence of λ_{pe} on the transverse coordinate as well. The wavefronts exhibit then a typical "horse-shoe" shape, being the curvature more accentuated farther from the driving laser pulse.

The curvature of plasma wavefronts is of capital importance in wavebreaking, electron injection and also for the focusing of the accelerated electrons. In fact, wavebreaking can be achieved even if the field associated to the plasma wave is lower than the threshold value of eq. (1.13), provided transverse wavebreaking occurs [17]. In this scenario, strictly dependent on the 2D feature described above, when the wavefronts curvature radius approaches the order of magnitude of the transverse displacement of electrons in the wave, the wake plasma wave breaks transversely. A number of electrons can be then injected into the accelerating region via this mechanism (see section 1.2.4).

1.2.2 The laser guiding issue

The more the laser pulse propagates in the plasma at the highest intensity, the more high-amplitude plasma waves are efficiently excited in its wake. For a Gaussian beam (here and in the following the considered laser beams will be assumed as Gaussian), the spot size $w(z)$ evolves with the longitudinal distance of propagation z as follows [18]:

$$w(z) = w_0 \sqrt{1 + \frac{z^2}{z_R^2}} \tag{1.14}$$

where

$$z_R \equiv \frac{\pi \cdot w_0^2}{\lambda} \tag{1.15}$$

is called "Rayleigh length" and defines the upper limit imposed by optical diffraction to the propagation distance of the radiation at the intensity it reaches in the focal region. For a tightly focused laser pulse, z_R constitutes a severe limit for the useful acceleration distance to very short values: $z_R \approx$100 μm for a 0.8 μm Ti:Sa laser pulse focused in a 5 μm spot. The majority of the LWFA experiments are then affected by this drawback, and the loss of intensity due to diffraction over z_R cannot be overcome by focusing the electromagnetic pulse in wider waists, because it would imply to use laser systems extremely more powerful and thus less affordable, in order to get the same intensity on target.

In laser-plasma interactions, the guiding of laser radiation over long distances is mainly a refractive guiding. As in optical fibers, if the index of refraction $\eta(\mathbf{r})$ of the medium exhibits a maximum on the longitudinal axis of propagation and a decreasing gradient in the transverse (radial) direction, i.e. $\partial\eta(r)/\partial r < 0$, then the medium can act as a waveguide, balancing the beam diffraction with the effect of a converging lens at the boundaries. This behavior is due to the

inward curvature of the laser pulse wavefront caused by such a refractive index profile, occurring when the phase velocity of the laser beam in the medium is lower on the propagation axis than off-axis. The phase velocity, in fact, depends on the index of refraction via the usual $v_\varphi = c/\eta(r)$ relation.

The index of refraction $\eta(\mathbf{r})$ can be evaluated as follows. The dispersion relation for the electromagnetic pulse in a homogeneous plasma is:

$$\omega^2 = k^2c^2 + \omega_{pe}^2 \tag{1.16}$$

From eq. (1.16) it follows that the maximum electron density for propagation, called "critical density", is $n_c = 1.1 \cdot 10^{21} \lambda_{[\mu m]}^{-2}$ cm^{-3} ($n_c \sim 1.7 \cdot 10^{21}$ cm^{-3} for 0.8 μm laser pulses). The group velocity of the radiation through the plasma takes the form:

$$v_g = \frac{\partial \omega}{\partial k} = c\sqrt{1 - \frac{\omega_{pe}^2}{\omega^2}} \tag{1.17}$$

Some general considerations can be sketched from eq. (1.13) and (1.17) regarding the optimum electron density value to improve the efficiency of the LWFA. Velocity and amplitude of plasma waves in the wake of a propagating laser pulse are critically affected by the value of n_e, with dramatic effects in the maximum energy achieved by the accelerated electrons. From eq. (1.13) it can be easily deduced that high values of n_e are requested in order to maximize the wavebreaking field amplitude E_{wb} and thus to achieve the highest accelerating gradients. Equations (1.17) in turn shows that the higher n_e, the lowest v_g, and thus the plasma waves travel with a lower phase velocity, that in the LWFA scheme is equal to v_g, limiting the energy gain by the electrons that can outrun them and dephase more easily. From the experimental point of view it is then mandatory to find a compromise between these two regimes: it is worth noting that the resonant n_e value for laser pulses of 50 fs duration is $n_e \approx 1.2 \cdot 10^{18}$ cm^{-3}.

From the dispersion relation (1.16), it follows that for small a_0 the index of refraction takes the form $\eta_0 = ck/\omega = \sqrt{1 - \omega_{pe}^2/\omega^2}$. This result can be generalized including relativistic effects and variations in the plasma density [19]:

$$\begin{aligned} \eta(\mathbf{r}) &= \sqrt{1 - \frac{\omega_{pe}^2}{\omega^2}\frac{n(\mathbf{r})}{n_0\gamma(\mathbf{r})}} \\ &\approx 1 - \frac{\omega_{pe}^2}{2\omega^2}\left(1 + \frac{\Delta n(\mathbf{r})}{n} - \frac{a_0^2(\mathbf{r})}{2} + \frac{\delta n(\mathbf{r})}{n}\right) \end{aligned} \tag{1.18}$$

The second row of eq. (1.18) has been obtained expanding the first row for small variations of electron density (Δn) and moderate relativistic effects, accounting for a change δn in density as wake response. Equation (1.18) shows that refractive guiding is made possible by either a plasma electron energy distribution that has a local minimum on the transverse direction of laser propagation axis, or a non-uniform transverse intensity distribution of the laser pulse. Effects of the plasma shape on guiding is implied by the first term in the expansion of eq (1.18), while the laser intensity profile enters through the second term in the expansion.
In the following, the two ways of guiding are briefly addressed.

1.2.2.1 Plasma waveguides

The index of refraction dependence on the electron density distribution can be exploited for laser guiding provided a hollow plasma channel is present along the laser propagation axis. The first remark to be made is that this hollow channel must be pre-existent at the moment of the arrival of the laser pulse in its focal region. From the experimental point of view, it means that not only the pre-ionization of the medium has to be taken into account, but also the hydrodynamic expansion that the ionization front provokes in the surrounding target regions. Furthermore, it is important to stress the necessity for the plasma to be fully ionized in order to avoid defocusing of the traveling radiation. In partially ionized plasmas, in fact, a propagating laser pulse with high intensity can further ionize the medium via optical field ionization, especially in the spatial regions in which its intensity profile peaks at the maximum value (the central region for Gaussian beams). This means that in this case the electron density would likely be enhanced on the laser propagation axis, building-up an opposite scenario of the required one for efficient guiding and thus contributing to defocus the laser beam.

The electron density distribution suitable for guiding a Gaussian laser pulse can be evaluated by solving the wave equation coupled with the index of refraction given by eq. (1.18). The matching condition for a laser pulse focused in a waist of size w_0 to be guided by a plasma channel with electron density depth Δn can be evaluated inserting in the wave equation a refractive index distribution that depends on a radial electron density profile of the form $n(r) = n_0 + \Delta n \cdot r^2/w_0^2$. This condition leads to the relation [20]:

$$\frac{4}{w_0} = \frac{1}{c^2}\frac{4\pi e^2 n}{m_e}\frac{\Delta n}{n} \tag{1.19}$$

that, in turn, gives the following relation between the spot size w_0 to be guided and the change of the electron density in the channel:

$$w_0 = \left(\frac{1}{\pi r_e \Delta n}\right)^{\frac{1}{2}} \tag{1.20}$$

in which $r_e = e^2/m_e c^2$ is the classical electron radius.

As a demonstration, the Maxwell's equation for an isotropic charge-free medium without losses has been solved for a dielectric constant $\epsilon(\mathbf{r}) = \epsilon_0 + \delta\epsilon(\mathbf{r})$, being $\delta\epsilon(\mathbf{r})$ the spatial variation induced by a shaped transverse profile. Expressing the electric field $\mathbf{E} = \psi(x, y, z, t)exp[i(kz - \omega t)]$ where k is the wavenumber in the propagation direction z, and separating the laplacian in its transverse and longitudinal components, it gives:

$$\frac{\partial\psi}{\partial t} = \frac{i}{2(1 + \delta\epsilon(r)/\epsilon_0)}\left[\frac{\partial^2\psi}{\partial r^2} + \frac{1}{r}\frac{\partial\psi}{\partial r} + \frac{\delta\epsilon(r)}{\epsilon_0}\psi\right]. \tag{1.21}$$

after separation of the temporal and spatial parts of the equation.
Equation (1.21) can be solved with a custom function for $n_e(r)$ (i.e. for $\delta\epsilon(\mathbf{r})$), in this case specifically with a parabolic profile. Considering the case of a laser pulse with 1 μm wavelength focused in a spot with w_0=20 μm in a plasma with electron density distributed as $n_e(r) \approx 5 \cdot 10^{14} \cdot r^2 + 4 \cdot 10^{18}$, the resolution of the wave equation yields the result plotted in fig. 1.3 for the intensity of the electromagnetic pulse. The intensity of the laser pulse in this case is contin-

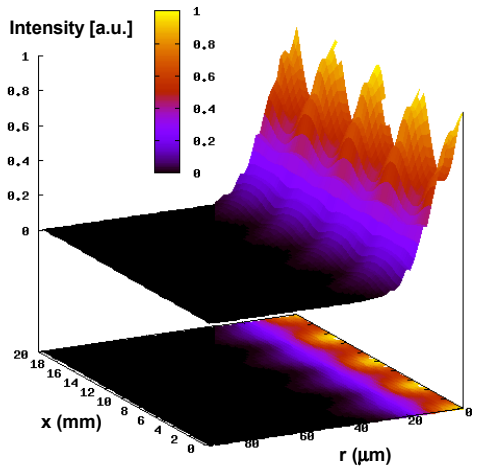

FIGURE 1.3: Results of the computation of eq. (1.21) with an electron density distribution of the form $n_e(r) \approx 5 \cdot 10^{14} \cdot r^2 + 4 \cdot 10^{18}$. The distance over which the calculation has been carried out is 20 mm.

uously decreased by the optical diffraction and subsequently increased by the re-focusing induced by the walls of the plasma hollow waveguide. The overall behavior is then the refractive guided propagation of the laser pulse.

Production of plasma channels in gas-jets constitutes a method of major importance, and has been widely investigated in the tuning of the interplay between laser pulse and target medium. Plasma channel guiding was first demonstrated by focusing with an axicon a first laser beam on a gaseous high-Z target and exploiting the hydrodynamic channel density depletion to guide a second beam over more than 20 z_R [21]. It is worth noting that the use of low-Z gases has enhanced the possible applications of such guiding technique, since a fully ionized medium can provide a more efficient propagation of an intense laser pulse in the channel avoiding energy losses in further ionization processes.
Furthermore, a "ignitor-heater" technique was first developed at LBNL laboratory (USA), which makes use of a first short pulse ($<$ 100 fs) to ionize a millimetric nitrogen or hydrogen gas-jet and of a second longer pulse (160 ps) to heat the existing plume via inverse bremsstrahlung [22]. This technique was introduced to show how a double pulse process can save the energy expense to generate the plasma channel with respect to a single pulse. The possibility to create a channel with a precursor laser pulse, prior to the arrival of the main accelerating pulse, can be also improved by the use of clustered gas-jets and the generation of a plasma waveguide with an ultrashort precursor pulse (70 fs). In this way the propagation of a femtosecond test pulse through the plasma waveguide has successfully been proved [23]. The method based on clustered gases has been extended to longer pulses (100 ps) with high efficiency, thanks to the high laser pulse absorption compared with the unclustered case [24].
A further very promising and exploited technique relies on the production of plasma channels in gas-filled capillaries. In such devices the ionization is induced via electric discharge through electrodes put at the edges of a thin tube containing low-Z gas. After the first experiments on glass-made devices, with the obvious drawback of single-shot operation due to capillary destruction after laser interaction but with promising results [25, 26], capillaries made up by two half-channeled joint sapphire blocks filled with gas and with electrodes placed near each end of the so-formed tube have become the device to be used to reach GeV electron energies [27]. When a capacitor discharges electric current through the electrodes, the contained gas is immediately ionized and shaped as a hollow-channeled optical fiber able to optically guide a propagating laser. The profile of the electron density for a forefront capillary device has been recently characterized by means of interferometric technique, showing also the possibility of tailoring the plasma profile to match efficient LWFA issues [28].

1.2.2.2 Relativistic optical guiding

The guiding effect can also be achievable exploiting the dependence of η on $\gamma(\mathbf{r})$ in eq. (1.18). Ponderomotive self-focusing in non-relativistic plasma has been first studied by Litvak [29] and Max et al. [30].

When the quiver motion of the electron in the plasma waves in the wake of an intense laser field becomes relativistic, the increase in their mass results in a decrease of ω_{pe} exactly as a depletion of n_e does in a plasma channel. Solving the wave equation with the index of refraction given by the second term in the expansion of eq. (1.18), a relation for the evolution of the laser spot size r_s with the longitudinal propagation coordinate z can be found [31]:

$$\frac{d^2(r_s/w_0)}{dz^2} = \frac{1}{z_R^2(r_s/w_0)^3}\left(1 - \frac{P}{P_c}\right) \tag{1.22}$$

where P is the laser pulse power and $P_c \simeq 17(\omega/\omega_{pe})^2$ GW is the so-called critical power for relativistic self-focusing. It then turns out that the laser spot size will focus provided that $P > P_c$. There is therefore a threshold value, analogous to eq. (1.20) for density, for the laser power in order to counterbalance the optical diffraction.

It has been shown that relativistic self-focusing is efficient for laser-guiding only in the case of long pulses compared to the plasma wavelength [32]. This is due to the fact that the index of refraction is modified in a time-scale of the plasma frequency ω_{pe} rather than in a time-scale of the laser frequency ω and, given that $\omega_{pe} \ll \omega$, the guiding effect is efficient only on the body of long pulses and ineffective for short pulses with length comparable to λ_{pe}/γ.
The effect of laser pulse duration on the relativistic self-focusing of a laser pulse with duration τ_L from 35 fs to 3 ps has been experimentally studied by Faure et al. [33], and the ineffective self-guiding for too short pulses ($\omega_{pe}\tau_L/\gamma$ <4.6) was demonstrated even for laser power greater than P_c. Recently, Chen et al. [34] confirmed this behavior exploiting a 100 TW laser system while, by accurately tuning the electron density of the plasma, successfully produced a ≈10 mm self-guided plasma channel.

1.2.3 Self-modulated LWA

It is by now an established trend in laboratories worldwide to perform "laser-into-gasjet" acceleration experiments in a range of plasma electron densities well above the resonant values, given the available and common laser pulse duration (n_e should be as low as $3{\cdot}10^{18}$ cm^{-3} for pulses with duration $\gtrsim$30 fs for the relation (1.7) to be satisfied). Also the experiments presented in this thesis are performed in conditions that make the acceleration scenario different from

the pure laser wakefield scheme. It is usual in fact that the laser pulse spatial extension L_l is several times the plasma wavelength λ_{pe}. However, depending on the laser duration and power and on the electron plasma density values, a regime in which the laser pulse self-modulates according to the period of the plasma waves that are excited after the passage of its rising front can be established. In a 1993 paper, the acceleration of electrons in laser-plasma interaction with $L_l > \lambda_{pe}$ and $P > P_c$ was theoretically demonstrated by Krall et al. [35]. Provided, in fact, that the condition for relativistic self-guiding is satisfied ($P > P_c$), a pulse with $L_l > \lambda_{pe}$ begins to excite a low-amplitude plasma wave in the wake of its rising edge, via the ponderomotive force. In turn, this wake field actively modifies the laser pulse propagation so that in the zones in which there is a lower electron density the relativistic focusing is enhanced by the channeling of part of the radiation, while the regions of higher n_e defocuses it. The overall result is then a modulation of the electromagnetic pulse at λ_{pe}, that with a feedback process contributes to enhance the waves in the wake.
Two considerations must be done concerning this regime of acceleration:

- when n_e becomes as high as requested for the above conditions to hold, the laser pulse group velocity in the plasma dramatically drops according to eq. (1.17), and this effect can represent a more severe limit on propagation of the laser pulse than optical diffraction;

- numerical simulations show that effective modulation of a 10 TW, 65 fs pulse happens in a plasma with electron density of few 10^{19} cm^{-3} over distances of the order of less than 2 mm (see section 3.4). This implies that guiding the laser pulse becomes mandatory to increase the accelerated electrons energy gain, since efficient wakefield excitation is possible once the pulse is modulated at about λ_{pe}

1.2.4 The electron injection issue

Once the acceleration principle is established, a problem arises concerning the injection in the pushing electric field of seed electrons to be accelerated. This quest is one of the most demanding, since even the layout of the accelerator depends on it. In fact, such electrons can be taken:

i) from the bulk plasma itself: it's the most common technique and it is usually referred to as "self-trapping";

ii) from an external source: for example a side-coupled linac matched to the plasma-based accelerator.

Despite the conceptual clearness of these two mechanisms, from the experimental point of view the precise control of the electron injection in the plasma waves

is really hard to achieve, because of either the highly non-linear nature of the wavebreaking process that is at the basis of the mechanism *i*) and the spatial and temporal constraints on the focusing conditions of an electron beam for the case *ii*).
In the following these two types of injection mechanism are briefly reviewed.

1.2.4.1 Electron self-trapping

When the electric field associated to a plasma wave exceeds the wavebreaking value expressed by eq. (1.13), the wave structure breaks and electrons in the rear part of its crest can be poured in the front direction, just as the sea waves behave on their approach to the shore. As we have seen in section 1.2.1, the two-dimensional effect of transverse wavebreaking can lower the threshold field (1.13), enabling the injection of a high number of electrons in the plasma wave.

As introduced in section 1.2.2, $\gamma_p = \omega/\omega_{pe}$ and some considerations can be drawn in the framework of particle injection due to wavebreaking: in case of high plasma electron density, small values for a_0 are required in order to satisfy the matching condition for E_{wb}. From a quantitative point of view, it means that for $n_e \approx 10^{19}$ cm^{-3}, $\gamma_p \sim 10$ and thus a laser pulse with a_0 of a few would be sufficient to break the wake wave and inject electrons. On the contrary, electron densities of the order of 10^{18} cm^{-3} would require much larger values of a_0 and hence much powerful laser systems. The drawback of this consideration affects the energy gained by the electrons, since small value of v_g means low phase velocity of plasma waves in the laser wake and in turn low energy for the tuned electrons. It turns out then that a compromise has to be established between the two regimes. Furthermore, a relation was experimentally found between the laser energy and the electron density for trapping to occur. It was observed that stable relativistic electron beams were obtained provided the plasma electron density and the laser energy exceeded a threshold condition: higher density required lower laser energy [36]. Using a simple model that does not take into account frequency shifts of the vector potential nor the change in the laser energy due to plasma electron density variations, the following relation is found:

$$E_{threshold}[J] = 23.3 \cdot 10^9 \left(\frac{n_c}{n_e}\right) a_{thr}^2 \tau_{FWHM}^{[s]} \tag{1.23}$$

in which a_{thr} is the threshold vector potential for self-trapping, found to be 3.2 by a best fit with the experimental data of ref. [36].

In this thesis experiments that falls in the first case will be presented, in which electron injection happens mainly from the bulk plasma background.

Injection is the starting step in the acceleration process for a given electron: in order to gain as much energy as the pushing wave can transfer to it, the electron must remain in phase with the wave for the longer time possible. A critical point in this framework is the matching between the initial electron velocity and the phase velocity of the plasma wave. In fact, as for a surfer that wants to ride an ocean wave, the particle must have an initial velocity that is not too small, otherwise it would slip back with respect to the wave, nor too large, otherwise the wave would be quickly outrun by the particle. There are then a minimum and a maximum value for the electron velocity that constitute the constraints for trapping by the plasma wave. In the linear regime, the plasma density perturbation δn can be expressed as:

$$\delta n = \delta n_e \sin(k_{pe} z - \omega_{pe} t) \ . \tag{1.24}$$

The Poisson equation $\nabla \cdot \delta\mathbf{E} = -e \cdot \delta n/\epsilon_0$ gives then for the electric field the relation:

$$\delta\mathbf{E}(z,t) = E^0_{wb} \frac{\delta n_e}{n_e} \cos(k_{pe} z - \omega_{pe} t) \ . \tag{1.25}$$

The problem of trapping in a plasma wave can be studied in 1D geometry considering the orbits of an electron in the phase space (γ, ψ), in which $\gamma = \sqrt{1 - v_e^2/c^2}$ is the relativistic factor associated to the electron energy and $\psi = k_{pe} z - \omega_{pe} t$ is the phase of the plasma wave described by an oscillating potential $\phi = \phi_0 \cos\psi$ as turns out from 1.25. With reference to Fig. 1.4, we see that trapping corresponds to the closed trajectories limited by the thick separatrix curve.

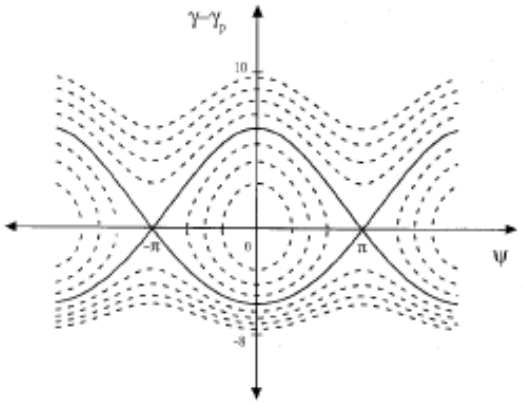

FIGURE 1.4: Electron trajectory in a plasma wave in the phase space (γ, ψ) for γ_p=20. The thick line represents the separatrix. Electrons have trapped trajectories inside the separatrix (closed orbits), and untrapped trajectories outside.

The minimum and maximum values for the electron γ are found to be:

$$\begin{aligned}\gamma_m &= \gamma_p(1+2\gamma_p\frac{\delta n_e}{n_e}) - \sqrt{\gamma_p^2-1}\sqrt{\left(1+2\gamma_p\frac{\delta n_e}{n_e}\right)^2-1} \\ \gamma_M &= \gamma_p(1+2\gamma_p\frac{\delta n_e}{n_e}) + \sqrt{\gamma_p^2-1}\sqrt{\left(1+2\gamma_p\frac{\delta n_e}{n_e}\right)^2-1}\end{aligned} \tag{1.26}$$

Open orbits represent the trajectories of such electrons whose γ is smaller than γ_m (that are overtaken by the plasma wave) or larger than γ_M (in which case they outrun the wave).

Available laser pulses hardly fulfill the relation (1.7) in terms of pulse duration (the high-density plasmas necessary for the self-trapping of electrons typically require sub 20-fs laser pulses for the relation to hold), but are so intense that they can excite in their wake a relativistic plasma wave via the onset of Raman forward scattering (RFS) parametric instability. In this scenario, the propagating electromagnetic wave decays into a forward propagating Stokes wave, an anti-Stokes wave, and a relativistic plasma wave. The beating of the laser electric field with the Stokes waves can eventually modulate the laser envelope, making it possible to be resonant with the plasma wave in the so-called self-modulated laser wakefield regime (SMLWF) [37]. In this framework, more than 10 years ago first encouraging results initiated the path towards the optimization of a laser-plasma accelerator [38, 39, 40]. Further progresses of laser science and the availability of laser pulses with duration of few tens of fs and suitable power, made then it possible to enter quasi-resonance regimes closer to the theoretical requirement (1.7). This led to enter the forced laser wakefield (FLWF) scheme of acceleration, allowing electrons with energy up to 200 MeV to be produced with 30 fs, 2-3 J laser pulses at LOA laboratory in France [41] and the enhancement of the electron yield with 1 J, $\sim$50 fs duration pulses at LBNL laboratory (USA) [42]. It has to be noted that most of these experiments have the common feature of poor quality of the electron beams. In the SMLWF regime, in fact, the laser pulse extends over several plasma periods, thus interacting with electron bunches accelerated by different plasma waves and degrading the output beam quality in terms of spatial collimation and monochromaticity. Even in the case of FLWF, the energy spread was found to reach values of approximately 100%, reducing the applicability of such high energy electron sources.

The first observation of monoenergetic beams from a laser-plasma accelerator rapidly followed the improved control of the plasma density, as well as the use of pre-formed hollow channels able to guide the laser pulse over several optical diffraction distances, and was reported by three groups from LOA, LBNL and RAL laboratories [43, 44, 45] in 2004. Energies of about 100 MeV in acceleration paths of the order of 1 mm have been achieved in supersonic gas-jets

targets, with energy spreads ranging from 2 to 24%.

Theoretical knowledge of the underlying physics has also grown with the experimental results and laser science development, providing numerical proofs and supporting simulations for different regimes of laser-target interaction. The pioneering work of Pukhov and Mayer ter Vehn [46] showed that a highly nonlinear acceleration regime is onset when a sub-10 fs, 20 mJ laser pulse propagates in a plasma with $n_e = 3.5{\cdot}10^{19}$ cm^{-3}, or a 33 fs, 12 J pulse travels in a plasma with $n_e = 10^{19}$ cm^{-3}. In these two cases, 3D particle-in-cell numerical simulations show that the pulse propagates leaving a hollow sphere in its back, on the rear side of which a bunch of electrons can accumulate pushed by the radiation pressure of the electromagnetic pulse. This alternative mechanism of electrons loading can yield energies of 50 MeV in the first case and 300 MeV in the second case. In this framework, monoenergetic electrons production has been demonstrated [47, 48]. The case in which the whole laser energy is trapped in a single filament, as the one discussed in ref. [48] is however unlikely to happen [49].

Alternative schemes for the injection mechanism have been proposed that concern wavebreaking, in order either to enhance the control on the process and to develop a scheme that does not imply the destruction of the accelerating structure, that on the contrary can happen in case of uncontrolled wavebreaking. A scheme in which only a portion of a plasma wave is interested by the breaking was proposed by Bulanov et al. [50], who demonstrated with 1D simulations that a gentle inhomogeneity in the longitudinal electron density profile of the plasma could provide breaking of the plasma wave and electron injection even well below the threshold (1.13). As introduced in section 1.2.1, in fact, wavebreaking occurs when the quiver velocity of the electrons in the wave is equal to the phase velocity of the wave. Furthermore, it can be shown that the plasma wave wave number depends on time through the relation $\partial k/\partial t = -\partial\omega_{pe}/\partial z$, in which k is the wave number and z the longitudinal coordinate. It then implies that an electron density downramp would contribute to lower the wave phase velocity thus favouring the wavebreaking condition (notice that the laser group velocity on the contrary increases, due to the lower electron density). Bulanov's work considered a transition scale length $L \gg \lambda_{pe}$ and demonstrated wavebreaking in the first plasma period behind the laser pulse and the subsequent trapping of the electrons in the second plasma bucket. Numerical simulation works related to this electron density transition scheme have been carried out also with 2D and 2.5D particle-in-cell codes for $L \leq \lambda_{pe}$ (sharp transition) [51, 52], and demonstrated the production of high-quality electron bunches.

As a comment for this technique, it must be said that the reduction of the plasma wave phase velocity represents a limit on the maximum energy that

an electron can gain if it is phase-matched with that wave. This means that this technique is not so much suitable for single stage experiments that aim to produce hundred of MeV (or higher) electrons, but could be an important first-stage injector of monoenergetic, ultra-short electron beams in possible following acceleration stages. This path has been considered very recently with the demonstration of controlled injection obtained focusing a 10 TW, 47 fs laser pulse on the downramp density gradient of a Gaussian-shaped gas-jet at LBNL [53].

1.2.4.2 External injection

An alternative technique for injection of electrons in the "plasma accelerator" relies on the utilization of a bunch of electrons originating from a conventional RF linac coupled to the laser-plasma device. As stated above, a set-up that involves a linac and a high-power laser requires a dedicated facility, so that this kind of experiments are quite hard to be carried out in laser-matter interaction laboratories worldwide. Moreover, given the possibility to dispose of such a particular arrangement, a number of experimental problems have to be overcome in order to create a competitive electron source. To date, the acceleration via laser wakefield of externally injected electrons with energy spread significantly smaller than 100% has not been successfully demonstrated in experiments [54, 55]. This is due to a series of constraints that must be satisfied in the production of the electron beam to be injected in the laser-plasma.

There are actually two main types of electron injection in a plasma wave capable of induce trapping of the particles and then efficient acceleration to ultra-relativistic energies. The first technique relies on sending in the laser produced plasma a packet of electrons whose $\gamma \approx \gamma_p$ at the right point within the plasma, in phase with respect to a accelerating electric field associated to a given plasma wave crest. The second way concerns sending an electron bunch with $\gamma \ll \gamma_p$ a little ahead of the laser pulse, in a way that, being overtaken by the laser wake, is then trapped in a subsequent plasma period.

Among the problems that, until now, have not come to a reliable solution, laser-plasma and accelerator experimentalists are facing the requests on the spatial extent of the seed electron bunch. In fact, in order to be injected in the accelerating region of a plasma wave travelling in the wake of an ultra-short laser pulse, the particle's bunch must have longitudinal dimensions smaller than λ_{pe}. Given that λ_{pe} is of the order of ten microns for a plasma with electron density of 10^{19} cm^{-3}, while in terms of transverse dimension, the optimum would be to dispose of electron bunches with extent of the order of the laser waist size w_0. A problem arises thus from the bunch lengthening caused by the space charge forces that repulse the electrons away from each other in such a tightly com-

pressed bunch. Present beamline accelerators are capable of focusing electron bunches in spots with size of at least 30 μm [56]. It has however been shown that the plasma wave itself can behave as a slicer for longer electron bunches that span over several plasma wave lengths [57]: in a theoretical work, Gordon et al. found that if a monoenergetic bunch of electrons extending over several λ_{pe} is injected in a train of plasma waves in the wake of a laser pulse, then the wakefield forces exerted by the plasma structures can phase-bunch the particle beam. Provided a fine-tuning between the electron energy and the plasma wave amplitude, this effect can affect up to the 50% of the original electron packet, the rest of which being radially expelled or overtaken by the plasma waves. It has to be noticed that with the present technology only less then 10% of the charge contained in a linac-produced bunch can be trapped by the wave.
A second problem regards the temporal synchronization of the electron packet with the plasma wave. In fact, nowadays RF-photogun technology is not capable of producing bunches with temporal duration of the order of sub-10 fs, that is the typical time-scale that comes at play in plasma-based acceleration experiments (a plasma density of n_e=10^{19} cm^{-3} implies that the plasma wave period T_{pe} $\simeq$40 fs). All the same, this selection of the proper injection phase can be relaxed in the scheme proposed by Gordon et al. [57], since the slicing effect of the plasma wave resulting from his simulations enables the use of electron bunches with duration higher by more than one order of magnitude ($\geq$100 fs).
Finally, when laser wakefield acceleration in gaseous targets (specifically supersonic gas-jets) in considered, further attention has to be paid to the density gradients at the vacuum-plasma boundaries, that can degrade the temporal, spatial and energetic uniformity of the externally incoming electron beam. This effect has been recently studied [58], and evidenced the possibility that a high-energy electron injected in a gas-jet can be scattered at the edge of the target region due to the variable wakefield experienced. As it will be shown in the next chapters, usual transition lengths for a gas-jet range from few to tens of hundreds microns. In this regions, electric and magnetic field can be generated with variable accelerating or decelerating features (that follows the increasing density toward the center of the jet), that can defocus the original beam. As a solution, the injection of the electron beam in the wakefield at an angle has been proposed in ref. [58]

The SPARC-PLASMONX facility for external injection experiments
As an example of facility in which a state-of-the-art linac is coupled to a high-power laser, it is worth mentioning the SPARC-PLASMONX facility at the Laboratori Nazionali di Frascati (LNF) of the INFN (Istituto Nazionale di Fisica Nucleare), Italy [59]. At LNF, in fact, the so-called FLAME (Frascati Laser for Acceleration and Multidisciplinary Experiments) laser system is under installa-

tion, while the SPARC linac is already operating.
FLAME is a >200 TW Ti:Sa laser system delivering pulses with duration <30 fs at 800 nm at a repetition rate of 10 Hz, and is characterized by a power contrast ratio of the femtosecond pulse to the nanosecond amplified spontaneous emission pedestal higher than 10^9.
The SPARC photoinjector provides high brightness electron beams with energy higher than 150 MeV for the investigation of free electron laser (FEL)-based experiments.

Most of the proposed program for both the systems relies on the synchronization of FLAME laser with the SPARC photoinjector laser, in order to have a temporal jitter between the radiofrequency and the ultra-short pulse below 1 ps. Besides the laser wakefield acceleration experiments with external injection, the set-up is conceived also for the creation of a Thomson backscattering source of tunable monochromatic X-rays (20-800 keV).
The main characteristics of both the FLAME-delivered pulses and the SPARC linac-produced electron bunches are summarized in fig. 1.5 (a) and (b).

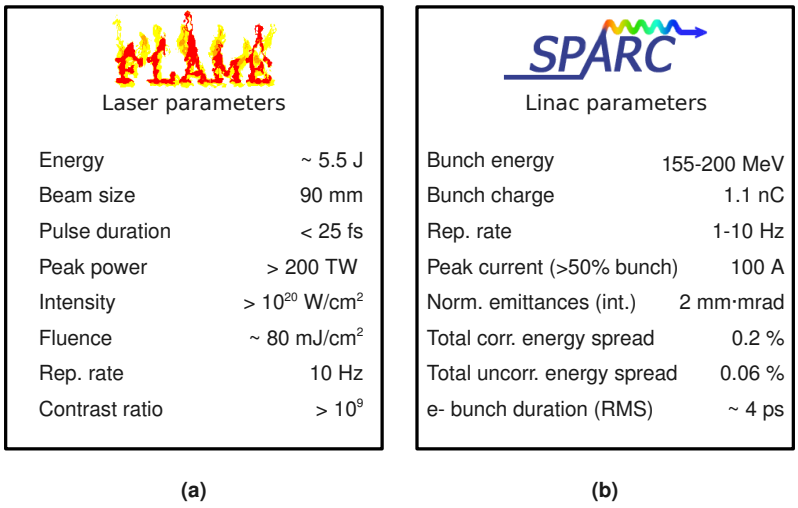

FIGURE 1.5: Main parameters for both (a) the FLAME laser and (b) the SPARC electron linac.

The schematic layout of the arrangement for the multiple beam lines coming from the linac is shown in fig. 1.6. The three RF linac sections send the beam, through a quadrupole triplet, a beam collimator and a first RF deflector, to a double bend dog-leg beamline that brings the electron bunches up to final focusing in the interaction regions.

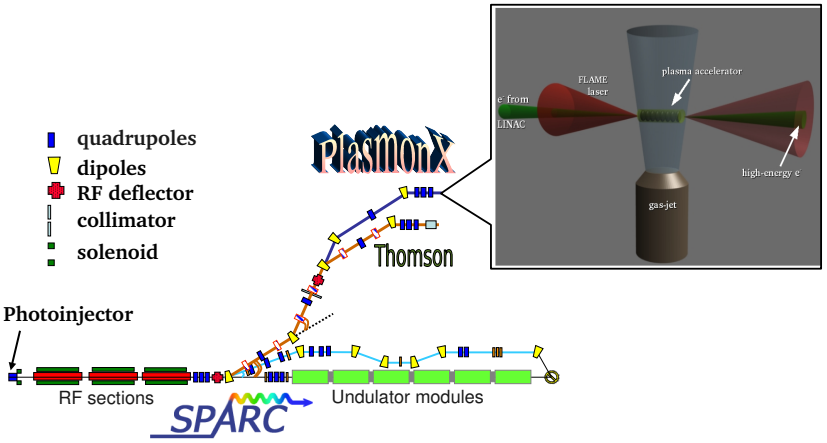

FIGURE 1.6: Layout of the arrangement for the multiple beam lines used for the SPARC linac and for the PLASMONX Project.

1.3 The design of an efficient laser-plasma accelerator

As pointed out in section 1.2.1, large amplitude electric fields associated to plasma waves excited by the passage of a short, intense laser pulse in a plasma exceed by several orders of magnitude the electric fields of the conventional RF-based particle accelerators. An electron that travels in phase with a plasma wave in the wake of the laser driver can thus gain a huge amount of energy in very short distances. It becomes then natural to start thinking about how to design a plasma-based accelerator to reach a high energy gain.

In section 1.2.4.1 the condition for electrons self-trapping in the plasma wave has been discussed with reference to the closed orbits in the phase space (γ, ψ), and the limiting relation for minimum and maximum electron gamma factor are expressed by eq. (1.26). An electron in phase with the wave gains thus the maximum energy when it is injected with the lowest possible energy for trapping (γ_m) and it is extracted from the wave with the highest gamma (γ_M). It follows from this consideration that:

$$\Delta W_{max} = (\gamma_M - \gamma_m) m_e c^2 = 2 \cdot m_e c^2 \sqrt{\gamma_p^2 - 1} \sqrt{\left(1 + 2\gamma_p \frac{\delta n_e}{n_e}\right)^2 - 1} \quad (1.27)$$

that in the limit of underdense plasma ($n_e \ll n_c$) reduces to:

$$\Delta W_{max} = 4 \cdot m_e c^2 \gamma_p^2 \frac{\delta n_e}{n_e} \ . \quad (1.28)$$

As an example, consider a fully ionized helium plasma with electron density of $2{\cdot}10^{18}$ cm^{-3} and a laser driver with wavelength λ_l=800 nm: in this case $\gamma_p \approx 30$ and the maximum energy gained by an electron reaches approximately the value of 1.8 GeV.

It turns out that laser-driven plasma accelerators provide a very promising alternative to standard particle accelerators, being competitive even from the point of view of final electron energy. The next step would then imply the design of custom-energy accelerating devices. In order to do so, there are however at least three problems to be resolved, which concern the underlying physics of laser propagation in plasmas and the phase matching of electrons with the accelerating electric field. These problems can be regarded to as "the three D's of laser accelerators" [60], namely:

1. diffraction of the laser pulse;
2. depletion of the laser power;
3. dephasing of the electrons with the wave.

Overcoming of issue 1. has been discussed in section 1.2.2. In order to design a reliable plasma based accelerator, it must be noted that current experiments demonstrate need for employment of a waveguide, rather than relying on laser self-focusing that is limited by an intrinsic lack of control due to its highly non-linear nature, and results thus inefficient for a stable device. Furthermore, optical guiding relaxes the constraint $P \gg P_c$ for relativistic self-guiding, opening to operation at lower intensities and thus more stable regimes.

The second issue to be considered, i.e. the depletion of the laser power, is due to the fact that the laser in its propagation transfers its energy to the plasma in the excitement of the plasma waves in its wake. When a significant part of the laser energy has been absorbed by the plasma waves, an efficient further excitation of the accelerating structure becomes inhibited, and the acceleration is highly limited. To evaluate the maximum distance over which the pump depletes, L_{pd}, it is sufficient to equate the energy in the driving laser pulse with the energy gained by the plasma waves left behind, $E_{wake}^2 L_{pd} = E_{laser}^2 c\tau_L$, obtaining [10, 61]:

$$L_{pd} \simeq \left(\frac{\omega^2}{\omega_{pe}^2}\right) \lambda_{pe} \cdot \begin{cases} a_0^{-2} & a_0^2 \ll 1 \\ a_0/3\pi & a_0^2 \gg 1 \end{cases} \tag{1.29}$$

in which $c\tau_L$ is the length of the laser pulse and the second part of eq. (1.29) results from the assumption of $c\tau_L \approx \lambda_{pe}$, following the resonance condition for

LWFA. It has to be noted that in case of $c\tau_L > \lambda_{pe}$, i.e. for experiments in which excitation of the plasma waves is obtained as consequence of laser pulse self-modulation (see section 1.2.3), the distance for pump depletion is higher, due to the fact that the energy absorption by the plasma from the laser pulse only begins when the self-modulation process is set-on.

The third limit to the acceleration process comes from the dephasing of the electrons with the plasma wave. As it was briefly introduced in section 1.2.4.1, as long as an injected electron gains velocity via the electric field associated to the plasma wave it is co-travelling with, it will eventually outrun the accelerating structure thus entering into a decelerating region, as it is shown by fig. 1.4. There is then a maximum distance an electron can travel remaining into an accelerating field region. This distance L_{deph}, called *dephasing length*, can be estimated considering the slippage of a particle that travels through a moving plasma wave half-length and the plasma wave itself: given the velocities of the particle ($\approx c$) and of the wave (eq. (1.17)), the relation

$$c \cdot \left[1 - \left(1 - \frac{\omega_{pe}^2}{2\omega^2}\right)\right] \frac{L_{deph}}{c} = \frac{\lambda_{pe}}{2} \tag{1.30}$$

is obtained. This expression gives then:

$$L_{deph} = \gamma_p^2 \cdot \lambda_{pe} \simeq \frac{a_0^2}{2} L_{pd} \ . \tag{1.31}$$

The dephasing length represents a lower limit for the acceleration distance, since it is clear that if the acceleration length for electrons is smaller than L_{deph}, no particle will gain as much energy as possible up to the maximum value expressed by eq. (1.27). On the contrary, if the acceleration length exceeds the dephasing length, trapped electrons begin to dephase with respect to the wave, but they can have gained as much energy as ΔW_{max}. Furthermore, it must be noted that the use of low plasma electron densities returns as a need to increase the electron energy, since L_{deph} grows with decreasing n_e.

From eq. (1.15), eq. (1.29) and eq. (1.31) it follows that the relation $z_R \ll L_{deph} \lesssim L_{pd}$ holds. To have an idea of the orders of magnitude of such quantities, consider a typical non-record laser-plasma experiments: for a laser pulse of 0.8 μm wavelength, $a_0 = 0.8$ focused in a spot with size $r_0 \simeq \lambda_{pe} \approx 15$ μm the propagation length are $z_R \approx 0.09$ cm, $L_{deph} \approx 0.53$ cm and $L_{pd} \approx 0.82$ cm.

In the acceleration experiment presented in this thesis (chapter 3), laser parameters were such that $a_0 \approx 1 \div 2$, so that the pump depletion and the dephasing lengths assume approximately the same value.

It turns then out that the acceleration distance is limited from below by the

Rayleigh range z_R over which the laser radiation has the maximum intensity without guiding, and is limited from above by the pump depletion length L_{pd}. As stated before, in case of self-modulation of the laser pulse to match the plasma wave length, the real value for these quantities increases. This means that the guiding of the laser radiation over distances that exceed the Rayleigh range by several times cannot be avoided in order for the injected electrons to reach higher energy.

1.3.1 The choice of the target

The dependence of the dephasing length on the plasma electron density follows from the relation (1.31):

$$L_{deph} \approx \frac{\lambda_{pe}^3}{\lambda^2} \propto n_e^{-3/2} \tag{1.32}$$

Being the laser-plasma acceleration process very critical on both laser driver and plasma medium intrinsic characteristics, target design and shaping is a major task in every experimental campaign. The precise control of the amplitude of target plasma's n_e, as well as its spatial profile and the overall dimensions can provide a useful tool in order to maximize the electron energy E_e, reduce the energy spread $\Delta E_e/E_e$, increase the number of electrons in the bunch (bunch current), extend the diffraction limited distance traveled by the focused pulse at high intensity. In order to achieve these improvements, several kinds of targets have been designed and tested. Among them, gas-jets, capillaries, and solids targets have up to now given important results.

Interaction of high-intensity laser pulse with supersonic gas-jets delivered by fast electromagnetic valves is the most common technique in LWFA experiments worldwide. This kind of target allows a uniform, underdense plasma to be the interaction medium, with a density that can be tuned by managing the pressure of the neutral gas in the reservoir. Furthermore, the interaction length can be increased or reduced by changing the dimensions of the gas exit slit, while fast valves enable high repetition rates and suitable synchronization with the laser pulse arrival. Injection of electrons in the plasma waves can moreover be improved by fine-tuning the laser interaction point with respect to the steep neutral density gradients at the gas entrance and exit edges.

Gas-jets enable also a quite custom shaping, provided the pre-ionization of the neutral gas by means of a precursor laser beam or of the amplified spontaneous emission (ASE) pedestal that usually precedes ultrashort pulses. High-quality electron bunches with $E_e \geq 80$ MeV and a few π·mm·mrad emittance has been obtained with a technique related to the "ignitor-heater" guiding scheme: one first laser pulse ionizes a hydrogen plume while a second pulse heat and shape the plasma where a third laser pulse creates the accelerating structure [62]. The same group has recently observed that focusing the laser pulse on

the downramp of a hydrogen gas-jet can reduce the accelerated electron bunches emittance to tenth of π·mm·mrad [53].

Monoenergetic electron production with $E_e \geq 200$ MeV has been demonstrated in gas-jets, by optimizing the value of n_e in order to find a relation between λ_{pe} and $c \cdot \tau_L$ in which the pulse duration is shorter than the plasma period and the plasma waves are bubble-shaped [47]. A technique of counter-propagating colliding laser pulses has been recently implemented in order to obtain a more efficient controlled injection of electron in a 2 mm helium gas-jet: it has been showed that with this technique electrons with E_e between 15 and 250 MeV, $\Delta E_e/E_e < 10\%$ and low divergence can be produced [63].

It must be said that, in terms of energy gain, a real progress to make plasma-based accelerators competitive with traditional RF-based facilities has been found in using gas-filled capillaries. With this kind of capillaries, developed at Oxford University, record electron energies of 0.5 and 1 GeV have been obtained with 12 TW and 40 TW laser pulses, respectively, in a 3.3 cm long capillary [27]. Guiding and high-energy gain acceleration has also been demonstrated in a 1.5 cm long sapphire capillary with 18 TW, 42 fs laser pulses, with achieved maximum energy of 500 MeV in a not stable repeatability and of 200-300 MeV in a more reliable way [64].

A minor but promising line of investigation concerns the use of plasmas pre-formed from thin foil targets, via the exploding-foil technique [65]. In this scheme, a thin foil of material, usually plastic of few micron thickness, is exploded in the interaction with the ASE pedestal. The main pulse interacts then with the pre-produced plasma enabling the onset of the LWFA mechanism. The choice of the thickness and material of the target, as well as ASE optimization, must then account for the possibility of producing a suitable plasma profile for acceleration and for the produced electron bunches not to be attenuated in their path forward.

1.3.2 The bubble regime and scaling to high energy

In section 1.2.4.1 it was mentioned that a 3D particle-in-cell simulation work evidenced the existence of a blow-out acceleration regime that is entered when the driving laser pulse longitudinal and transverse size are smaller than the plasma wavelength [46]. In this regime, provided the energy contained in the laser pulse is sufficiently high, the ponderomotive force exerted by the edges of the pulse expels electrons radially, creating a cavity with no electrons but only unshielded ions just behind the pulse. The expelled electrons accumulate at the borders of the cavity (called "bubble") and slip back with respect to the laser flowing into the crest of the first plasma period in the laser wake. At this point, those electron trajectories intersect with each others, leading to injection

in the first plasma bucket. This acceleration mechanism, although highly non linear in its nature, is found to generate a stable structure (the bubble) and able to generate ultra-short electron bunches with quasi-monochromatic energy spectra.

The bubble regime is entered when the laser pulse duration is shorter than the plasma wavelength, i.e. a pulse with 60 fs duration FWHM require a plasma density lower than or equal to $3{\cdot}10^{18}$ cm^{-3}. For higher plasma densities, this mechanism can however be achieved provided the laser propagation distance in the plasma is such to enable self-focusing and self-compressing of the driving pulse. Once more the need for optical guiding of the laser pulse emerges as a fundamental requirement.

In order to obtain scale-laws to extremely high energy and laser power, a twofold approach has been performed in the last three years. The first, temporally speaking, makes use of similarity analysis to get the scaling relations for electron energy, number and conversion efficiency of laser energy into quasi-monoenergetic electrons and was performed by Gordienko and Pukhov [66]. The second approach is based on the development of a phenomenological theory carried out by Lu and coworkers [67]. Each of these cases relies upon some assumptions that concern the laser strength parameter and the matching of its focusing conditions with the plasma parameters. These two cases are briefly reviewed in the following, with the relative retrieved scaling laws.

The similarity approach The theory developed by Gordienko and Pukhov is based on the following assumptions: ultra-high laser strength parameter $a_0 \gg 1$ (ultra-relativistic limit), very underdense plasma, focal spot size w_0 and laser pulse duration τ as large as $k_0 w_0 \gg 1$ and $\omega\tau \gg 1$, where k_0 and ω are laser wavenumber and frequency. If these hypotheses are satisfied and the similarity parameter $S = n_e/a_0 n_c$ is constant with simultaneous changes of laser strength and plasma density, then the laser-plasma dynamic is similar and the maximum energy for the quasi-monochromatic peak in the electron energy spectrum can be found to scales as:

$$E_e^{peak} \approx 0.65 m_e c^2 \sqrt{\frac{P}{P_{rel}}} \frac{c\tau}{\lambda} \tag{1.33}$$

where P is the laser power, $P_{rel} \simeq 8.5$ GW and λ is laser wavelength. Furthermore, the number of electrons in the peak is given by:

$$N_{peak} \approx \frac{1.8}{k_0 r_e} \sqrt{\frac{P}{P_{rel}}} \tag{1.34}$$

and the acceleration length is found to be:

$$L_{acc} \approx 0.7 \frac{c \cdot \tau}{\lambda} z_R \ . \tag{1.35}$$

The conversion efficiency of laser energy into electrons energy results: $\eta = E_e^{peak} N_{peak}/P\tau \approx 20\%$. The numerical coefficient in front of relations (1.33) to (1.35) are derived from theoretical simulation. It has to be noted that this analysis is valid for $a_0 \geq 2\sqrt{n_c/n_e}$ and is supported by simulations performed with values of a_0 ranging from 20 to 80, so are characteristic of laser-plasma interactions at extremely high intensity. However, they can provide a useful tool in the design of set-ups at large facility scale.

The phenomenological approach The phenomenological approach proposed by Lu et al. [67] takes advantage of the known relations for plasma waves excitation and beam loading in the wake of a high-intensity laser pulse, as well as pump depletion and electron dephasing lengths, to develop expressions of the same kind of the ones presented above. The assumptions that are at the basis of Lu's work are the following: quasistatic approximation (i.e. the laser envelope does not evolve significantly during its interaction with an electron), very underdense plasma ($n_e \ll n_c$), $a_0 \geq 2$, besides a laser waist matched to the bubble cavity ($k_p R \simeq k_p w_0 = 2\sqrt{a_0}$ where R is the radius of the hollow sphere behind the laser pulse). If these conditions are satisfied, then the energy gained by injected electrons (either self-injected or externally injected) is:

$$\Delta E_e[GeV] \approx 3.8 \left(\frac{P}{P_c}\right)^{-2/3} \frac{P[TW]}{100} \tag{1.36}$$

in which P_c is the critical power for relativistic self-focusing. The number N_e of electrons in the accelerated bunch is then found to be:

$$N_e \approx 2.5 \cdot 10^9 \frac{\lambda[\mu m]}{0.8} \sqrt{\frac{P[TW]}{100}} \tag{1.37}$$

and the acceleration length:

$$L_{acc} \simeq \frac{4}{3} \frac{\omega_0^2}{\omega_{pe}^2} \frac{\sqrt{a_0}}{k_{pe}} \ . \tag{1.38}$$

The difference of these formulas with respect to the ones in the paragraph above relies, according to ref. [67], in the scaling obtained for L_{acc}, since in the previous case the similarity theory predicts that the limit on the acceleration length is given by the plasma wavebreaking, in order to have the monoenergetic peak in the electron energy spectrum; in the phenomenological theory, on the contrary, the main limit to L_{acc} comes from the laser depletion.

Chapter 2

Studies on ultra-short laser pulses propagation in gas

Introduction

The effects, either linear or non-linear, that originate from the propagation of an ultra-short, ultra-intense laser pulse in a plasma stay at the basis of the mechanisms that rule the acceleration of electrons, as evinced from the previous chapter. The results attainable from a given experiment are as better predicted as better the propagation and evolution of the laser pulse in the target are comprehended. In order to perform experiment of particle acceleration in plasmas, several interaction parameters have to be well characterized, since in this way it become possible to obtain the interaction reproducibility. Generation of laser pulses with duration of tens of femtosecond, in fact, necessarily implies that several effects occurring in the complex laser chain can affect the final delivered pulse. One of the most relevant problems is the presence of one or more precursors in the temporal profile of the pulse. Depending on the ratio of the power of such precursors with respect to the peak power of the main short pulse (normally between 10^6 and 10^{10}), and considering that this latter is usually focused at intensities that easily exceed 10^{19} W·cm^{-2}, the intensity of the precursors can be well above the ionization threshold of the majority of targets (either solids or gases). This occurrence changes radically the scenario of the laser interaction with the target, since it can happen that the short femtosecond pulse interacts with a pre-plasma rather than the solid or gaseous medium. Obviously the interaction conditions also depends on the timing and duration of the precursor with respect to the main pulse, as the pre-formed plasma evolves prior to the high-intensity interaction. Furthermore, numerical codes exploited to model the wakefield acceleration (more frequently "particle-in-cell" or PIC [68] codes), do not have built-in interaction of laser emission prior to the main pulse nor ioniza-

tion of the medium, being able only to describe the interaction of the ultra-short intense pulse with a fully ionized plasma. This makes experimental results often surprising with respect to the numerical description of the process, as shown for example in the case of laser interaction with overdense plasmas [69]. In fact, even in the cases in which the pre-pulse action can be ignored, the ionization of the medium by the main pulse can deeply change its propagation due to self modulation and self defocusing caused by the fast change in the refractive index or generation of intense local electric and magnetic fields. More frequently, however, the "initial status" of the medium with respect to the intense pulse propagation has been "prepared" by the early interaction with the pre-pulse. A description of the origin of such precursors is given in the following, however it is possible to indicate three main kinds of pre-pulses: *i*) a sort of early "replica" of the main pulse due to the imperfect cut of the previous pulses produced by the laser oscillator (since a typical repetition rate if an oscillator is of the order of 50-100 MHz, the closest "replica" precursor precedes the main pulse by tens of femtoseconds) ; *ii*) the Amplified Spontaneous Emission (ASE) of radiation by the different elements in the laser chain, with a typical duration of a few nanoseconds and an amount of energy comparable with the main pulse, although at much lower power rate; *iii*) a picosecond pedestal which always precedes the main pulse due to the imperfect compression of the stretched amplified pulse at the end of the CPA system.

In this chapter, basic properties of the temporal quality of an ultra-short laser pulse are first briefly reviewed, then a study is presented concerning the interaction of ultra-short radiation with a subsonic helium flow from an electrovalve-controlled nozzle. In order to characterize the interaction of a typical ASE-like pre-pulse, an experiment has been performed at the Intense Laser Irradiation Laboratory of IPCF-CNR in Pisa (Italy) with a 3 GW laser system delivering pulses of 3 ns duration FWHM; the results are presented in section 2.2. The same gas-jet has then been used in a second experimental campaign, carried out at CEA Centre of Saclay (France), in which the effect of the ASE pre-pulse on the femtosecond main pulse propagation has been studied; results from this experiment are presented in section 2.3, as well as a numerical modelization of the interaction.

2.1 The temporal profile and contrast of femtosecond laser pulses

For first, it is worth to give a definition of laser "contrast ratio", for as it will be used in the following: with this term the ratio of the peak power of the main femtosecond pulse to the power of the preceding (the following ones are not

relevant for the main interaction) precursor pulses is indicated. These pedestals, which can be assumed as all the components in the delivered light but the main fs pulse, can have duration of a few nanoseconds down to femtoseconds. There are at least three main sources of such precursors:

1. oscillator background: the laser oscillator, typically running at repetition rate $\leq$ 100 MHz, can produce a replica of the main pulse due to the imperfect cut of the previous pulses by Pockels cells incomplete switching. This kind of prepulse usually precedes the high power pulse by at least 10 ns, and ordinary electro-optical cutting of this precursor reduces its energy to an extremely low level, so that it can be usually ignored. Typical contrast ratio: $>10^8$.

2. Amplified Spontaneous Emission (ASE): this kind of precursor originates from the amplification of photons by means of all the amplifying elements in the chain, and it is not directly associated with the main pulse, thus not having a spectral phase relation with the main pulse that would enable the compressor to temporally compress it. The time duration of a typical ASE prepulse is a *few nanoseconds* and, due to the progressive amplification in the laser chain stages, can carry as much energy as the main pulse, although at much lower power rate. Typical contrast ratio: $>10^6$ (up to 10^{10} can be achieved with special devices, like "plasma mirrors").

3. Imperfect compression of the stretched amplified pulse in the CPA system. This is due to the spectral dispersion introduced by the stretcher that, together with the dispersion introduced by the other elements in the CPA chain, cannot be perfectly recompressed by the compressor. These defects in the spectral phase result in a *picosecond pedestal* prior to the main pulse. Typical contrast ratio: $>10^3$.

2.1.1 Measurement of the laser pulse duration and contrast

Although it is of crucial importance for the comprehension of experimental results, the measurement of ultra-short and ultra-intense laser pulses is quite a hard thing to be performed. In fact, the request to monitor the different prepulses that couple with the main pulse is to have a high dynamic range over more than ten decades of laser intensity. Picosecond pedestal has to be studied with a good temporal resolution together with the need of resolving also the femtosecond principal pulse.

Because of the shortness of the laser pulses we are dealing with, there is no possibility to characterize the temporal and intensity shape of the pulse in a satisfactory way with photomultiplier tubes (whose resolution is limited to

fractions of nanoseconds) or optical streak cameras (that have not accurate resolution below 500 fs). It is therefore necessary to make use of an autocorrelation technique: the pulse waveform is retrieved by evaluating the correlation function of its intensity:

$$C_{2(3)}(\tau) = \int_{-\infty}^{+\infty} I^{(2)}(\tau) I(t+\tau) dt \tag{2.1}$$

Second order autocorrelation (C_2) has been widely used in order to measure the pulse amplitude and phase [70], but it presents an ambiguity in time direction and a relatively small dynamic range. Third-order autocorrelation overcomes those problems, making it possible to determine the front and rear profile of the pulse intensity by introducing asymmetry in the function C_3, and also allowing a large dynamic range to be investigated. The nonlinear $I^2(t)$ factor in 2.1 is produced by means of second harmonic generation from $I(t)$ in a nonlinear crystal (for example, standard BBO crystals are commonly used), while the correlation is provided by sum frequency mixing in the same crystal [71].

One experimental feature that is relevant for the majority of experiments is the possibility to perform pulse characterization measurement on single-shot basis. This is mandatory when trains of pulses have to be characterized at high repetition rates.

The electric field associated to a laser pulse can be expressed as a mono-dimensional complex function of either time or frequency. Among the techniques that have been developed to measure the shape of ultra-short laser pulses, some are based on the construction of two-dimensional experimental trace while others rely on mono-dimensional trace reconstruction. Depending on this difference, it is possible to recognize two main classes of techniques: a spectrography-based one and an interferometry-based one.

Spectrographic techniques consist in measuring the time-frequency representation of the pulse, and reconstructing the analytic signal of the pulse by means of an iterative algorithm from the experimental trace. An example of this technique is Frequency-Resolved Optical Gating (FROG) spectrogram [72]. In a FROG measurement, the signal from the autocorrelator is spectrally resolved, so that instead of measuring the energy as a function of time (as given by the autocorrelation), FROG gives the signal spectrum versus time by adding a spectrometer to an autocorrelator.

On the other hand, there is a class of techniques based on the measurement of interference between different frequencies in the pulse spectrum. In this case the experimental trace is mono-dimensional and the inversion algorithm is noniterative. This is the case of Spectral Phase Interferometry for Direct Electric-field Reconstruction (SPIDER) [73]. In SPIDER measurements two replicas of the input laser pulse are generated and time delayed with respect to each other. Then, they are frequency mixed with a stretched pulse in a Type II nonlinear crystal, resulting thus spectrally sheared from each other. The

interference between this pair of pulses is recorded by a spectrometer followed by an integrating detector.

2.1.2 Pulse cleaning: the plasma mirror

In order to reduce the level of the nanosecond and picosecond pedestals, there are two main options: the first relies in the improvement of the optical components of the laser chain, i.e. to reduce the spontaneous emission (to limit the ASE) or to better the compression of the spectral phase, while the second relies in the production and insertion in the laser chain of external devices to actively modify the produced pulse by means of non-linear filtering, i.e. saturable absorbers or "double CPA" [74, 75]. The second option includes the so-called "plasma mirror" (first proposed by Kapteyn at al. [76]): it uses a thin dielectric layer onto which the femtosecond pulse coming from the compressor impinges. After focusing, the pedestal is transmitted through the material, while the main pulse is reflected by the super-critical plasma created at the device.

The fact that the plasma mirror is conceived to be placed after the compressor, on the pulse way to the target, makes it non-invasive with respect to the whole laser chain.

The main tasks for this device concern then the need to keep the initial reflectivity as low as possible, so that the precursor can be transmitted away, and final reflectivity as high as possible, in order to have the maximum energy in the laser pulse after the plasma mirror. Furthermore, the dielectric plate has to be moved after each shot, requiring the synchronization of laser shots and of the mirror positioning system to be as accurate as possible in order to exploit a high repetition rate effectiveness. Most of the practically used plasma mirrors is used on a single-shot basis and reduce the pulse energy by roughly the 50%.

2.1.2.1 A practical implementation of plasma mirror: the UHI10 laser system at CEA/Saclay

As an example of laser systems that employs the advanced technique of plasma mirrors to temporally clean the pulse, the Ultra-High-Intensity 10 TW laser system (UHI10) that has been operative from 1997 to 2008 (before the upgrade at 100 TW) at the Saclay Laser-matter Interaction Centre (SLIC) of Commissariat à l'Énergie Atomique (CEA) in Saclay (France) is presented. The same technique is presently used on the new 100 TW laser.

UHI10 is a CPA-based Ti:Sapphire laser system delivering pulses on two beams at a wavelength of 800 nm and at a repetition rate of 10 Hz. The oscillator delivers pulses with 30 fs duration and energy of 3 nJ with a spectral band of 45 nm. The stretcher then lengthen the pulse up to a duration of 300 ps such as it can be amplified in the following stages. Of the two beams, one is called in the

following "main" and is the high-power one used for the principal interaction with the target; the second is called "probe" and is a lower power beam. Of the total 4 amplification stages, the first one is a regenerative amplifier: it allows the main pulse to attain an energy of 3 mJ; then a fast Pockels cell extract a single pulse. The following three are multi-pass amplifiers that give the main pulse an energy of 1.5 J. The 300 ps pulse is then compressed to 60 fs by the compressor, that is kept under vacuum. Given the total transmission of the

FIGURE 2.1: Photograph of the compressor under vacuum of the UHI10 CPA-based laser system (from `http://iramis.cea.fr/femto/slic/index.php`).

system of approximately 50%, the final delivered main pulse has a duration of 60±10 fs and an energy of 750 mJ, so that the peak power exceeds 10 TW. The probe is a 50 GW pulse usually employed to probe the plasma created by the main or to create harmonics in gaseous targets, and it is synchronized with the main. The peak intensity reached with an off-axis parabola with f=200 mm exceeds 10^{19} W·cm^{-2}.

The plasma mirror was built up by a thin plate of glass with anti-reflection coating. The contrast ratio for the main pulse of UHI10 was measured with a third order autocorrelator, namely Amplitude Technologies' SEQUOIA that up to 10^{12} dynamic range and a temporal delay of more than 500 ps. The result is shown in fig. 2.2. As it is evident, the contrast ratio of the main pulse is approximately 10^5 at 2 ps and $7{\cdot}10^5$ at long delays, while the contrast is increased by more than two orders of magnitude (approximately by a factor of 150) by the plasma mirror [78]. It is worth noting that, as introduced in the previous paragraph, a third order autocorrelator is capable of detecting an asymmetric shape of the laser pulse, as it is the one emerging from the plasma mirror after the cleaning.

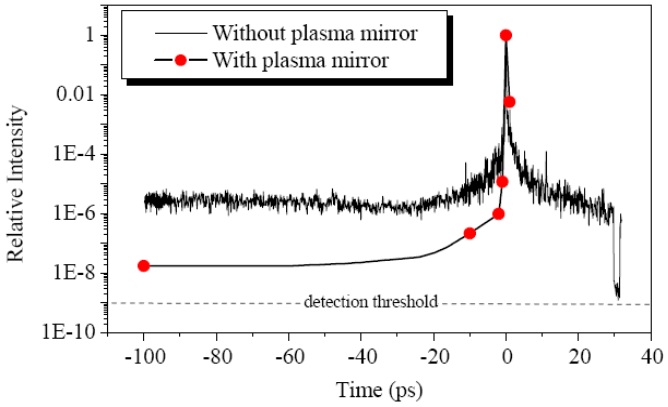

FIGURE 2.2: Temporal profile of the UHI10 pulse without (red curve) and with (triangles) the plasma mirror [77].

In order to prevent the ASE pedestal of UHI10 delivered pulses to damage the samples when focused very tightly to perform experiments on high-order harmonics generation, a dramatic increase of the contrast has been obtained recently at SLIC facility with the implementation of a second stage of plasma mirror added to the first one, by means of employment of two consecutive reflections on a set of parallel dielectric plates. The trace resulting from the cross-correlator is shown in fig. 2.3 [79]: the ASE pedestal starts from a level of 10^{10} and reaches a level of 10^{2} at 2 ps, while in the previous case, with the single plasma mirror, data for the same delays were 10^{8} to 10^{6}.

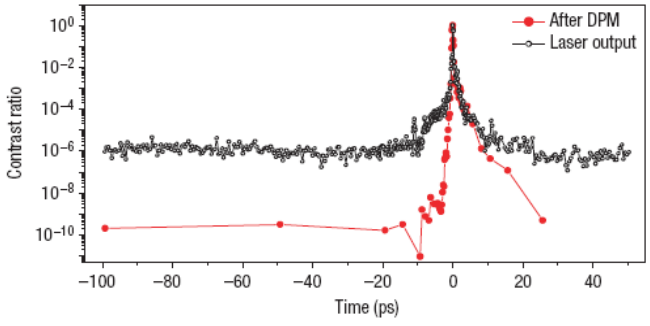

FIGURE 2.3: Temporal profile of the UHI10 pulse without plasma mirror (black line) and with the double plasma mirror (red line) [80].

2.2 Experimental study on plasma channels formation in gas-jet

This section presents an experiment devoted to the characterization of the plasma created via the interaction of a low-intensity, nanosecond laser pulse with a subsonic gas-jet. The goal of the study was to systematically describe the plasma and its temporal evolution in different conditions of laser-gas interaction, in order to explore the behavior of the ionized medium following its creation by an ASE-like laser pulse. As pointed out in the previous chapter, for a laser pulse to fulfil the quasi-resonance condition 1.7, its duration has to be of the order of tens of femtoseconds. However, the preceding nanosecond pedestal due to ASE, whose intensity is several orders of magnitude lower than the high intensity one, interacts with the target medium few nanosecond prior to the arrival of the short pulse. Furthermore, the peak intensity of laser pulses commonly employed in acceleration experiments likely exceeds 10^{19} W·cm^{-2}, while the ratio to the ASE intensity for systems with no cleaning devices is typically of the order of 10^6. It follows that an ASE pre-pulse intensity of 10^{13} W·cm^{-2} is by far above the threshold for gas breakdown, so that the short femtosecond pulse usually propagates in a pre-formed plasma rather than in a gas. Such a plasma has the time to hydrodynamically evolve, and its evolution can be used to make the plasma as suitable as possible for an improved propagation of the main pulse and consequent efficient acceleration.

The results presented here are oriented to find the most suitable conditions to improve the acceleration length [81, 82]. To this purpose we use the well established data [83] on optical gas breakdown by laser pulses and subsequent evolution of the plasma. To do so, an experimental arrangement to probe the laser-gasjet interaction with a fast inteferometric technique was set-up at the Intense Laser Irradiation Laboratory of IPCF-CNR in Pisa (Italy). The description of the experimental components and layout is presented in the next paragraph.

2.2.1 The experimental set-up at Intense Laser Irradiation Laboratory of IPCF-CNR

The laser system employed to study the plasma evolution driven by an ASE-like laser pulse is a 3.3 GW Nd:YLF delivering two beams with maximum energy of 5 J per beam at a wavelength of 1053 nm and duration of 3 ns FWHM. The system can provide intensities up to $10^{15} W/cm^2$ on target with a high temporal and spatial quality.The laser works in single mode both longitudinally and transversely. One of the two beams is used for the interaction with the target, while the other is used for interferometry. As a nomenclature, the first

will be called "main" and the latter "probe". The scheme of the arrangement of optical components for the experiments is shown in fig. 2.4. The probe beam is

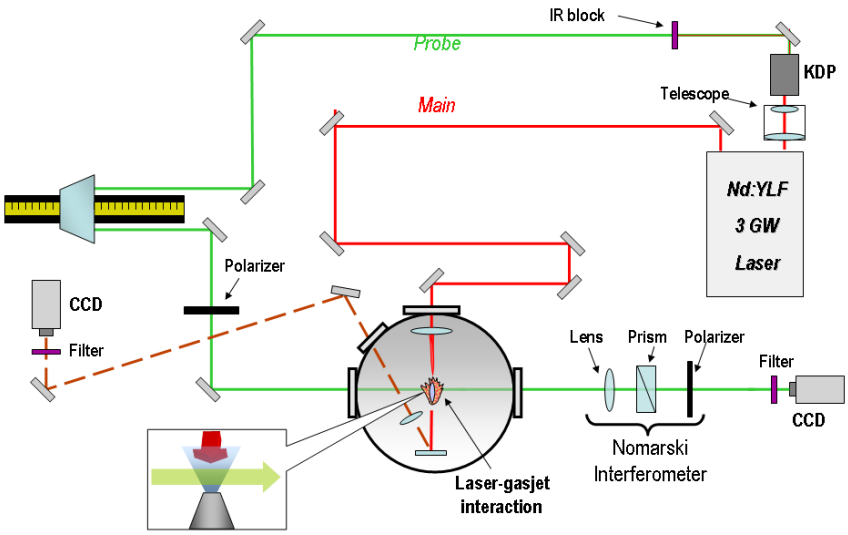

FIGURE 2.4: Experimental arrangement for the plasma channels characterization at ILIL lab of IPCF-CNR. Inset: sideview detail of the interaction region.

frequency doubled by a KDP-type crystal, so that $\lambda_{probe} = 527$ nm and is filtered from any remained infra-red fraction of the pulse. In order to probe the evolution of the plasma at different delays with respect to its creation by the main pulse, the probe beam is sent on a sliding guide mounted on millimetric graduate reference. The probe beam crosses then the sample in orthogonal direction with respect to the main pulse propagation direction, and enters the interferometer set-up, after which is imaged on a CCD camera. The interferometer is built in Nomarski configuration, and will be explained in detail in subsection 2.2.2. The transmitted main pulse is also imaged on a CCD camera in order to monitor the equivalent focal plane, and to image the position of the laser focus with respect to the target. In this study, in fact, a careful control on the laser point of interaction with the gas is needed to systematically characterize the produced plasma.

The main pulse is focused on the target with a $f/8$ lens, and the resulting focal spot is almost elliptical with semi-axis of dimension (5.2 ± 0.2) μm and (6.0 ± 0.2) μm. It implies that the Rayleigh length in this case is $z_R \approx 100$ μm. In order to have an intensity for the main pulse that is of the order of $10^{13 \div 14}$ W·cm^{-2}, the energy of the laser pulses was set in the range 0.3 J to 0.5 J by tuning

the system's amplifiers. For what concerns the intensity of the main beam, it implies that, given the fraction of energy actually reaching the target is of the order of 80%, the intensity on target is approximately $1.4 \cdot 10^{14}$ W·cm^{-2}.

2.2.2 The Nomarski interferometer

The interferometer employed in the experiment is a polarized light interferometer (named Nomarski after the first who proposed it [84]), in which two cross-polarized beams give a completely separated interferometric images [85]. The interferometer is made up of two polarizers, a lens and a Wollaston prism; a scheme for the Nomarski configuration of these optical components is shown in fig. 2.5. The incoming probe beam is firstly linearly polarized by the polarizer

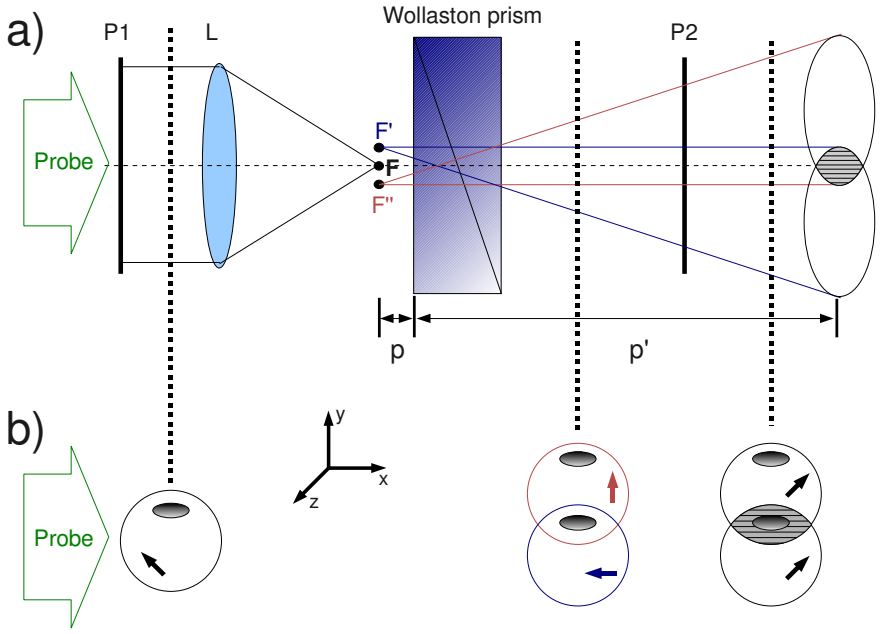

FIGURE 2.5: Scheme of the Nomarski interferometer. a) Arrangement of optical elements; b) sections of the probe beam at different positions in the layout with polarization indicated.

$P1$, and then is focused by the lens slightly before the prism. The incoming beam is splitted by the Wollaston prism, which is formed by two identical triangular prisms of bi-refringent crystal, tied together to form a parallelepiped. The optical axis of the two crystals are orthogonal to each other and to the probe beam propagation direction. The incident light on the first prism is refracted in two co-propagating ordinary and extra-ordinary beams, which swap their nature in the passage in the second prism and exit at different angles from the

Wollaston device. The two outcoming beams are orthogonally polarized with respect to each other, thus the second polarizer $P2$ (whose axis is oriented in a intermediate direction) makes the two polarizations be collinerar. The fringe pattern originates then from interference of the superposed portion of the two beams that can be imaged on the detector. Using basic optics, a relation between the distances of the optical elements can be found in order to optimize the quality of the recorded interferograms. With reference to the coordinate system indicated in fig. 2.5, and calling p the distance of the focus F from the Wollaston prism and p' the distance of this latter from the detection plane, it follows that the position of the intensity maxima on the detector plane are [86]:

$$y_n = n\frac{(p+p')\lambda_{probe}}{d} \tag{2.2}$$

in which d is the distance between F' and F''. Denoting with α the angle between the outgoing beams from the Wollaston prism, the interfringe distance on the recorded interferogram is:

$$l = y_{n+1} - y_n = \frac{(p+p')\lambda_{probe}}{d} \simeq \frac{p' \cdot \lambda_{probe}}{\alpha \cdot p} \ . \tag{2.3}$$

The Nomarski interferometer can be used at different wavelengths, since Wollaston prism, usually made up of calcite or quartz, is transparent in the range 180-4500 nm. Furthermore, the identical optical path for the beams originating in the prism (F' and F'' are equidistant from F) makes it suitable for use with optical probes whose duration is ultra-short, while the in-line layout makes the alignment easier than for other interferometers.

2.2.3 Gas-jet and pump-probe parameters

The subsonic gas-jet used for the experiment has been provided by the PHI group of CEA/Saclay (France). In order to produce the high-density gas column (up to 10^{20} cm^{-3}), a stainless steel, high-speed solenoid valve was developed by the Saclay plasma group. The valve could operate at 10 Hz repetition rate with backing pressure up to 20 bar, and was activated by an external circuit composed of a 110 V voltage supply coupled to a generator of TTL signals. The duration of the delivered TTL signal sets the opening duration of the electro-valve, which was estimated to be 10 ms FWHM. The gas-jet density distribution coming from different nozzles coupled to this kind of electro-valve has been formerly characterized in detail with fast interferometric techniques [87, 88].

In the following description, I will present results obtained with a rectangular slit nozzle with dimension of 3 mm in length and 0.3 mm in width.
Due to the subsonic nature of the gas-jet, the gas expands well beyond the size of the slit after its exit from the nozzle. It will be evident from the plasma mapping presented in the next sections. A schematic view of the interaction

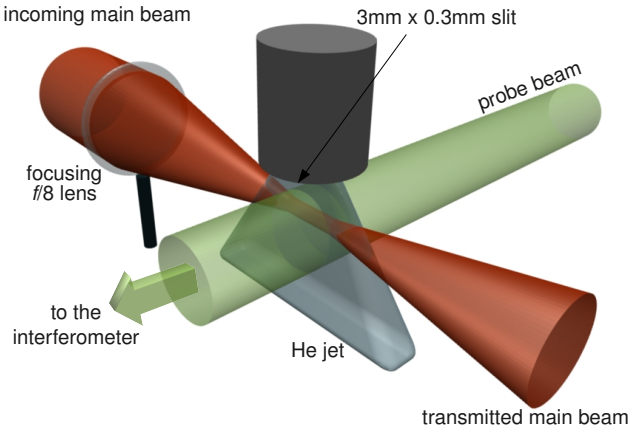

FIGURE 2.6: Scheme of the interaction region with the propagating main and probe pulses.

is shown in fig. 2.6. The gas used in the experiment is helium, whose backing pressure varied from 5 to 8 bar.

The delay line built on the sliding guide shown at lefthand side of fig. 2.4 enabled data-taking at different moments from the creation of the plasma, to follow its evolution with time. However, in the following, data obtained with 5 ns delay between the arrival on focus of the main pump laser pulse and the probing by the frequency-doubled beam will be presented. With this value of time delay, it was possible to achieve the maximum quality of interferograms and the best reproducibility of the plasma profile.

For what concerns the geometry of the interaction region, the pump laser beam axis was set to be in the longitudinal symmetry plane of the gas-jet. Interferograms were recorded for different positions of laser focus with respect to the nozzle slit, ranging from the entrance to the exit of the gas-jet. Figure 2.7 shows the coordinate system adopted to describe the interaction point between the main beam and the gaseous target.

In the following, data related to focal positions $x = -1$ mm, $x = 0$ mm and $x = +1$ mm are presented, while the laser beam axis was set 500 μm away from the slit plane. In the spatial frame of fig. 2.7, the probe beam is directed along the y axis.

2.2.4 Experimental results from Pisa experiment on ns pulse propagation

Among the huge number of collected interferograms, in the following the ones relevant to the best interaction conditions are presented. From the experiment,

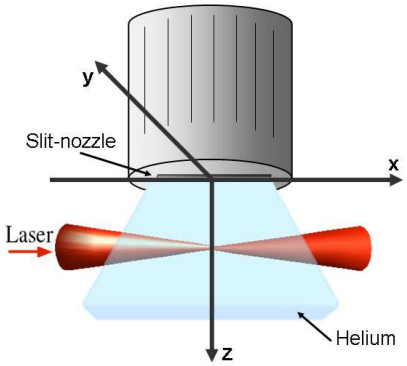

FIGURE 2.7: Gas-jet and laser focusing geometry. The focus of the main beam has been shifted from the center towards both the entrance and the exit of the gas-jet through the experiment. The coordinate system adopted is also shown. The probe beam, not shown in figure, propagates along the y axis. The gas expansion angle from the slit is merely indicative.

it results that a small plasma is initially produced by optical breakdown in the gas nearby the focus; then the plasma expands along the laser propagation axis. This expansion is due to the fastest of the following two phenomena: (i) the "propagation" of the condition for the optical breakdown at the leading edge of the laser pulse, or (ii) the propagation of the blast wave produced by the local fast heating of the gas.

As it emerges from the basic data on laser-induced gas breakdown and on laser pulse propagation in refractive media [83, 89, 90], if the initial plasma is optically thick to the laser radiation (heavy gases and/or high pressure) the plasma will expand only toward the laser. In the opposite case of optically thin plasmas, expansion will take place in both directions, producing a quasi cylindrical region of ionized gas, nearly symmetric with respect to the focal position.

The obtained data, as for the most of acceleration experiments with gas targets, show the production of optically thin and then symmetric plasmas. The use of large f/N number (i.e. long focal lenght), particularly suitable for acceleration, enables the nanosecond pulse to produce a plasma whose length on the laser propagation axis is much larger then the transverse size. Furthermore, in the nanosecond time-scale, the transverse expansion of the hot plasma in the surrounding gas will result in a density depletion along the axis, as expected from a quasi cylindrical explosion. Plasmas obtained in this condition are found to be suitable for refractive laser-guiding over many Rayleigh ranges, opening to an efficient use in high gain, long-scale acceleration experiments.

The most interesting condition leading to relevant data for LWFA was found

focusing the pump laser beam 500 μm away from the nozzle slit plane on the z axis (see fig. 2.7). At this distance from the nozzle, the neutral helium density in the jet is of the order of $5{\cdot}10^{18}$ cm^{-3}: this values has been determined from the measurement of the electron density, since the characterization of the atomic density of the neutral gas-jet was made very difficult by the low index of refraction of neutral He gas.

Interferograms relevant to experimental conditions in which the laser focus position into the gas-jet has been progressively shifted from the entrance in the jet toward the exit are shown in fig. 2.8: the figure shows three interferograms obtained in different conditions of laser focus positions with respect to the gas-jet in the longitudinal direction, namely with the pump beam focused at $x = -1$ mm (fig. 2.8(a)), $x = 0$ mm (fig. 2.8(b)) and $x = +1$ mm (fig. 2.8(c)). The transverse and height positions were $y = 0$ mm and $z = 500$ μm in all the three cases.

Comparing the size of the plasma in the interferogram with the slit longitudinal size, it can be evinced that the length of the ionized gas reaches approximately 3 mm, while its shape is basically cylindrical. This cylindrical structure is evident for all the three conditions, regardless of the focus position in the gas-jet. The plasma length, however, is shorter than the whole available gas extension at 500 μm above the nozzle plane, that is estimated to be roughly 4 mm. Energy ranged from 460 mJ (interferograms 2.8(a) and 2.8(b)) to 490 mJ (interferogram 2.8(c)), so that the laser intensity on focus was of the order of $1.5{\cdot}10^{14}$ W/cm^2.

The procedure for analysis of the interferograms is the following: first, the phase map was computed using a fringe analysis technique based on Continuous Wavelet Transform Ridge Extraction [91], obtaining the phase-shift distribution in the x-z plane with a high degree of accuracy. In particular, this technique enables a better recognition of local variations of phase than other commonly used techniques based on Fast Fourier Transforms. Then, the obtained phase difference maps were in turn processed with an improved Abel inversion algorithm [92] in which the usual axial symmetry requirement is relaxed by means of a truncated Legendre polynomial expansion in the azimuthal angle. The analysis procedure used in this thesis, which permits to obtain an accurate electron density map of the plasma starting from the fringe pattern, is described in Appendix A. Figures 2.9 to 2.11 show the electron density maps retrieved for plasmas related to interferograms of fig. 2.8.

Deconvolved data demonstrate the production of quasi-cylindrical plasmas extending over several millimeters and with a hollow density channel on their axis. The mean on-axis electron plasma density ranges from 3.5 to $4.5{\cdot}10^{18}$ cm^{-3} for the three cases, as evident from the transverse lineouts in fig. 2.9(c), 2.10(c), and 2.11(c). As a speculation, it can be noted that these values of electron

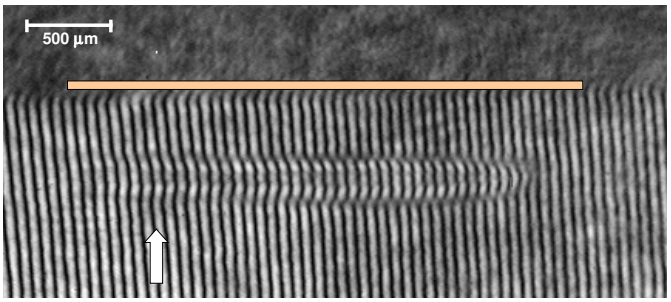

(a) Entrance

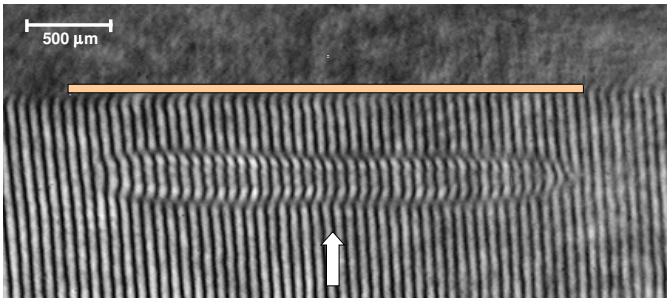

(b) Center

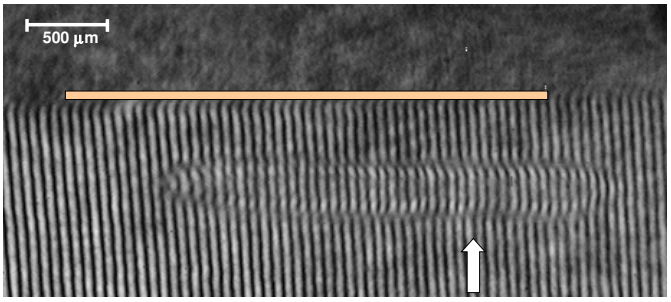

(c) Exit

FIGURE 2.8: Interferograms recorded focusing the pump laser at different positions on the x axis along the gas-jet. (a) $x = -1$ mm, laser energy 460 mJ; (b) $x = 0$ mm, laser energy 460 mJ; (c) $x = +1$ mm, laser energy 490 mJ. For all the interferograms $y = 0$ mm and $z = 500$ μm. The position of the 3 mm long slit and of the nominal focus of the main pulse in the gas-jet are indicated by the horizontal solid line and by the arrow, respectively. The laser pulse propagates from the left side of the images.

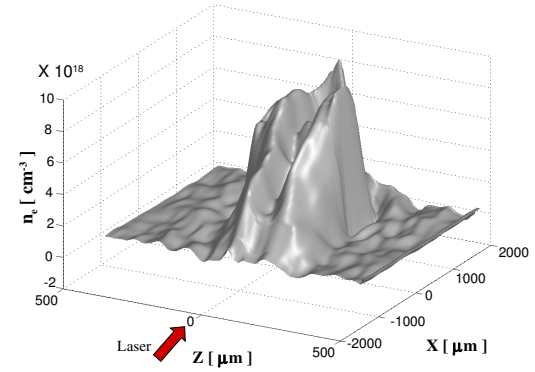

(a)

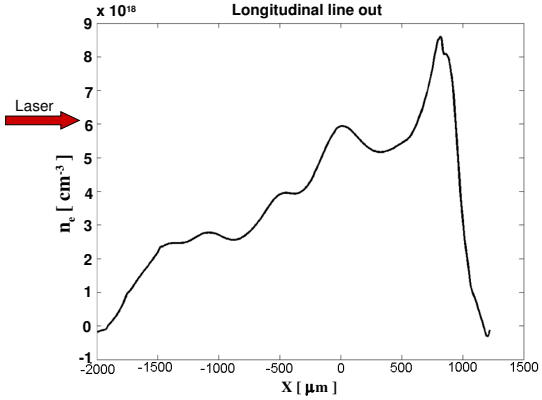

(b)

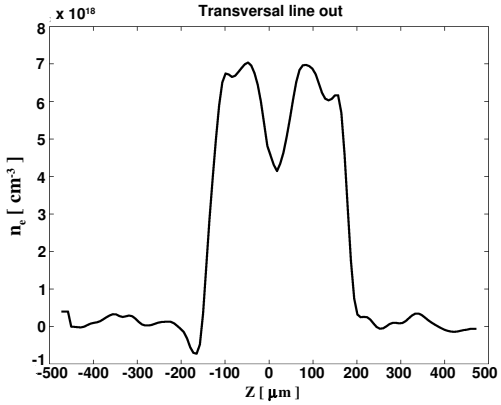

(c)

FIGURE 2.9: Electron density maps obtained after the analysis of interferogram 2.8(a). (a) 3D reconstruction of the plasma density profile. (b) Density lineout taken on the longitudinal axis. (c) Density lineout taken at $x \approx -300$ μm in the transverse direction (z axis). The origin of the z axis corresponds to 500 μm from the nozzle.

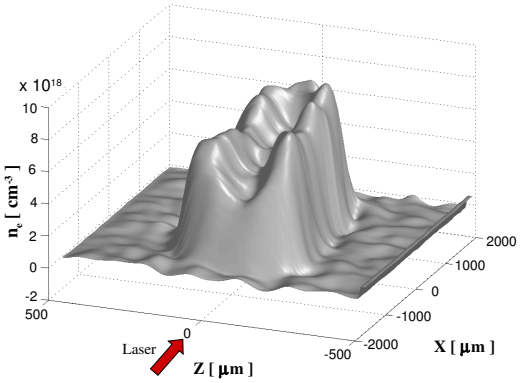

(a)

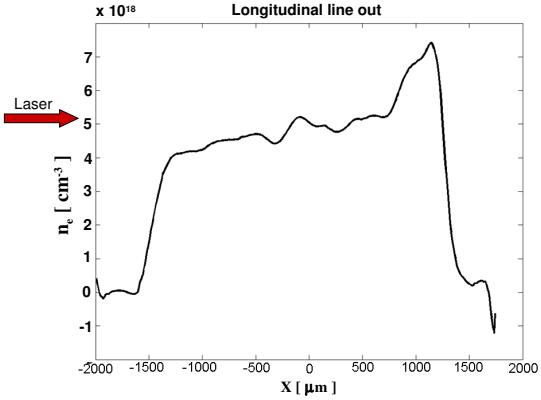

(b)

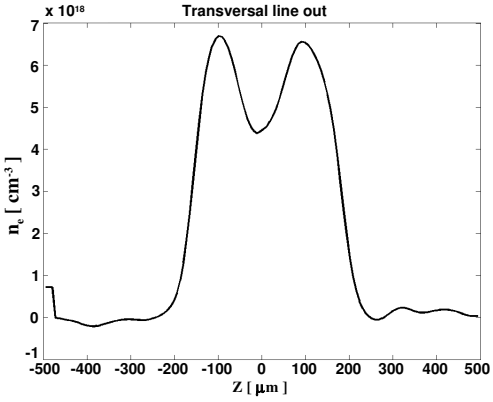

(c)

FIGURE 2.10: Electron density maps obtained after the analysis of interferogram 2.8(b). (a) 3D reconstruction of the plasma density profile. (b) Density lineout taken on the longitudinal axis. (c) Density lineout taken at $x \approx -300$ μm in the transverse direction (z axis). The origin of the z axis corresponds to 500 μm from the nozzle.

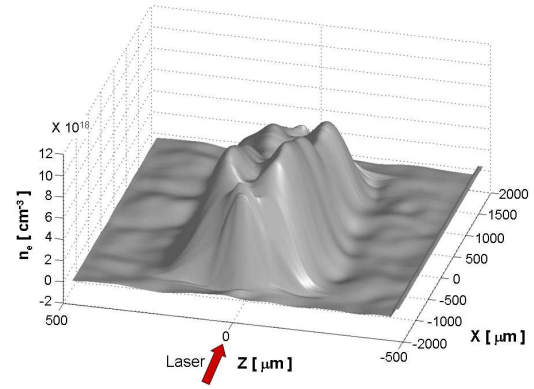

(a)

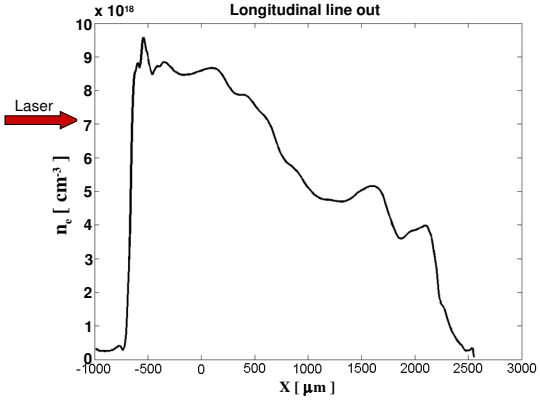

(b)

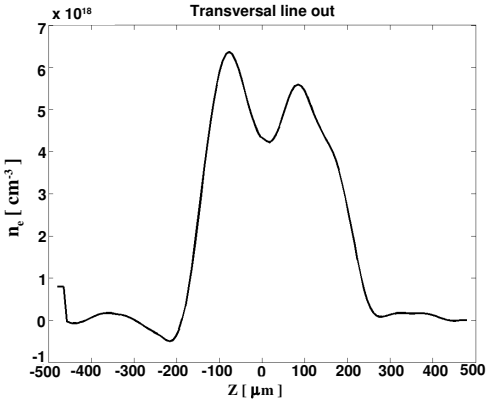

(c)

FIGURE 2.11: Electron density maps obtained after the analysis of interferogram 2.8(c). (a) 3D reconstruction of the plasma density profile. (b) Density lineout taken on the longitudinal axis. (c) Density lineout taken at $x \approx -100$ μm in the transverse direction (z axis). The origin of the z axis corresponds to 500 μm from the nozzle.

density are quasi-resonant in the LWFA regime with laser pulses of duration $\tau_L \approx 30$ fs FWHM, according to the relation (1.7).

The density along the longitudinal axis exhibits a different behavior in the three cases: it rises or falls depending on the focus position with respect the gas. From the entrance to the exit of the jet, the on-axis density has a slope that varies in sign and value, passing from a quite steep ascending tapering (map 2.9(b)) to a smooth increasing profile (map 2.10(b)) and finally to a quite steep descending one (map 2.11(b)). In every case, the maximum density along the plasma axis is roughly 10^{19} cm^{-3} and is located at one end of the channel, constituting a sort of "tip" with a few tens of μm's width. It is worth noting how the obtained plasmas present only a single-end tip, while on the opposite side on the channel longitudinal axis the plasma has a rather smooth descending-to-zero slope. This is due to the fact that, except for the case in which the laser is focused at the center of the gas-jet, one edge of the plasma falls in a region of lower gas density (either the entrance or the exit) where boundaries of the jet are located. This feature nicely fits with the requirements of Sprangle's work, and add gas-jets to the already proposed gas-filled capillaries as target to reach GeV energies for laser wakefield accelerated electrons. However, the use of larger f/N focusing optics can provide plasma channel extension from one gas-jet boundary to the other (in the laser propagating direction), in order remove the outer tips. This can be needed in case of acceleration experiments in which electrons are injected in the plasma from an external source (see section 1.2.4.2), in which a density wall can degrade the quality of the electron beam.

Figures 2.9 to 2.11 show that the maximum density and the depth of the ending tip are comparable to the ones of the walls of the channel in all cases. This is due to the fact that the edges of the plasma cylinder are fronts of the detonation wave that arises from the expansion of the hot plasma towards the surrounding neutral gas. In this way also the sharp drop of the electron density at the outer walls of the plasma can be explained, being the separation layer between the ionized and the unionized gas. The scale length of such a layer is of the order of 10 μm.

For what concerns the transverse density profile (along the z direction), the density minimum has a value in the range of 60% to 70% with respect to the channel walls, while its radius r_{ch} at half of the depth is of the order of 30 to 50 μm. As explained in the following, this values are suitable to optically guide a driving pulse (the theory of refractive waveguides is briefly addressed in section 1.2.2.1). Figure 2.12 shows the magnification of the region where the density minimum is in lineout 2.10(c). The density distribution in figure can be described as $n_e(r) = n_0 + \Delta n_e (r/r_{ch})^2$, given that the values for n_0 and $\Delta n_e / r_{ch}^2$ resulting from the fit are: $4.542 \cdot 10^{18}$ cm^{-3} and $3.74 \cdot 10^{22}$ cm^{-5}, respectively. With reference to equation 1.20, which relates the plasma channel density profile

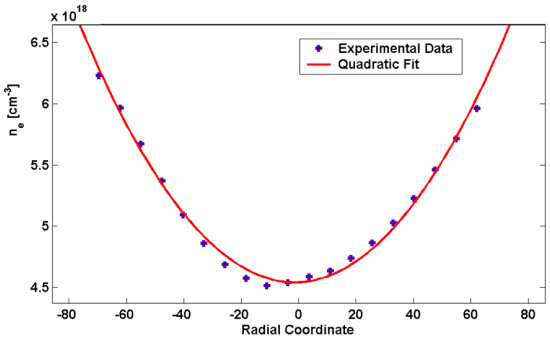

FIGURE 2.12: Magnification of the central region of fig. 2.10(c) fitted by a quadratic curve, whose parameters are given in the text.

with the laser spot size to match the optical guiding condition, the obtained data are consistent with $w_0 = 23$ μm. It means that pulses focused in spots smaller than w_0 can be refractive-guided in such plasma channels. Furthermore, the guiding basic properties of the obtained plasma channels can be evaluated in terms of the number of high-order Gaussian beam modes that can be supported. Three different models can be used to describe the guiding properties versus plasma channel dimension [93, 94]: in our case let's assume that the n-order mode spot size evolves as $\sqrt{2p + |m| + 1}$ times w_0, where $p \geq 0$ and m are radial and azimuthal indices and w_0 is the spot size calculated above (corresponding to the $1/e$ field radius of the $p = 0$, $m = 0$ mode). The constraint on the number of guided modes arise then from the inequality $w_0 \cdot \sqrt{2p + |m| + 1} \leq r_{ch}$, which in turn results in the condition $2p + |m| + 1 \leq 10$. This implies that the number of modes capable to propagate in the waveguide is as high as 55.

Furthermore, a scheme for electron self-injection and acceleration in LWFA regime has been proposed by Kim et al. [95], in which the pump laser beam propagation axis is perpendicular to the plasma channel axis, in order to exploit the transverse parabolic profile of the electron density as a transition to induce self-trapping. 2D simulations performed in that work demonstrated trapping of electrons and acceleration to energies of more than 30 MeV for electron densities of the order of $4{\cdot}10^{18}$ cm^{-3} to $1{\cdot}10^{19}$ cm^{-3} and laser drivers with peak power 10 to 30 TW. The parabolic profile of the above presented plasmas, as well as their density in the range of simulations of ref [95], makes the obtained plasmas suitable for tests in the experimental scheme proposed by the authors.

2.2.4.1 On the dynamics of the ionization process

In order to find reliable and reproducible conditions to be used in systematic experiments, it is necessary to understand the mechanisms that contribute to ionize and deplete the plasma channel. Production and evolution of laser-produced

plasmas in gaseous target by optical breakdown have been studied from more than 30 years ago [83]. The expansion of the plasma column follows the growth of the laser pulse power and the onset of a blast wave arising from the sudden release of laser energy in the gas. Figure 2.13 presents on the top a Gaussian laser pulse power versus time and on the bottom the plasma length versus time. With reference to the figure, at a given time t_{th} the power reaches the value

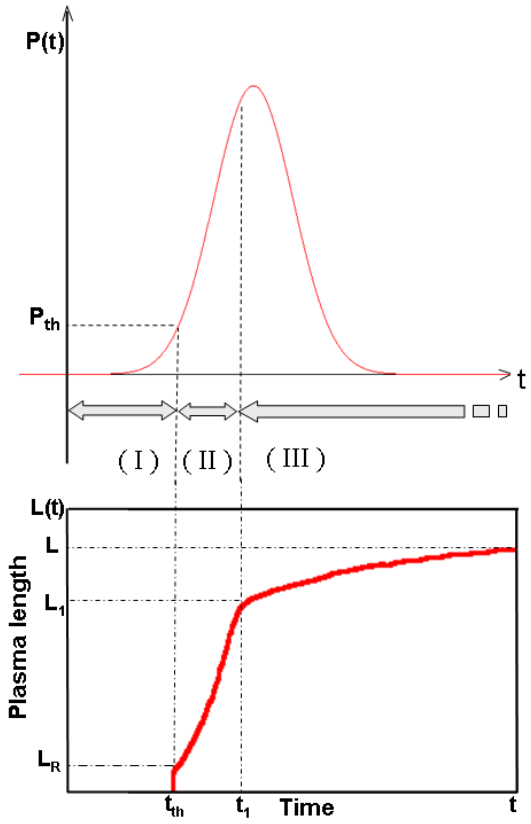

FIGURE 2.13: Trend of Gaussian laser pulse power (*top*) and plasma length (*bottom*) with time. In region (I) the laser power is below the threshold for optical breakdown of the gas. Region (II) represents the range in which the laser power is above threshold and thus the medium ionization occurs for optical breakdown. In region (III) the ionization process is eventually developed by propagation of the blast wave through the unionized gas.

P_{th}, that corresponds to the threshold value for intensity I_{th} for breakdown in the focus region. The first breakdown creates a plasma approximately as long as the Rayleigh range (L_R in the figure). At this point the layer in the gas target in which the threshold condition is satisfied shifts progressively along the propagation direction of the beam, driven by the rise of the laser pulse intensity in the geometry of the focusing optics (we are operating with a large f/N).

The ionization front moves thus according to the longitudinal expansion of this layer. In the meantime, a blast wave has originated from the strong energy release on axis in the focal region by the laser pulse, and it starts to radially develop [96]. In the transverse direction (z), it results in an electron density depletion from the axis towards the external walls. The propagation of the above-breakdown-threshold condition continues until the time t_1, at which its velocity is exceeded by the expanding speed of the shock wave. At this time, the plasma has a length denoted with L_1. The leading mechanism for ionization is now the propagation of the shock wave, that continues supported by the laser energy deposition. Obviously, the blast wave propagates with a velocity that decreases with time following the laser pump depletion.

Going in the details of the experiment, in our case the threshold intensity for optical breakdown is found to be $I_{th} \approx 5{\cdot}10^{11}$ W/cm^2, according to the well-known data of [83], while the peak value as reported above exceeds 10^{14} W/cm^2. It implies that, as stated before, the breakdown occurs very early during the laser pulse, and a region of $L_R \approx 100$ μm length will be ionized almost instantaneously. After that, the plasma length increases symmetrically (the plasma is optically thin) up to an extension of $2L_1$. Taking into account I_{th}, the Gaussian increase of the power, the focusing geometry and the velocity of the blast wave typical of our experiment, we estimate $2L_1 \approx 2.8$ mm, that is well consistent with interferograms like the ones shown in fig. 2.8. The residual expansion of about 150 μm on each side is due to the blast wave, whose mean velocity, considering an expansion time of 5 ns after the pulse peak, would then be $5 \cdot 10^6$ cm/s. We observe that, consistently with the assumption of a radial expansion driven by the cylindrical blast wave, the whole radius of the plasma cylinder is also found to be ≈ 150 μm..

2.2.4.2 Discussion on the relevance of the obtained results

This preliminary study on plasma channel production by nanosecond laser pulses, similar to the ASE pedestal that characterizes most of the fs high-intensity pulses employed in LWFA, shows a good reproducibility in terms of electron density profiles and makes them capable of being employed in acceleration experiments. In fact, a twofold kind of experiments can be proposed: a first one in which a single fs pulse exploits its ASE pedestal to pre-form the plasma as in the mimicked case presented above. A second possibility rely on the coupling of two temporally synchronized laser pulses with different duration (a ns one to pre-create the plasma channel and a fs one to drive the acceleration process). In this case the control on the ns pulse would be more careful, while the short pulse temporal profile should be cleaned to high-contrast by mean, for example, of plasma mirrors (briefly described in section 2.1.2). Attention should be finally payed in the latter case to the degree of ionization of the medium after

the long pulse propagation, since a non-complete ionization would imply that either part of the energy in the short pulse is loss in further ionization, and that the longitudinal electron density profile is modified during its propagation.

In this framework, longitudinal plasma density distributions like the one of fig. 2.9 can be suitable for acceleration of electrons in the LWFA scheme, as theoretically proposed by Sprangle et al. in 2000 [97]. In that paper it was shown that if the plasma density on axis increases with a given trend as a function of the distance traveled by the laser pulse, the phase velocity v_φ of the accelerating field in the wake of the laser can be made equal to the speed of light c. Depending on the slope of such a "tapered" plasma channel, this happens several plasma wavelengths behind the laser pulse. In this way, acceleration can benefit in a two-fold way: from one side, phase-matching of electrons with the accelerating plasma wave is maintained for the whole acceleration distance (avoiding dephasing); moreover, a highest energy gain can be achieved (the accelerating structures travels at c).

The location behind the laser pulse for which $v_\varphi = c$ is called "luminous point". The luminous point actually moves relative to the wake of the laser pulse, making it unsuitable for the above acceleration purposes.

However, it is shown that providing the following relation between the plasma frequency and the longitudinal coordinate, the luminous point remains fixed with respect to the wakefield at K plasma wavelengths behind the pulse:

$$\frac{\partial\,\hat{\omega}_{pe}}{\partial\,\hat{z}} = \frac{\hat{\omega}_{pe}^2}{2\pi K}\left[\left(\frac{\pi w_0}{\lambda_l}\right)^2 \hat{\omega}_{pe}^2 + 1\right] \tag{2.4}$$

in which $\hat{\omega}_{pe} = \omega_{pe}(\hat{z})/\omega_0$ and $\hat{z} = z/z_R$, given that ω_0, $\lambda_l = 2\pi c/\omega_0$ and w_0 are laser's frequency, wavelength and waist size, respectively.

Equation 2.4 can be solved with a set of laser parameters typical of a Ti:Sa system commonly employed as driver in acceleration experiments. For example, choosing the following set of parameters: $\lambda_l = 0.8$ μm, $w_0 = 6$ μm and $K = 2$ to fix the luminous point two plasma wavelengths behind a laser driver, the curve plotted in fig. 2.14 is obtained. In the figure, plasma electron density as function of longitudinal distance in units of the Rayleigh length is shown, making it easy to be compared with the longitudinal lineouts of figs. 2.9(b) to 2.11(b). Being the similarity of the experimentally obtained plasmas lineouts with the one in fig. 2.14 striking, the presented technique of plasma channel formation in gas-jet represents a valid alternative to the generation of tapered plasma channels in segmented gas-filled capillaries, in which the density is varied by changing the capillary radius or discharge current or voltage along the capillary as initially proposed by Sprangle et al. in ref. [98].

Furthermore, it must be noted that from previous data [99] it is known that the electron temperature of our plasma is $T_e \approx 50$ eV. At the density of the obtained plasma, this implies a complete ionization of the He gas in the plasma

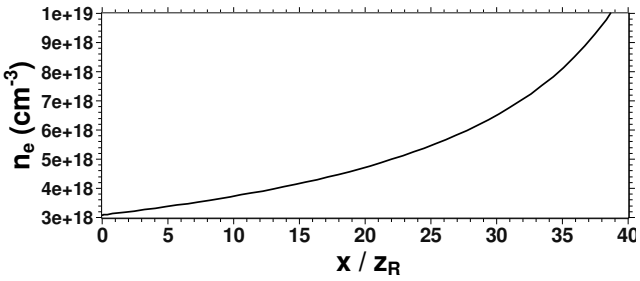

FIGURE 2.14: Plasma electron density longitudinal profile as obtained solving equation 2.4 with parameters $\lambda_l = 0.8$ μm, $w_0 = 6$ μm and $K = 2$.

volume [100], so that the produced plasmas can fit the above model as no further ionization could degrade the high-intensity pump laser.

2.3 Study of stable propagation of intense fs laser pulses in gas-jet

The results shown in previous section can be combined and related with the propagation of a fs laser pulse preceded by its real ASE pedestal through the results of an experiment carried out at the SLIC laser facility of CEA Centre of Saclay (France) in collaboration with the PHI group, presented in this section.

As target, the same gas-jet described in section 2.2.3 has been used while the laser system available at SLIC facility has been already described in section 2.1.2.1. In order to perform studies of ultra-short laser pulse propagation in gas with particular attention to the effects of the nanosecond ASE pedestal, no plasma mirror was employed to temporally clean the pulse and improve the contrast ratio. As it is evident from figure 2.2, if no plasma mirror technique is applied, the laser pulse has an ASE pedestal of nanosecond duration for which the contrast ratio is as high as 10^6. Beyond the ASE pedestal, a picosecond prepulse is also present, with a contrast ratio between 10^3 and 10^4. The laser beam was focused on the gas-jet at a height from the plane of the nozzle of 500 μm by an $f/5$ off-axis parabolic mirror in a spot of 13 μm FWHM, $M^2 = 3.3$. The nominal intensity reached in the focus was about $3{\cdot}10^{18}$ W/cm^2, corresponding to a normalized strength parameter $a_0 \approx 1.2$: the relativistic regime was thus slightly exceeded. After focusing, it was found that the focus of the ASE preceded the focus of the fs pulse by approximately 400 μm in the target. The spot region was monitored by a CCD camera collecting the transmitted light with a $f/5$ lens, while a spectrometer with 5 nm resolution gave the spectrum

of the transmitted pulse. The layout of the experimental chamber is sketched in fig. 2.15 For what concerns the interferometry, a Mach-Zehnder setup was

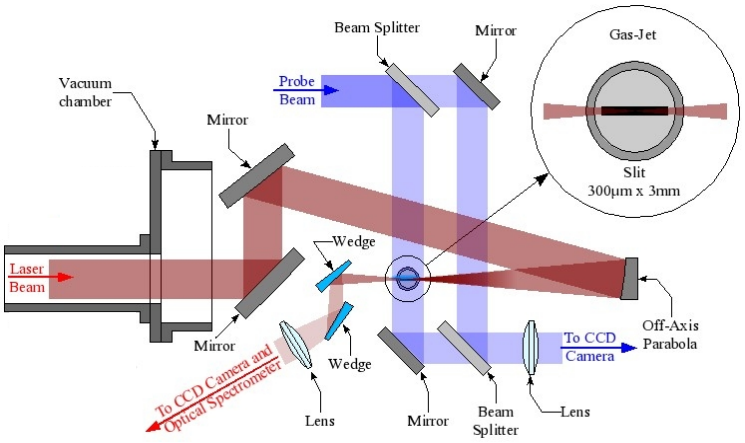

FIGURE 2.15: Layout of the experimental setup employed in the propagation experiment carried out at CEA Centre of Saclay at the SLIC laser facility with the UHI10 laser system with no plasma mirror employed to temporally clean the beam.

employed. This setup makes use of two beam splitters and two mirrors. This configuration is more flexible in terms of magnification and field of view than the previously employed Nomarski, but requires the beam to be separated in two pathways far from the region of interest: one split beam passes through the plasma while the other propagates undisturbed in vacuum, then the beams recombine. Altough this configuration needs more accurate alignment, it has the advantage that the two arms can be widely separated spatially. Mach-Zender interferometer can also be used to obtain shadowgraphic images of the plasma, provided that the unperturbed beam is blocked [101]. As probe beam, a fraction of the femtosecond pulse was doubled in frequency by means of a KDP-type-I crystal, which contributed to stretch the duration of the probe beam up to estimated value of about 120 fs. This value represents the temporal resolution of the obtained interferograms.

The work presented in this thesis concerns the analysis and the discussion of the data obtained with the above described setup. In order to draw some considerations about the process, two regimes of propagation are discussed in the following, discriminating whether the ASE pedestal was above threshold for ionization or below threshold. Figures 2.16 and 2.19 show two interferograms, with the corresponding density maps, obtained with helium gas-jet at a pressure of 8 bar. Both interferograms were recorded 2 ps before the arrival of the tip of the

short laser pulse in the nominal focus of the ASE pedestal. In all the following figures representing raw and deconvolved data, the axis are labelled following the coordinate system of fig. 2.7, while the laser and the gas-jet comes from the opposite side with respect to previous section (right to left and bottom to top, respectively).

As it will be evident from data presented in sections 2.3.1 and 2.3.2, there are two regimes of gas density that separately put the ASE ns pedestal in condition of either free propagation below ionization threshold or above threshold to create a pre-plasma in the medium. These regimes are entered by slightly shifting the laser path along the z direction. The corresponding maximum electron density goes from $2{\cdot}10^{19}$ cm^{-3} to $3.6{\cdot}10^{19}$ cm^{-3}. Because of the very low refraction index of the helium (1.000036), as well as the small transverse thickness of the gas column (the transverse size of the gas-jet, as described in section 2.2.3 is 300 μm) and the absence of steep neutral density gradients due to the subsonic nature of the gas flow, it has not been possible to determine via interferometric measurements the neutral gas density distribution. The determination of the neutral gas density profile is thus inferred from the maximum electron density determined after data deconvolution, under the assumption a full gas ionization by the powerful CPA fs pulse. It turns then out that in the case of free propagation, the gas density is about 1 to $1.2{\cdot}10^{19}$ cm^{-3}, while in the second case is approximately $1.8{\cdot}10^{19}$ cm^{-3} [102], accounting then for a difference of the order of 30% in one case with respect to the other. However, this minor difference is enough to produce a transition from "below" to "above" the optical breakdown of the gas at the given ASE intensity.

2.3.1 Laser pulse propagation *below* threshold for ASE induced breakdown

Figure 2.16 shows an interferogram and its respective deconvolved electron density map obtained 2 ps before the arrival of the front of the pulse in the nominal focus position ($x \approx 300$ μm in the figure). With reference to fig. 2.7, the focus nominal position was ($x \approx 300$ μm, $y = 0$, $z \approx 500$ μm). The laser propagates from right to left in each following figure, while the electron density map were retrieved with the technique described in appendix A.

From the density maps 2.16(b) it is possible to sketch some considerations on the gas neutral density distribution along the direction of the gas flow from the nozzle plane. It is in fact evident that the electron density distribution is partially asymmetric in the z direction, reaching the density n_e values higher in the lower half (positive values of z) than in the upper part (negative z). The reason for this feature can be addressed to the neutral gas density gradient along the z direction, the rarefaction growing with distance from the nozzle. The transverse electron density profile in the z direction is plotted in figure 2.20. An

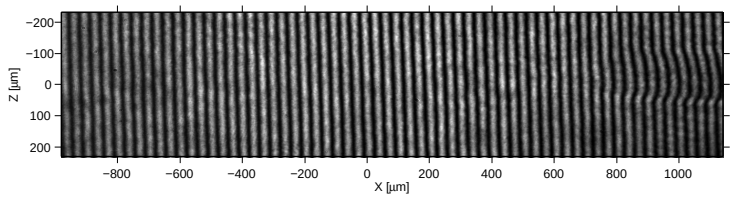

(a)

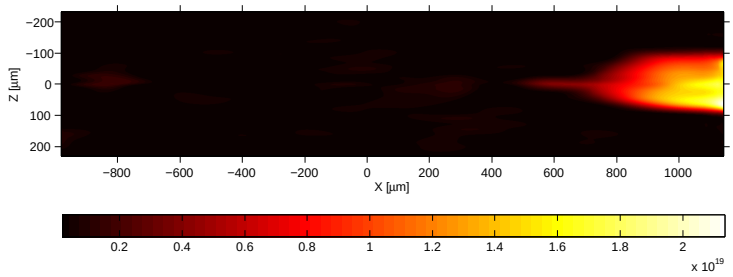

(b)

FIGURE 2.16: Raw and analyzed data of pulse propagation below threshold for ionization by the ASE ns pedestal. The laser comes from the right hand side of the image. (a) Interferogram taken 2 ps before the arrival of the front of the fs pulse in the nominal focus position ($x \approx 300$ μm in the figure). (b) Electron density map retrieved from the fringe pattern.

asymmetric shape with respect to the plasma axis located at $z = 0$ is clearly evident. The maximum of n_e is located roughly at $z = 70$ μm, i.e. at a height

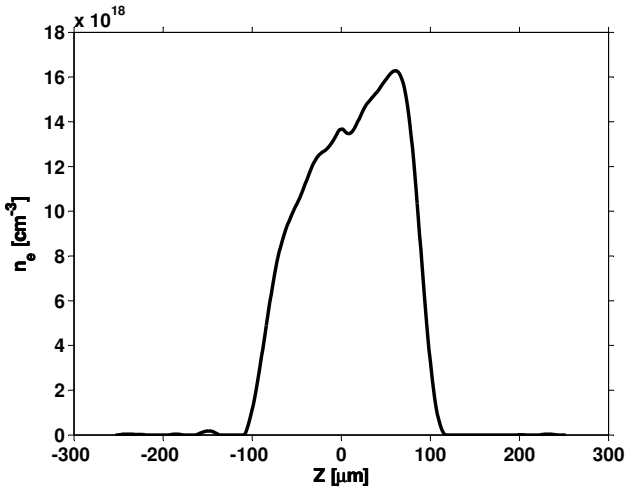

FIGURE 2.17: Transverse lineout along the z direction of the electron density of fig. 2.16(b) taken at $x \approx 1$ mm.

of 430 μm from the slit plane. The density grows approximately by a factor of 50% from the upper region (farther from the nozzle plane, $z < 0$ in figure) to the lower region (closer to the nozzle plane, $z > 0$ in figure).

Furthermore, fig. 2.16(b) shows the ionization induced by the laser pulse when the ASE pedestal is below threshold for inducing breakdown in the gas, and presents a feature that is proper of the short laser pulse delivered by the SLIC system: starting at $x \approx 500$ μm a filament of plasma with longitudinal extension of 300 to 500 μm and diameter of ≈ 20 μm is found to precede the large ionization front located at $x = 800$ μm. This tip, present in every obtained interferogram (as can be evinced even from the following data presented herebelow), is due to the effect of gas ionization induced by the most intense part of the picosecond pedestal, that is temporally located about 1 ps before the CPA pulse (this picosecond precursor is visible in the autocorrelation trace of the laser pulse in fig. 2.2). The thin plasma has a length corresponding to about 1-ps duration and it is due to the action of the picosecond precursor of the main pulse, whose intensity in that region close to the waist is as high as required to ionize the gas [83]. From the sequence of the interferograms at different times (figures 2.18 and 2.21) it turns out that this particular pre-plasma appears when the main pulse approaches the focus, and it moves with the main plasma front at its left (i.e., in front of it). The net change in the plasma diameter at the arrival of the main pulse, located in the map approximately at $x \approx 850$ μm, evidences an ultra-fast ionization of the gas in a diameter much larger than the waist of the focusing optics, as can be expected by the transverse intensity profile of the pulse, and the values of the intensity needed for direct ionization of the gas (by single atom multi-photon and/or tunneling processes).

Figure 2.18 shows several snapshots of laser propagation evolution as inferred from the induced effects on gas ionization. In fact, by accurately changing the delay between the plasma creation by the short, intense fs pump pulse and the arrival of the probe beam on the interaction region, it has been possible to follow the evolution of the ionization process from early times up to several picoseconds after the focusing. The time $t = 0$ indicates the moment in which the ahead tip of the plasma slice produced by the picosecond pedestal reached the nominal focus position, located in the figures at $x \approx 300$ μm. Interferogram were recorded in a time range that spanned from -2 ps to +2 ps.
As the laser approaches to the focus position, the fs ionization front reduces the transverse extension of the ionized region, the beam divergence reducing as it gets close to the focus. Once the pulse goes beyond the focus, it emerges keeping the original divergence due to the focusing optics.

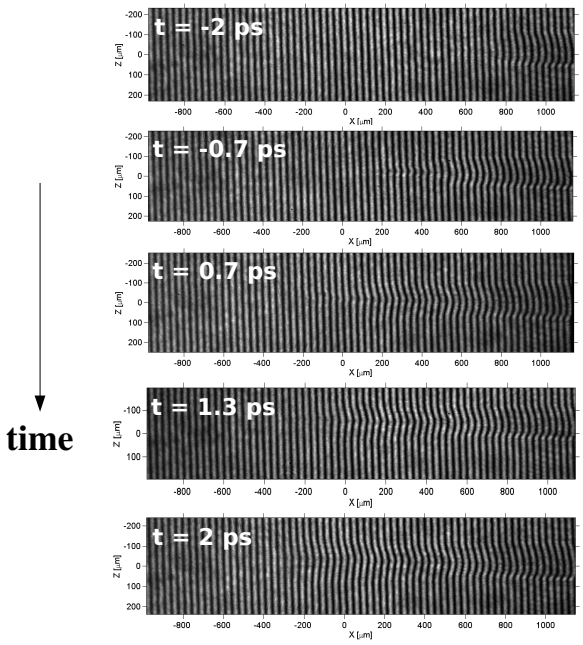

(a)

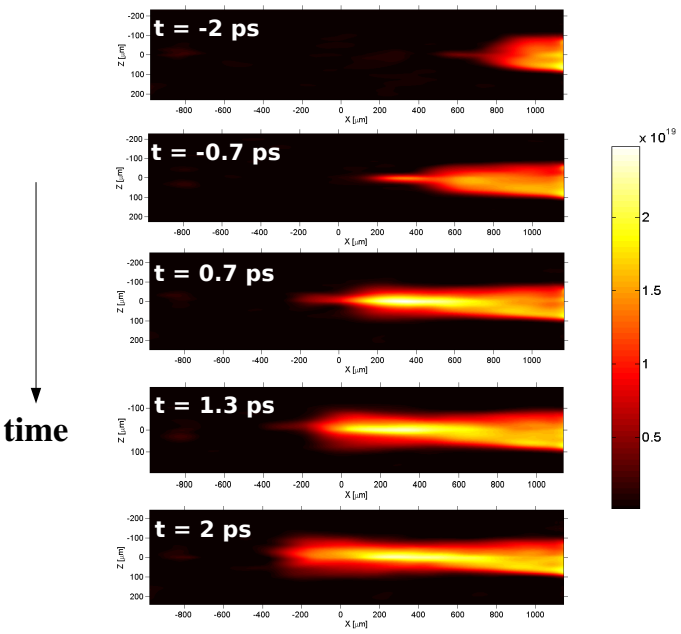

(b)

FIGURE 2.18: Interferograms (a) and respective density maps (b) showing the evolution of the pump laser pulse propagation in the helium gas-jet below threshold for ASE initiating ionization. Data were recorded from $t = -2$ ps to $t = +2$ ps, assuming as zero time $t = 0$ the moment in which the ahead tip of the plasma slice produced by the picosecond pedestal reaches the nominal focus position $x \approx 300$ μm.

2.3.2 Laser pulse propagation *above* threshold for ASE induced breakdown

A shift in the z direction of the interaction point between the laser and the gas-jet towards the nozzle plane enabled the investigation of a different regime, in which the nanosecond ASE pedestal of the pump pulse is above threshold for gas ionization. The focusing geometry of the beam was set such that the ASE pre-pulse was focused in the middle of the gas-jet ($x = 0$ according to fig. 2.7). This scenario is represented in fig. 2.19, that shows both the interferogram and the respective electron density map obtained 2 ps before the arrival of the forecoming tip of the picosecond pedestal in the $x = 0$ position. It is evident

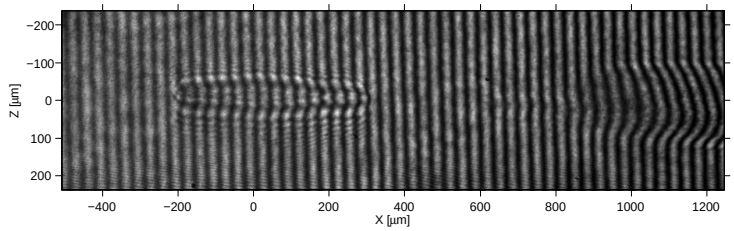

(a)

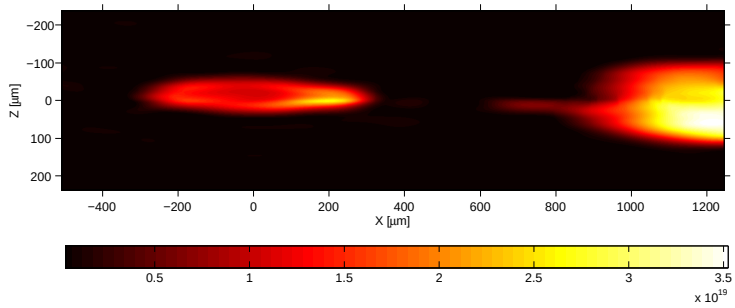

(b)

FIGURE 2.19: Raw and analyzed data of pulse propagation above threshold for ionization by the ASE ns pedestal. The laser comes from the right hand side of the image. (a) Interferogram taken 2 ps before the arrival of the front of the pulse in the nominal focus position ($x = 0$ in the figure). (b) Electron density map retrieved from the fringe pattern.

that the plasma created by the ASE pre-pulse is present ahead of the short pulse, and it is expanding as time goes by and the short pulse approaches the $x = 0$ position of system nominal focus. The plasma created by the short part of the pulse obviously resembles the analogous ionization profile obtained in the case of propagation free from ASE-induced pre-plasma. Again the density distribution is asymmetric in the z direction with a maximum located in the bottom half-map.

Recalling the results of section 2.2.4, it can be noticed that the ASE-induced plasma bubble is depleting along the laser propagation axis, and a hollow density channel is forming on axis. This effect is the same observed with a dedicated laser in Pisa experiment. The propagation of the above-threshold ASE intensity followed by the shock wave originated by the sudden heating of the plasma on the x axis contributed to the hydrodynamic expansion of the hot pre-plasma and to its longitudinal depletion. At the delay of the recorded interferogram, the plasma channel has a longitudinal extension of approximately 500 μm and a transverse size of ≈ 100 μm. Fig. 2.20 shows the transverse lineout (taken along the z direction) of the electron density in fig. 2.19(b) of the plasma produced by the ASE. The channel-like transverse density profile is quite clear and is

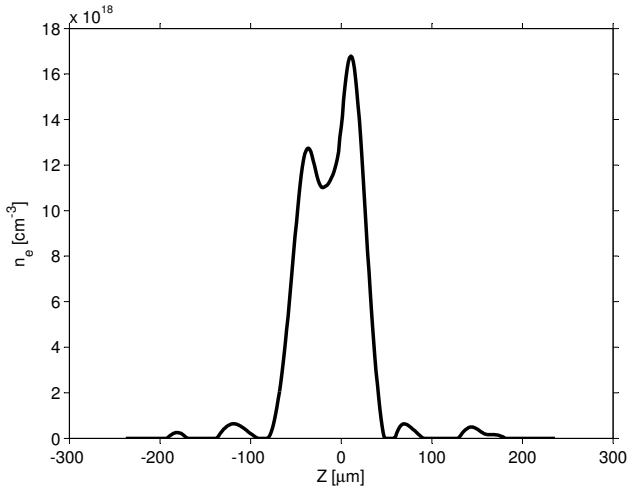

FIGURE 2.20: Transverse lineout along the z direction of the electron density of fig. 2.19(b) taken at $x \approx 0$.

parabolically shaped, with the minimum of density of the order of $1.1{\cdot}10^{19}$ cm^{-3} and two asymmetric walls higher of 20% (the farther from the nozzle plane, at $z < 0$) and of 50% (the closer to the nozzle plane, at $z > 0$). Again, the neutral gas density gradient due to the flow direction is reflected in a asymmetry of the ionized region.

Recording interferograms at different delays from the arrival of the short pulse, preceded by its pedestals, on target enabled the study of the propagation of the laser pulse in presence of the ASE-created pre-plasma. This sequence is shown in fig. 2.21, in which data obtained at pump-probe delays from 0.9 ps before to 3.7 ps after the arrival of the picosecond precursor in the nominal focus position $x = 0$ (that has been set as $t = 0$ in this case). The raw and deconvolved data show a peculiar effect induced by the pre-plasma on the propagation of the fs pulse: this latter is splitted in two spatial components by the interaction

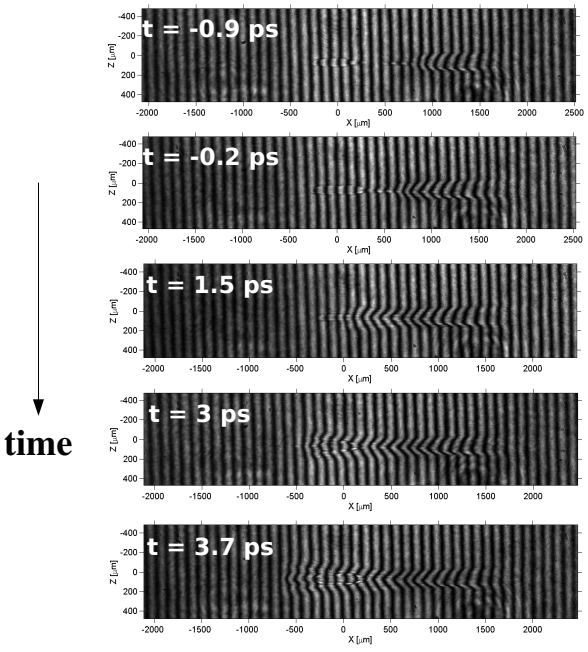

(a)

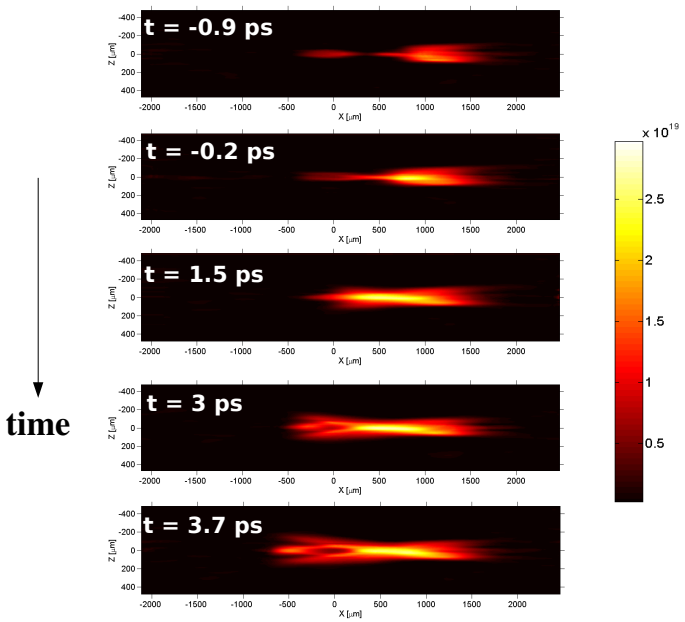

(b)

FIGURE 2.21: Interferograms (a) and respective density maps (b) showing the evolution of the pump laser pulse propagation in the helium gas-jet below threshold for ASE initiating ionization. Data were recorded from $t = -0.9$ ps to $t = +3.7$ ps, assuming as zero time $t = 0$ the moment in which the ahead tip of the plasma slice produced by the picosecond pedestal reaches the nominal focus position $x = 0$.

with the ahead plasma. The central part of the short pulse is collimated by the density channel on the axis, while the other is refracted away at an angle larger than the one given by focusing optics. The spatial component that is refracted away is ring-shaped, and the projection on the bi-dimensional plane of the interferogram makes it appear as external double wings. Furthermore, the ASE plasma boundary of higher density (basically a shock wave expanding in the gas) is further ionized by the CPA pulse to higher electron density than the surrounding plasma. The effect of the pre-plasma on the central part of the pulse can be observed indirectly here from the central feature of the electron density beyond the preformed plasma (towards negative values of the x coordinate). The fs pulse that crosses the expanded plasma channel actually clean itself after it encounters the pre-plasma. At the moment of interaction with the just-expanded waveguide, the central part of the short pulse travels along the longitudinal direction guided by the low-density channel created by the ASE pre-pulse. The outer regions of the short pulse, on the opposite, interact with the high-density walls of the channel and thus, due to the lower index of refraction that they encounter, are refracted away diverging from the original focusing optics.

The final effect of the pre-plasma can be evaluated looking at the far-field images of the transmitted pump laser pulse in presence or absence of the guiding channel. Figure 2.22 shows in fact the laser intensity distribution as imaged on a CCD collecting the transmitted light by an optics of the same aperture as the focusing optics ($f/5$). From the images of the laser spot it is evident that

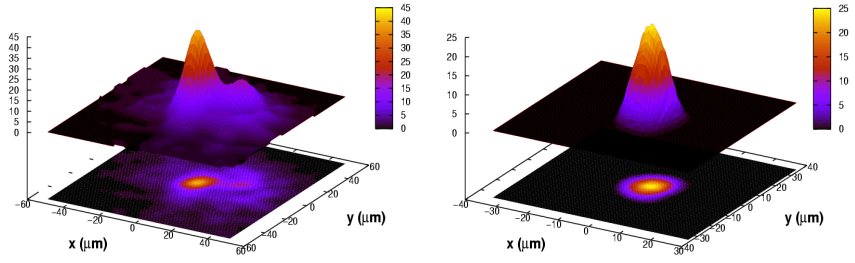

(a) (b)

FIGURE 2.22: 3D intensity distribution of the transmitted short laser pulse as recorded in the far field by a CCD. (a) Intensity profile below threshold for ASE-induced gas breakdown. (b) Intensity profile above threshold for ASE-induced gas breakdown.

a series of aberrations present in case of free propagation are canceled out in the spot imaged after propagation through the ASE-induced pre-plasma. The interaction of the short pulse with the hollow plasma channel results then in a spatial filtering of the pulse itself. This feature can be indirectly observed from

the electron density maps of fig. 2.21(b) at larger time delays. The spot images also give the evidence for the fact that the refraction to large angles of the CPA pulse is more efficient on the outer, more aberrated regions of the pulse. These regions are also the ones that are more affected by non-linear effects due to the laser ionization of the gas, such as defocusing or self-phase modulation. In fact, while the central part of the pulse ionizes the ahead incompletely ionized gas in one or few optical cycles, making the rest of the pulse (of more than 20 optical cycles) propagate in a fully ionized He channel, the external corona has a much lower intensity and then is more subject to defocusing by the higher electron density it encounters.

2.3.3 Comparison with numerical simulations

In order to discuss the physical feature observed in the experiment, a set of numerical simulations has been performed by Thierry Auguste of CEA/Saclay, whose results are briefly examined in the following. The code used to simulate the propagation process is based on the solution of the standard paraxial wave equation in cylindrical geometry. In a frame co-moving with the laser pulse, the equation of propagation is:

$$\frac{\partial}{\partial z}E(r,z,t) - \frac{i}{2k_0}\frac{1}{r}\frac{\partial}{\partial r}\left(r\frac{\partial}{\partial r}\right)E(r,z,t) + \frac{i}{2c^2k_0}\cdot\Delta\cdot E(r,z,t) = 0 \qquad (2.5)$$

where $E(r,z,t)$ is the slowly varying complex amplitude of the laser field, k_0 is the vacuum wave number, c is the speed of light and Δ accounts for the non-linear response of the plasma:

$$\Delta = \max\left[0, \omega_{p0}^2\left(\frac{1}{\langle\gamma\rangle} - 1\right) + c^2\nabla_\perp\left(\frac{\nabla_\perp\langle\gamma\rangle}{\langle\gamma\rangle}\right) + c^2\frac{\nabla_\perp\langle\gamma\rangle\nabla_\perp n_{e0}(r,z)}{n_{e0}(0,z)}\right] \qquad (2.6)$$

In equation (2.6) ω_{p0} is the undisturbed plasma frequency, $n_{e0}(r,z)$ is the space varying electron density and $\langle\gamma\rangle$ is the relativistic factor averaged on an optical cycle [103]. Equation (2.5) was solved iteratively in a self-consistent way with the ionization rate equations. Results were found to be not affected by the ionization rates used in the calculations, thus Perelomov, Popov and Terent'ev (PPT) ionization model was used [104, 105, 106], being valid in regime of multiphoton ionization.

The simulated scenarios did not account for the ASE-induced pre-plasma, but only for the free propagation regime. Simulations have been performed of the interaction of 10 TW, 65 fs FWHM laser pulses focused with an $f/5$ optics, M^2= 3.3 at a peak intensity of $I_{max} = 3.26{\cdot}10^{18}$ W/cm^2 on a He gas-jet with neutral density $1.8{\cdot}10^{19}$ cm^{-3}. Three different kind of simulations were performed, concerning the interaction of (*i*) the picosecond precursor alone, (*ii*) the femtosecond CPA pulse alone, (*iii*) both the ps and fs pulses as in the real case. This method permitted to evidence that the ps pulse alone creates

a plasma of radius ≈20 μm and length ≈500 μm, and is not self-focused in its propagation (*i*). in fact in this case, because of the power contrast ratio of the ps precursor that makes it reach only low values of a_0 ($a_0^{ps} \ll 1$), a self-focusing could only be due to Kerr effect in the neutral gas. However, this effect can be neglected in the considered case because of several reasons: the length of the gas-jet is too small and the gas density is too low, beyond the fact that the Kerr effect actually stops once the medium is ionized. Furthermore the helium non-linear refractive index is too small ($n_2^{He} \approx 10^{-28}$ cm^2/W), and this implies that the non-linear dephasing due to Kerr effect can be quantified as $\phi_{NL} \approx 6 \cdot 10^{-10} \ll \pi$.

In case (*ii*) only the external wings and the rising edge of the fs pulse are affected by ionization induced refraction, but again no significant increase of the intensity due to relativistic self-focusing was observed. Finally (*iii*), simulations performed with a 10 TW pulse and a picosecond pedestal show that a plasma can be created by the pedestal in the vicinity of the focus position in vacuum (in the middle of the jet, in $z = 0$). The size and the distance from the focus of this pre-plasma depend on the intensity contrast ratio. For a contrast ratio of 10^{-3}, the gas starts to ionize 2.7 ps before the femtosecond pulse reaches the middle of the jet, creating a plasma with radius ≈20 μm and length ≈300 μm. The results of the numerical simulations in case (*iii*) are shown in fig. 2.23 for the ps and fs pulses at three different times of propagation, from -0.5 ps before the arrival of the ps pulse in $z = 0$ to 3.7 ps after the precursor passage over that position. From fig. 2.23 and from the set of data obtained with the numerical computation it doesn't appear the asymmetry in the radial electron density distribution. This asymmetry, already pointed out in the previous section, is thus found to be real and actually due to the neutral gas density gradient arising from the flow along the z direction. The simulation accounted on the opposite for a gas-jet with a trapezoidal profile along the x direction with a 1.5 mm plateau and 250 μm ramps, and a Gaussian profile in the y direction with 500 μm FWHM.

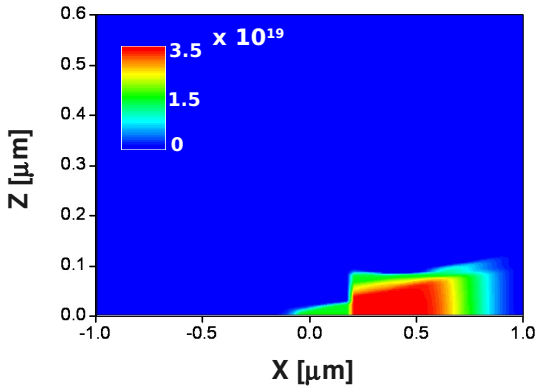

(a)

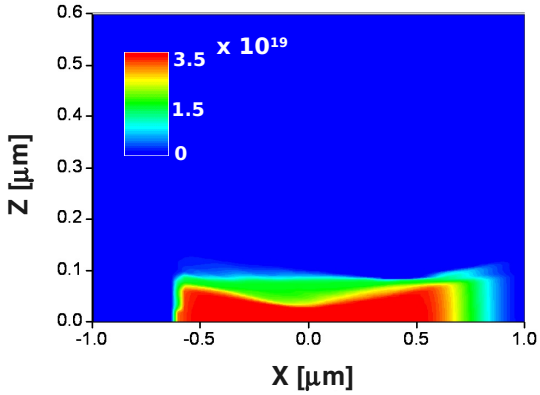

(b)

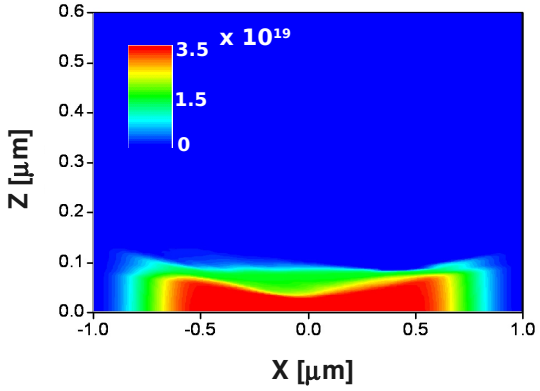

(c)

FIGURE 2.23: Snapshots of laser propagation in He gas-jet. Both the ps precursor and the fs CPA pulses are simultaneously present. (a) Snapshot at $t = -0.5$ ps before the arrival of the ps pulse in $z = 0$. (b) Snapshot at $t = 2$ ps. (c) Snapshot at $t = 3.7$ ps. The laser comes from the right hand side.

2.3.3.1 Effect of probe transit time on electron density measurements

One peculiar outcome of the numerical simulations of the short pulse propagation process is the difference between experimental and simulated data in the spatial scale of the electron density gradients induced by the massive ionization front that comes with the femtosecond CPA pulse. In fact, as shown in fig. 2.23, the ionization front of the CPA pulse resulting from the model is very sharp, with an abrupt jump in the plasma electron density in the presence of the fs pulse. This follows from the sudden ionization during the very first few optical cycles of the high-intensity pulse that exceeds 10^{18} W/cm^2. On the contrary, the maps of fig. 2.21(b) shows a much smoother ionization front, with density gradients of few hundreds of μm's. The experimental data seem thus in contrast with the expectations from ultrafast ionization process. A comparison of the longitudinal lineout of the electron density resulting from the experimental analysis and from the simulated data is shown in fig. 2.24.

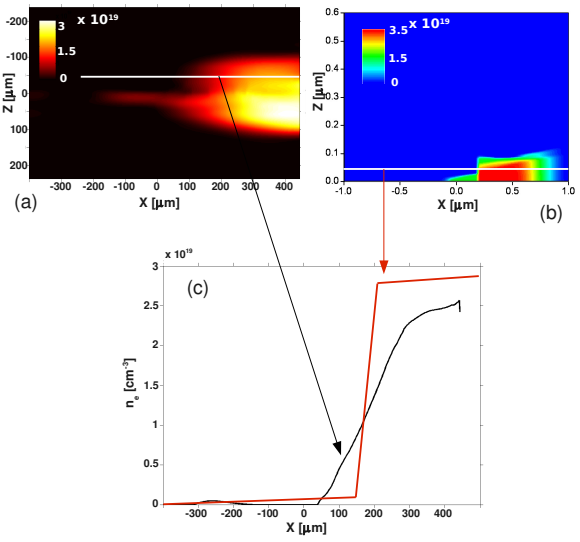

FIGURE 2.24: Comparison between the electron density retrieved by the analysis of the experimental data (a) and from the numerical simulation (b). Insert (c) shows the longitudinal lineout, taken at the z coordinate indicated by the white line, of the two different electron densities.

One explanation for this different behavior can be found as follows: when the probe pulse duration is comparable to (or shorter than) its transit time through the sample region, and the probed region changes its index of refraction in the same time-scale (or faster), then some artifacts can be generated in reconstructing the real phase and density maps [107].

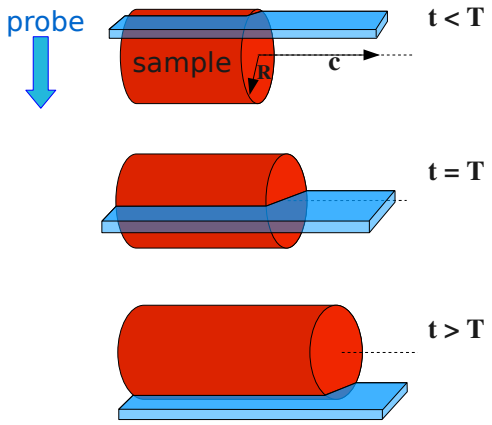

FIGURE 2.25: Scheme of cross-propagation of a fast-moving sample and an ultrafast optical probe. Time flows from top to bottom of the image.

As depicted in fig. 2.25, consider the case of a sharp ionization front that moves at a speed close to c. The created plasma cylinder has a diameter that is much larger that the optical depth of the probing pulse: in this case the transit time of the probe through the sample is longer than the probe duration ($\leq$ 120 fs in the presented experiment), thus the probe beam crosses a medium with a fast-changing index of refraction. This simultaneous propagation of both probe and ionization front reduces the fringe shift, increasingly toward the front with an apparent smoothing of the front density profile. In particular, the real profile is masked for what concerns the refractive index gradients in the direction of motion of the sample. Figure 2.26 shows the interferogram relative to the map of fig. 2.24(a), in which the region corresponding to the masked fringe shift is highlighted.

The effect of the transit time of the probe beam through the fast moving sample is to smooth the gradient of the index of refraction (and hence the electron density) over a length that is approximately equal to the diameter of the plasma cylinder. Two algorithms have been proposed to obtain the real profile of the index of refraction from data recorded with ultrafast interferometry, depending on the use of either the phase shift map or the fringes' visibility; the real time duration of the probe pulse could also be evaluated exploiting this technique [107].

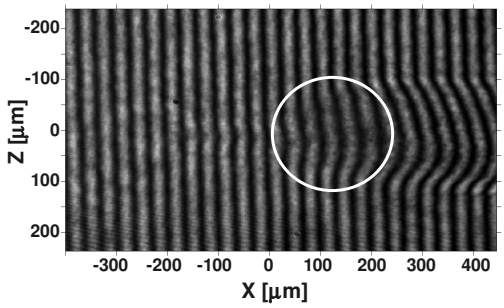

FIGURE 2.26: Interferogram relative to the map of fig. 2.24(a). The region corresponding to the masked fringe shift is highlighted by the thick white circle.

Chapter 3

Efficient electron acceleration with 10 TW laser pulses

Introduction

The experiment presented herebelow is the core of the Ph.D. work this thesis in focused on. It is based on an experimental campaign carried out at CEA Centre of Saclay (France), with the UHI10 laser system described in section 2.1.2.1, in collaboration with the host Physique à Haute Intensité (PHI) group, plus a group from LULI (France) and a group from the Institute for Transuranium Elements of Karlsruhe (Germany). The author was fully involved in the campaign, participating either to the set-up of the experiment at the Saclay SLIC facility and to the post-processing and analysis of the obtained data. In particular, the main experimental topics on which the work of the author was focused on were the set-up of the interferometric line and of the SHEEBA device, with the subsequent analysis of the obtained data on the key features of the produced plasma and of the accelerated electron bunches. Data obtained with the beam profile monitor and with the magnetic spectrometer have been analyzed as well by the author in collaboration with the group from LULI.

As it was pointed out in section 1.2, great attention is devoted to the improvement of stability and reproducibility over a large number of shots of the electron acceleration process. Laser propagation in the accelerating medium is affected by several types of instabilities, including filamentation and hosing, which are detrimental for the production of high-quality electron bunches. The requests look forward for high-charge, high-energy electron bunches emitted within a small solid angle, possible at a high repetition rate. The presented

experiment was then intended to find the best conditions for stable production of electron bunches with reproducible parameters. To this purpose, the 10 TW laser pulses provided by the UHI10 laser system represents a valid tool since, although its peak power is limited if compared to current worldwide employed lasers for acceleration, it can prevent the set-on of laser-plasma instabilities once moderately-relativistic intensities are reached on target. The lower limit that however has to be ensured is that the laser intensity on target is as high as the one required by the regime of local wave breaking for the excited plasma waves. This latter condition, that is essential for a correct capture of electrons and their acceleration in a quasi-mono-energetic bunch, can be achieved by focusing a powerful enough pulse at the sharp boundary of a supersonic gas-jet. To explore a wider parameters space, supersonic nozzles of different size were used, for each case monitoring the plasma density distribution and the characteristics of the accelerated electron bunches [108].

In this chapter the results obtained from the experiments are revised, with particular attention to the most significant outcomes from the several diagnostics that have been employed and with emphasis on the role of the author in data-taking and data-analysis.

3.1 Experimental set-up and target characterization

The laser-driven electron accelerator was set up at the SLIC facility (CEA-Saclay, France) with the UHI10 Ti:Sa laser system, previously described in section 2.1.2.1. The laser delivered 65 fs chirped pulse amplification pulses with energy up to 0.7 J at a wavelength of $\lambda_l = 800$ nm. The pulses were focused by an $f/5$ off-axis parabolic mirror producing a quasi-Gaussian spot with size of 13 μm FWHM, accounting for a normalized field parameter of nominally $a_0 \leq 2$. The nanosecond-scale contrast ratio of the pulse ($> 10^6$) ensured that no preplasma was formed by amplified spontaneous emission. Concerning electron acceleration, an improvement in accelerated beam stability and pointing, as well as a stabilization in electron energy is expected with the use of high contrast ratio [109].

Diagnostics of the plasma was performed by means of ultra-fast femtosecond interferometry with a probe perpendicular to the propagation axis. The Mach-Zehnder interferometer allowed us to control the plasma-electron-density distributions shot-by-shot, and was operated with a small portion of the femtosecond pulse, doubled in frequency by a KDP-Type-I 2-mm-thick crystal, in the same way as in the previous experiments on propagation and ionization studies. The probe beam propagated in a perpendicular direction with respect to the main pulse and the gas flow. By means of an optical delay, it was possi-

ble to vary the delay between the arrival of the main CPA pulse and the probe pulse.The schematic layout of arrangement of the experimental devices in the vacuum chamber is shown in fig. 3.1.

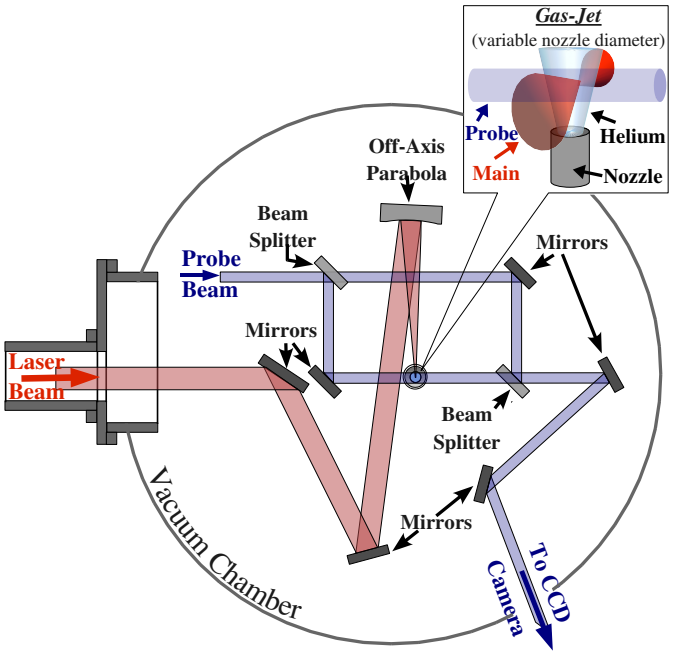

FIGURE 3.1: Layout of the experimental set-up for the acceleration experiment with UHI10 laser system of CEA/Saclay.

3.1.1 The set of supersonic nozzles

In order to perform a systematic study of the acceleration process in its peculiar features of electron injection and dynamics, a set of several supersonic nozzles connected to the ultrafast electro-valve have been used in the experiment. The nozzles had circular aperture with diameters ranging from 0.6 mm to 10 mm. In all cases, the employed gas was helium at a backing pressure ranging from a few (of the order of unity) to 80 bar, depending on the diameter of the nozzle in order to obtain an intense flux of gas in each case. The nozzles had a diameter of 0.6, 1, 2, 3, 4, 5, 6 and 10 millimeters. A wide range in the parameters space for dephasing and acceleration lengths has then been possible to be investigated. It is worth to anticipate that the best results in term of accelerated electron currents have been obtained with the smallest nozzles, with diameter from 0.6 mm to 4 mm. These will then be the ones to which most of the attention is devoted.

The characterization of the plasma electron density distribution obtained with

the various type of nozzles has been performed in detail, since the longitudinal and transverse density profiles have an active incidence on the acceleration process. Furthermore, in order to compare the experimental results with a set of numerical simulations, the plasma features in terms of spatial density distribution must be known with the most accurate precision. A large set of interferograms has been collected, and the fringe patterns have been analyzed with the deconvolution technique explained in appendix A: the phase-difference map is extracted with an algorithm based on continuous-wavelet-transform capable of evidencing local phase variations with a higher degree of accuracy, then the phase maps are processed with an algorithm that generalizes the Abel inversion even to distributions that slightly differ from axial cylindrical symmetry by truncating a Legendre polynomial expansion in the azimuthal angle.

Figures 3.2 to 3.9 show the retrieved electron density profile of plasmas obtained with all the employed nozzles. All interferograms were recorded at a delay of $\approx$ 20 ps between the pump and probe beam arrival on target, and the used gas was helium at different pressures for each nozzle. Helium pressure in the reservoir was 8 bar for the nozzles with 1 and 2 mm diameter, 20 bar for 0.6, 3 and 4 mm diameter nozzles, 75 bar for the 5 mm diameter one and 100 bar for the 6 and 10 mm diameter nozzles. The pressure was chosen in order to obtain plasmas with peak electron density in the range 2-3$\cdot 10^{19}$ cm^{-3}. The higher pressures were used for the larger nozzles, while for the smaller ones the value of pressure was chosen in order to balance also a higher or lower height of laser focus position with respect to the orifice plane: for the 1 and 2 mm diameter nozzles the pump focus nominal position was located 0.5 mm away from the aperture plane and for the 0.6, 3 and 4 mm diameter nozzles it was set at 1 mm away.

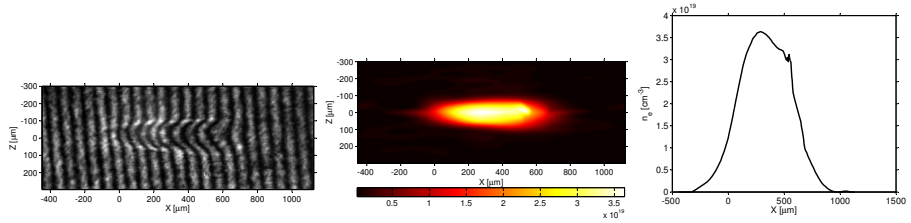

(a) (b) (c)

FIGURE 3.2: Experimental and deconvolved data for the plasma obtained with helium at 20 bar from the 0.6 mm nozzle. (a) Fringe pattern; (b) electron density map; (c) longitudinal density line-out on axis. The laser comes from left-hand side.

It must be noted that for the smallest nozzles, up to the 4 mm diameter one, it has been possible to analyze the full plasma, comprehensive of the initial and final edges, while for the larger apertures only the very first region of plasma

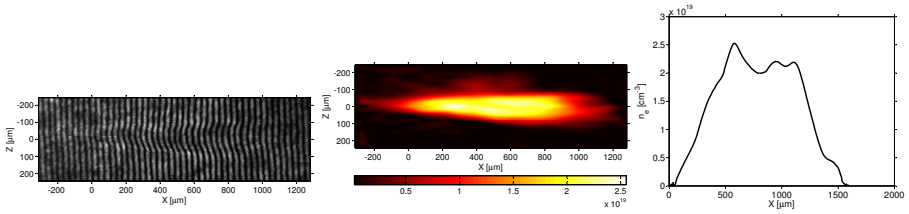

(a) (b) (c)

FIGURE 3.3: Experimental and deconvolved data for the plasma obtained with helium at 8 bar from the 1 mm nozzle. (a) Fringe pattern; (b) electron density map; (c) longitudinal density line-out on axis. The laser comes from left-hand side.

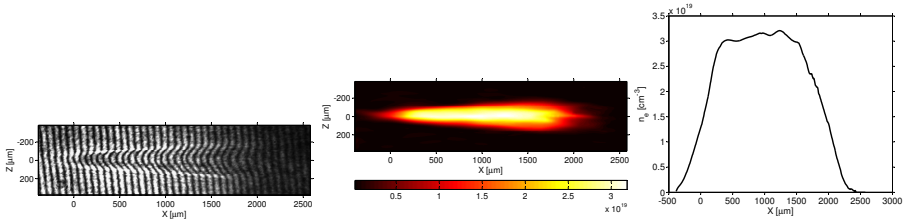

(a) (b) (c)

FIGURE 3.4: Experimental and deconvolved data for the plasma obtained with helium at 8 bar from the 2 mm nozzle. (a) Fringe pattern; (b) electron density map; (c) longitudinal density line-out on axis. The laser comes from left-hand side.

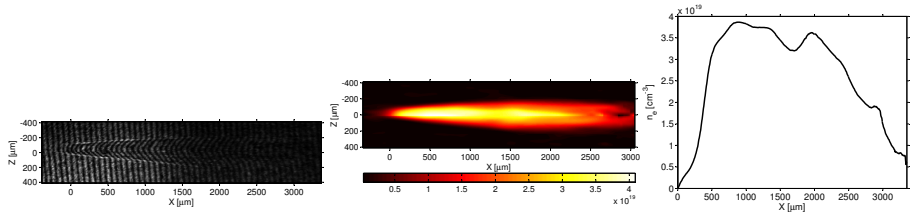

(a) (b) (c)

FIGURE 3.5: Experimental and deconvolved data for the plasma obtained with helium at 20 bar from the 3 mm nozzle. (a) Fringe pattern; (b) electron density map; (c) longitudinal density line-out on axis. The laser comes from left-hand side.

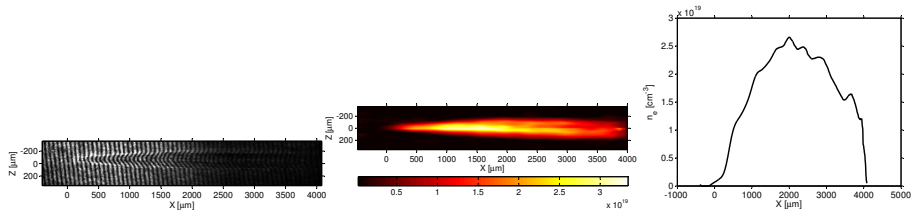

(a) (b) (c)

FIGURE 3.6: Experimental and deconvolved data for the plasma obtained with helium at 25 bar from the 4 mm nozzle. (a) Fringe pattern; (b) electron density map; (c) longitudinal density line-out on axis. The laser comes from left-hand side.

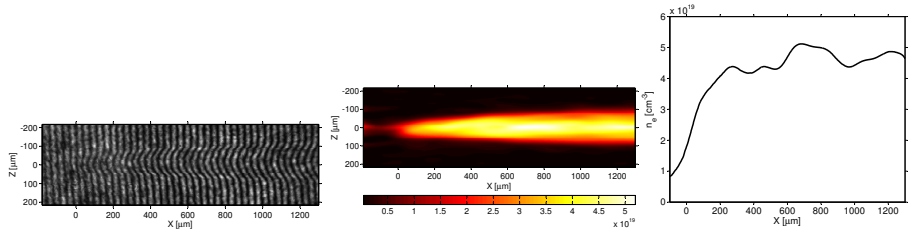

(a) (b) (c)

FIGURE 3.7: Experimental and deconvolved data for the plasma obtained with helium at 75 bar from the 5 mm nozzle. (a) Fringe pattern; (b) electron density map; (c) longitudinal density line-out on axis. Only the first ∼1.2 mm are considered. The laser comes from left-hand side.

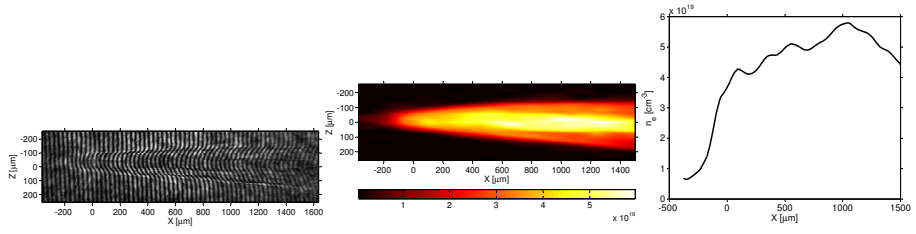

(a) (b) (c)

FIGURE 3.8: Experimental and deconvolved data for the plasma obtained with helium at 100 bar from the 6 mm nozzle. (a) Fringe pattern; (b) electron density map; (c) longitudinal density line-out on axis. Only the first ∼1.5 mm are considered. The laser comes from left-hand side.

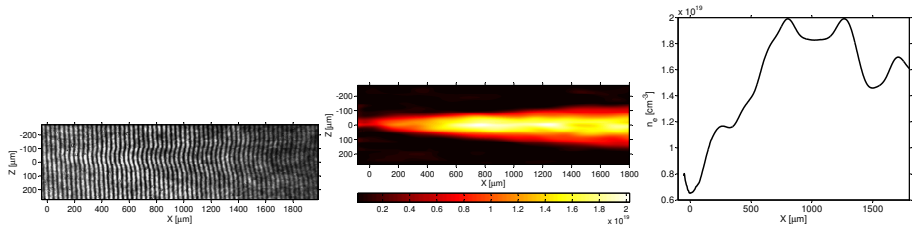

(a) (b) (c)

FIGURE 3.9: Experimental and deconvolved data for the plasma obtained with helium at 100 bar from the 10 mm nozzle. (a) Fringe pattern; (b) electron density map; (c) longitudinal density line-out on axis. Only the first ∼1.7 mm are considered. The laser comes from left-hand side.

extending for approximately less than 2 mm was analysable. This is mainly due to a lack of visibility in the fringes in the external field of view of the interferogram that was not sufficiently illuminated by the probe light. However, it can be anticipated that the best electron signal was observed with the above mentioned smaller nozzles and, moreover, the possibility to deconvolve the density profile over the full plasma length has enabled ad-hoc numerical simulations to be performed starting from the real plasma distribution.

Nozzles with diameter from 0.6 mm to 4 mm exhibit a density on axis that is between 2 and $3.5{\cdot}10^{19}$ cm^{-3}. They are characterized by a well-defined density plateau that extends for almost the nominal dimension of the gas column, except for the raising and descending ramps that are of the order of 250 μm. The density on the plateau is however almost constant. From the retrieved bi-dimensional maps of fig 3.2(b), 3.3(b), 3.4(b), 3.5(b) and 3.6(b), it can be noted that the electron density has a maximum along the longitudinal axis since, at this time, the shock wave that is hydrodynamically set-on by the laser-energy deposition in the focal region has not yet developed enough to deplete the on-axis region and form a hollow channel [81]. It the case of the 2-mm nozzle, the density is almost constant in the high-density plateau. This feature implies that no density fluctuations interfere with laser propagation throughout the plasma. In the case of the 0.6-mm nozzle, the electron density does not reach a complete plateau condition on the axis but the density profile is suitably smooth with a density variation of approximately 20% along 0.5 mm. With the 3 and 4-mm nozzle, the density shows some modulations in the plateau region, accounting for variations of less than 15%, while in the region of laser exit, the density lowers smoothly up to half of its plateau value, because of the defocusing of the laser beam through the gas.

An important note in this description comes from the assumption that the adopted range of experimental pump and target parameters enables the full

ionization of the helium jet on the laser propagation direction. This condition is fundamental for acceleration purposes, since it makes the pump pulse propagation through the plasma free from degradation induced by further ionization, and thus the pump depletion length expressed by equation (1.29) is not limited by energy losses due to gas ionization. The assumption of full ionization is corroborated by the characterization of the gas-jet in terms of atomic (neutral) density of delivered helium. In fact, fig. 3.10 shows the transverse lineout of the neutral density for the 4 mm diameter nozzle, taken at different distances from the orifice plane and at different backing pressures for either helium or argon gas-jets. The analysis of neutral density at different pres-

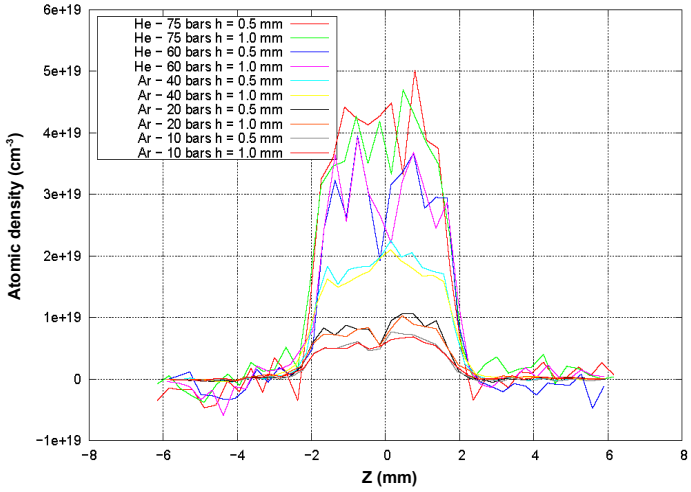

FIGURE 3.10: Atomic density versus transverse position for the 4 mm diameter nozzle at different distances from the orifice plane and at different backing pressures for either helium or argon gas-jets.

sures in the reservoir enables a proportionality relation between atomic density and pressure to be established. In the case of the 4 mm nozzle, the relation $N_{at}[cm^{-3}] \approx 5.2 \cdot 10^{17} \cdot p[bar]$ holds, as resulting from the linear fit plotted in fig. 3.11. Being the interferogram related to the 4 mm nozzle obtained with a backing pressure of 25 bar, it results from the above relation a neutral density of $\sim 1.3 \cdot 10^{19}$ cm^{-3}, that is well in agreement with the retrieved peak electron density found in fig. 3.6(c) (referred to the same nozzle pressure) that slightly exceeds $2.5 \cdot 10^{19}$ cm^{-3}.

Analysis of nozzles with larger diameters (5, 6 and 10 mm) was possible only for the first region, which has been magnified and deconvolved to show the density increase of the plasma in the early 2 mm. In these cases, the helium pressure in the reservoir was almost five times the value for the previous nozzles.

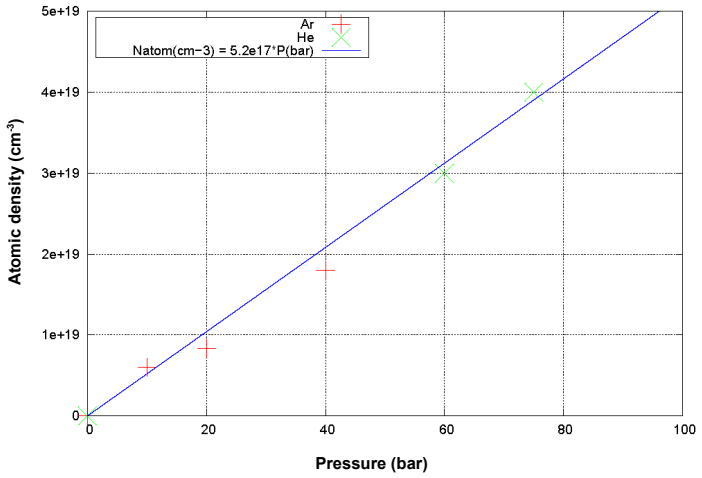

FIGURE 3.11: Linear fit of retrieved neutral density versus backing pressure for helium and argon gas-jets from the 4 mm diameter nozzle.

It implies that the plasma electron density intrinsically reaches higher values, exceeding $4{\cdot}10^{19}$ cm^{-3}.

3.2 Results of electron acceleration

The characterization of the electron bunches that were accelerated in the CEA "laser-into-gasjet" experiment represented the core of data analysis, the search for a regime of stable production of relativistic electrons being the rationale of the whole experiment. As the interferometric data clearly show, the electron density of the plasmas produced in the experiment is well above $7{\cdot}10^{17}$ cm^{-3}, that is the request for the 65-fs laser pulse to resonantly excite high-amplitude plasma waves within the LWFA scheme. However, also such "high-density" conditions have been proved to be suitable for the production of relativistic electron bunches [44, 45, 48]. As it will be shown in the following, in fact, high-charge electron bunches have been accelerated in this conditions. Several diagnostics have been employed in order to get an accurate measurement of the electron bunches key parameters, including number, energy spectrum and angular divergence. The characterization of the electron beams was carried out by making use of four different diagnostics. During the experiment, several scans in focus position of the pump beam with respect to the gas column and in backing pressure in the gas reservoir were performed, in order to maximize the signal that was shot-to-shot provided by two main monitoring device: for

first, a scintillator LANEX screen was used as beam-profile monitor, capable of revealing the presence and the rough collimation of the electron bunches. Then, it was replaced by a magnetic spectrometer in order to get on a shot-to-shot basis the electrons' energy spectrum. Furthermore, the angular distribution and charge of electrons in the bunch were provided by a set of radiochromic foils (RCFs) arranged in a stack with different absorbing materials, called SHEEBA (Spatial High Energy Electron Beam Analyzer) [110]. Another measurement of the electron-bunch parameter was eventually performed, exploiting the nuclear activation of a 197Au sample by means of the bremsstrahlung photons produced by the electron beams in a suitable converter. It has to be noted that these diagnostics on the electron bunches are exclusive one with respect to the other, since each one is destructive for the electron beam. This implies that the use of multiple devices capable of independently give information on the bunch key parameters can be used to cross-check the measurements and to verify their consistency.

In the following, the set-up employed for the beam profile monitor and for the magnetic spectrometer will be briefly described, as well as the most significant related results. Then, the SHEEBA device will be introduced and explained with the analysis procedure carried out to deconvolve the signal left by the high-energy electrons on the RCFs. Finally, the nuclear activation of a gold sample will be described with attention to the extracted results concerning a precise measurement of the number of electrons in the produced bunches.

3.2.1 Results from beam profile monitor

As a first shot-to-shot diagnostics, a beam profile monitor was used to either check the presence of accelerated electron bunches and to estimate their angular spreading. A cooled Andor iDus DV420 CCD camera was used to image the rear surface of a scintillator screen, specifically a Kodak LANEX Fine Screen®. The Andor CCD camera has a chip with 1024x255 active pixels, each one with size of 26x26 μm^2 accounting for a total image area of 26.6x27 mm^{2}was, and it was cooled to -20°C in order to reduce the noise and background signal. The LANEX screen is a scintillator layer made up of gadolinium oxysulfide phosphor powder (Gd_2O_2S:Tb, called "gadox") contained in a urethane binder, protected on front and rear sides by a cellulose acetate coating. An absolute calibration for this kind of scintillator screen has been made by Glinec et al. [111].

The LANEX screen was shielded from direct laser light by a layer of copper of 300 μ thickness, and was located 44 mm away from the end edge of the gas-jet nozzle. The screen was holded by a circular-shaped ring permitting an acceptance region of 30 mm diameter. It turns then out that the angular acceptance of the beam profile monitor was of the order of 700 mrad (approximately a cone of 40° aperture). The schematic representation of the position of the diagnostics

with respect to the electron source is shown in fig. 3.12.

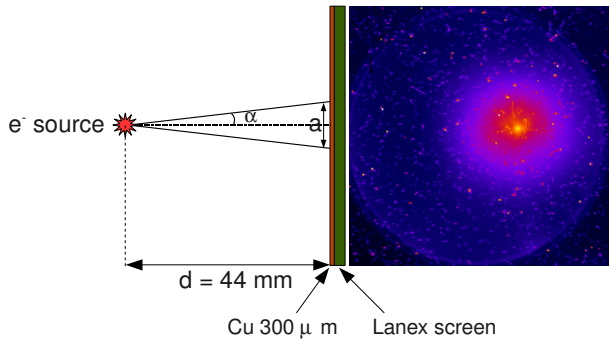

FIGURE 3.12: Sample image of the electron spot as recorded by the CCD imaging the rear surface of the LANEX scintillating screen. The distance d of the beam profile monitor from the electron source, the semi-angle of aperture α of emitted electrons and the spot size on the screen a are also shown.

The beam profile monitor enabled a real-time check of electron divergence and spatial distribution, and permitted a careful scan in pressure and laser focus position with respect to the gas-jet nozzle to be performed to optimize the electron spot in terms of intensity and collimation. In order to evaluate the mean angular divergence of the obtained electron bunches, the angle α has been calculated for the recorded images in different conditions: $\langle\alpha\rangle = \arctan[(a/2)/d]$, being d the distance of the LANEX screen from the electron source and a the FWHM of the electron spot. The solid angle subtended by the bunch is then $\Delta\Omega = \pi \cdot \tan^2\langle\alpha\rangle$. The electron transverse emittance ϵ can be calculated assuming that the size of the source is comparable with the laser spot size ($w_{1/e} \approx 6$ μm):

$$\begin{aligned} \sigma_\theta &= \frac{\langle\alpha\rangle}{2\sqrt{2\ln 2}} \approx 0.42 \cdot \langle\alpha\rangle \\ \sigma_r &= \frac{w_{1/e}}{\sqrt{2}} \approx 4.25 \cdot 10^{-3} \text{ mm} \end{aligned} \tag{3.1}$$

so that $\epsilon = \pi\sigma_\theta\sigma_r$.

To show the pointing stability and the reproducibility of the acceleration process that took place in the interaction, a set of 10 consecutive shots is presented in fig. 3.13. The presented data are raw LANEX screen images in which the scintillation light testifies the collimation and the spatial distribution of the electron spots as emerging from the gas-jet. Data have been obtained with 1 mm diameter nozzle at a pressure from 6 to 10 bar, and in the raw images the spatial conversion factor is 1 pixel=0.165 μm. As it is evident from fig. 3.13, a strong electron signal is shot-to-shot present, with a inner more intense spot

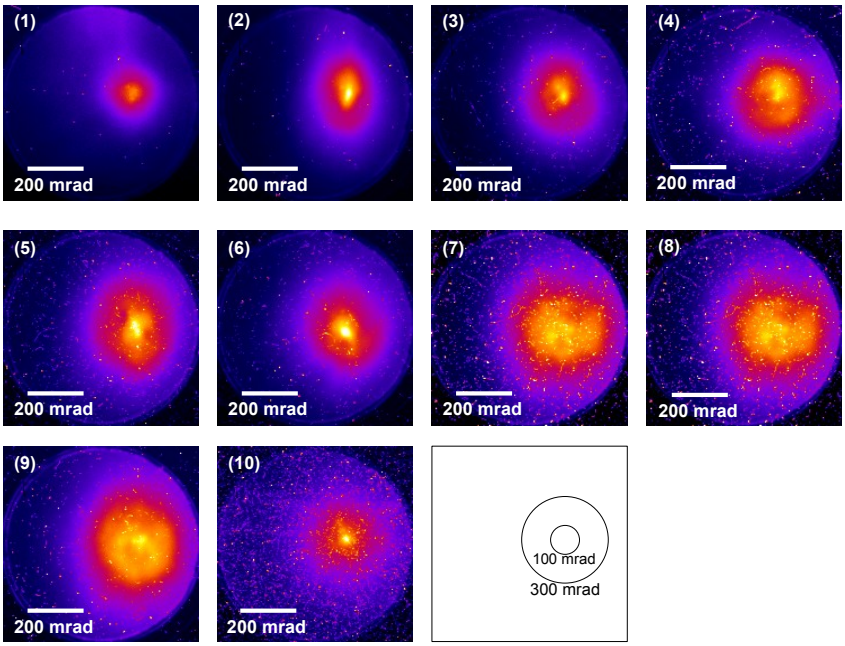

FIGURE 3.13: Beam profile monitor images of ten sequential shots with 1 mm diameter nozzle with backing pressure ranging from 6 to 10 bar. Contours referred to different divergence angles are also shown in the blank square.

due to the presence of one electron bucket with low angular divergence. Among the ten shots, the mean spot size of the most collimated ones, i.e. number 1, 2, 3, 6 and 10, is approximately 3 mm. Figure 3.14 shows the intensity lineout, in arbitrary counts units, of the spot n. 2 of fig. 3.13. This implies that for those

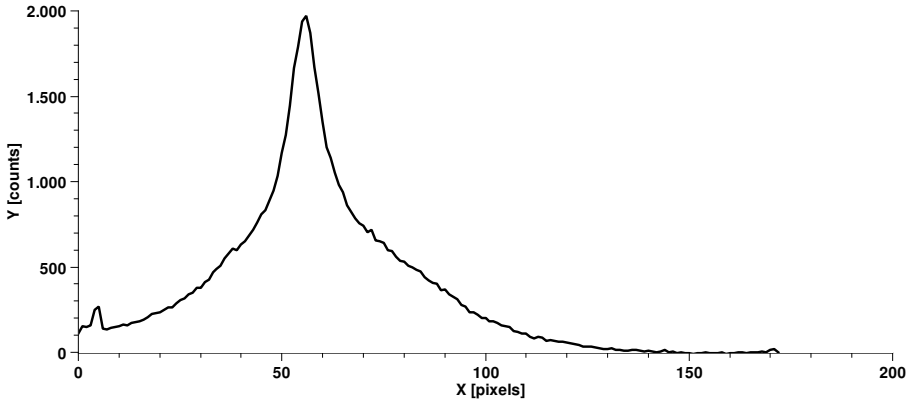

FIGURE 3.14: Intensity lineout, in arbitrary counts units, of the electron signal n. 2 of fig. 3.13.

shots the mean divergence angle is ≈35 mrad (2°), the solid angle is ∼4 mstr and the transverse emittance is $\epsilon = 0.06\pi \cdot \text{mm} \cdot \text{mrad}$. Taking into account the overall series of ten shots in fig. 3.13, the mean size of the inner beam spot is 4.2 mm, accounting for a divergence angle $\alpha \sim 48$ mrad. Even in the less collimated electron signals of number 4, 5, 7, 8 and 9, a central spot with maximum intensity is however always present.

An interesting feature evidenced with nozzles up to the diameter of 4 mm and relatively high gas backing pressures (higher than 40 bar) is the presence of multiple simultaneous spots in the beam profile monitor data. An example of this is shown in fig. 3.15, in which raw data referred to the 2 mm diameter nozzle at 40 bar (fig. 3.15(a)), at 80 bar (fig. 3.15(b)) and 3 mm diameter nozzle at 100 bar (fig. 3.15(c)) are shown.

One possible explanation for the presence of multiple spots in the electron signal can be found assuming that each low-divergence spot is related to each of multiple accelerated buckets. This feature will be confirmed by the 3D numerical simulations presented in section 3.4. Electrons injection is expected to happen in different plasma waves, subsequent to multiple both longitudinal and transverse wavebreaking (see section 1.2.4.1), favoured by the high-density of plasma due to the high pressure in the reservoir.

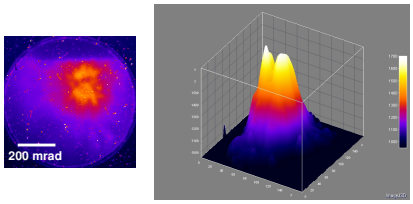

(a)

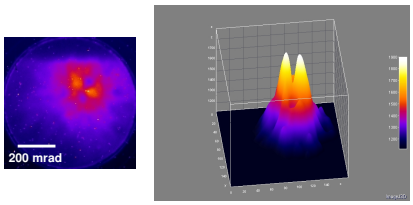

(b)

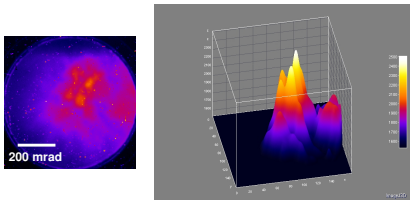

(c)

FIGURE 3.15: Beam profile monitor data referred to: (a) 2 mm diameter nozzle at a helium backing pressure of 40 bar; (b) 2 mm diameter nozzle at 80 bar; (c) 3 mm diameter nozzle at 100 bar. Raw LANEX data are shown side by side to their 3D surface map, for a better visualization of the intensity levels in the image.

3.2.2 Results from the magnetic spectrometer

The shot-to-shot indication of the energy spectrum of the accelerated electrons came from the employment of a magnetic spectrometer associated to the previously described LANEX screen. The layout of the spectrometer is shown in fig. 3.16. The set-up for this diagnostics makes use of 1 T permanent magnet,

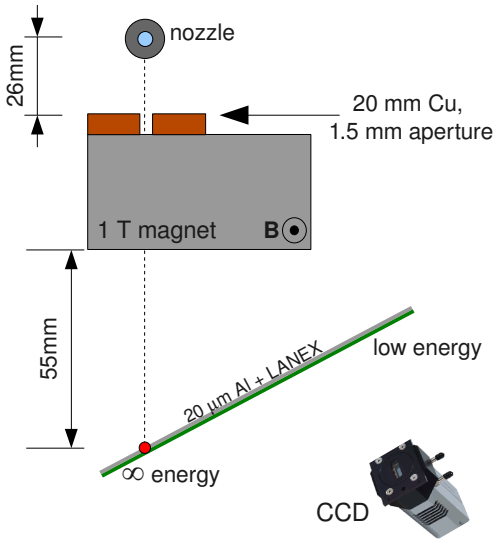

FIGURE 3.16: Sketch of the magnetic spectrometer set-up with arrangement of devices from the nozzle up to the imaging CCD.

placed 26 mm behind the nozzle end edge and with a 20 mm of copper on its front side to form a 1.5 mm aperture as entrance slit for the electron beam. Behind the magnet's rear side the LANEX screen, with a coating of 20 μm aluminium for shielding from the laser light, was placed at an angle of $\sim 36°$ and at a distance of 55 mm (referred to the laser impact point). A tracking code was used to calculate the proportionality relation between the electron deflection on the scintillator screen as recorded by the CCD and the corresponding energy, by taking into account the applied magnetic field and the distance and angles that came into play in the experimental set-up of components.

Results from the magnetic spectrometer add to the beam profile monitor indications concerning the correspondence between the target (nozzle diameter and gas pressure) and the obtained electron spatial and spectral distribution. As shown in the previous section, good spatial collimation was obtained with the smaller nozzles (up to the 4 mm one) and fairly low pressure (not exceeding 40 bar). Occurrence of multiple electron spots and some radial structures was

also noted in the same conditions, while an increase in backing pressure and the use of larger nozzles provided electrons bunches with worse collimation. A correlation can be found with the results form magnetic spectrometer in terms of energy spectrum: the most energetic and monokinetic electron bunches are obtained with the nozzles up to the 4 mm diameter one, with pressure not exceeding 30 bar. In the following, data obtained with the 0.6 mm, 2 mm and 4 mm diameter nozzles are shown. Figures 3.17 to 3.19 present three data that are representative of a large number of shots that provided similar results. These data show quasi-monokinetic signal recorded by the magnetic spectrometer, testified by a roughly single spot that emerges with higher intensity from the streak that extends farther from the position of the laser axis.

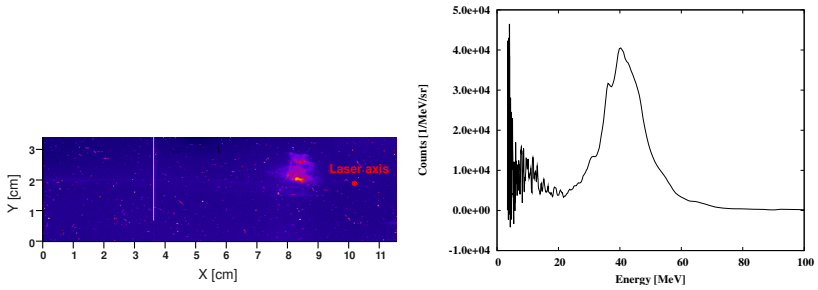

(a) (b)

FIGURE 3.17: Magnetic spectrometer results for laser interaction with gas-jet at 8 bar backing pressure flowing from the 2 mm diameter nozzle. (a) raw data; (b) reconstructed energy spectrum. The position of laser axis is also shown.

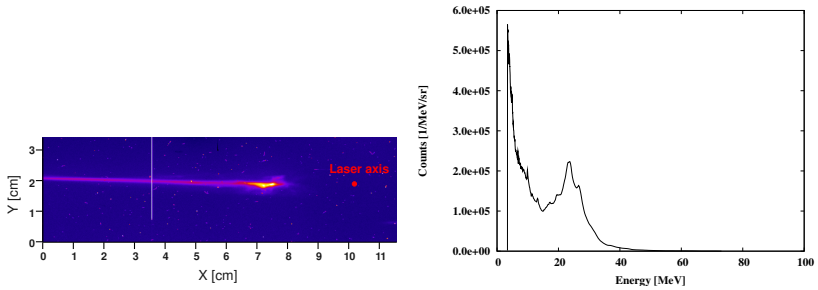

(a) (b)

FIGURE 3.18: Magnetic spectrometer results for laser interaction with gas-jet at 25 bar backing pressure flowing from the 4 mm diameter nozzle. (a) raw data; (b) reconstructed energy spectrum. The position of laser axis is also shown.

Figure 3.17 is referred to a shot performed on helium gas-jet at a backing pressure of 8 bar with the 2 mm nozzle, while fig. 3.18 and 3.19 are referred to different shots with the 4 mm nozzle at a gas pressure of 25 bar. In the former case, a minor distance of the laser focus position from the nozzle plane

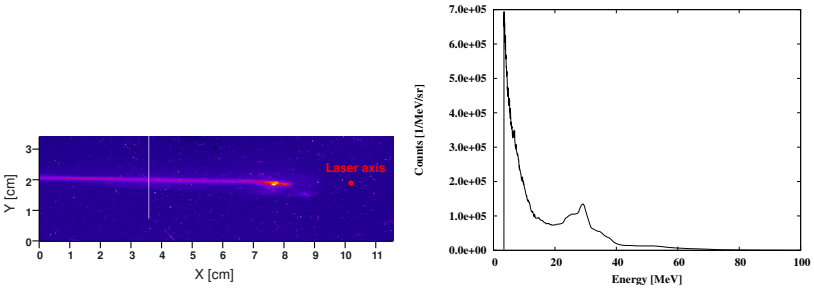

(a) (b)

FIGURE 3.19: Magnetic spectrometer results for laser interaction with gas-jet at 25 bar backing pressure flowing from the 4 mm diameter nozzle. (a) raw data; (b) reconstructed energy spectrum. The position of laser axis is also shown.

(0.5 mm instead of 1 mm) accounts for the lower helium pressure with respect to the latter cases. In figure 3.17(a) a single spot is present, with no low energy component in the electron spectrum, while figs. 3.18(a) and 3.19(a) show a less intense streak that extends for several centimeters from the higher energy peak. This behavior is reconstructed in the energy spectra of figs. 3.17(b), 3.18(b) and 3.19(b), which show a peak energy of $\sim$ 40 MeV in the first case and $\sim$ 25 and $\sim$ 30 MeV for the last two shots with the 4 mm nozzle.

As anticipated above, several shots presented at the same time multiple electron buckets with high energy, approximately in the same conditions in which quasi-monochromatic electron bunches were produced. This feature, evidenced also with the beam profile monitor (see fig. 3.15) was not shot-to-shot reproducible, nor was determined by substantial differences in the interaction condition. A first guess, with afterwards confirmation by numerical simulations, is that multiple electron bunches originating from different plasma wave periods are independently accelerated in the wake of the laser. The difference in energy and spatial position at the exit of the plasma may be due to a premature dephasing by some of them and to minor deflections in emerging from the plasma column. An example of this aspect, from the point of view of electron energy, is represented in the magnetic spectrometer data of figs. 3.20 to 3.22. Raw data 3.20(a), 3.21(a) and 3.22(a) clearly show at least two peaks with the highest intensity, as well as the low energy component. The 1D spatial resolution of the magnetic spectrometer makes it possible to note also a slight angular deflection along the Y transverse axis of the images in figs 3.20(a) and 3.22(a). The presence of the different energy peaks emerges quantitatively in the energy spectra of figs. 3.20(b) to 3.22(b).

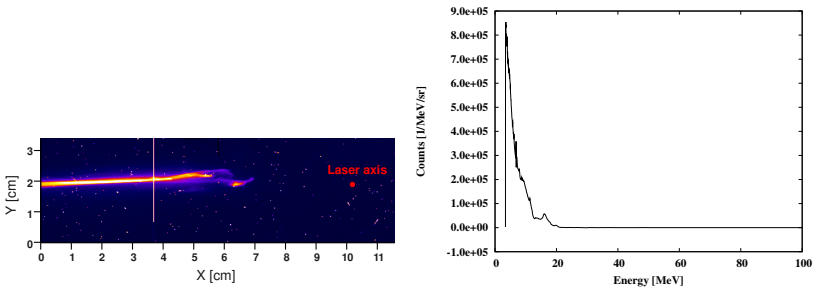

(a) (b)

FIGURE 3.20: Magnetic spectrometer results for laser interaction with gas-jet at 25 bar backing pressure flowing from the 0.6 mm diameter nozzle. (a) raw data; (b) reconstructed energy spectrum. The position of laser axis is also shown.

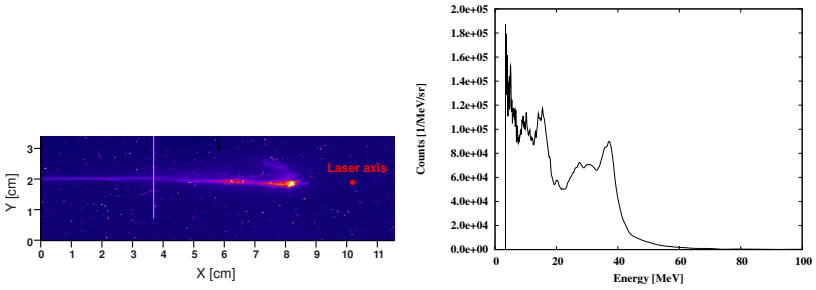

(a) (b)

FIGURE 3.21: Magnetic spectrometer results for laser interaction with gas-jet at 8 bar backing pressure flowing from the 2 mm diameter nozzle. (a) raw data; (b) reconstructed energy spectrum. The position of laser axis is also shown.

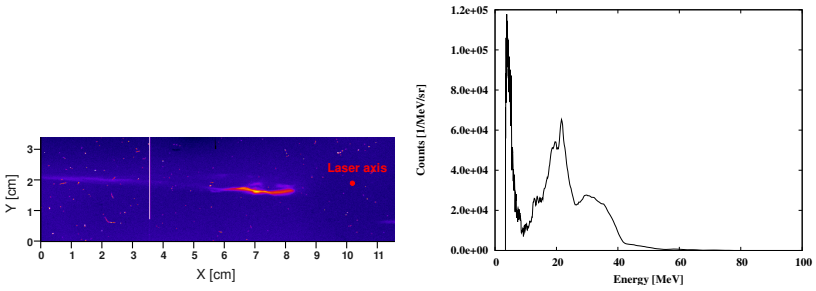

(a) (b)

FIGURE 3.22: Magnetic spectrometer results for laser interaction with gas-jet at 20 bar backing pressure flowing from the 4 mm diameter nozzle. (a) raw data; (b) reconstructed energy spectrum. The position of laser axis is also shown.

3.2.3 Results from SHEEBA electron beam analyzer

The high-energy electrons accelerated in the laser-plasma interaction have been characterized in number, spectrum, and angular distribution using an RCF-based detector named SHEEBA (Spatial High-Energy Electron-Beam Analyzer) [110]. It consists of an array of RCFs (specifically GAFCHROMIC® HD810 and MD55) separated from each other by absorbers of different thickness and materials: mylar foils, aluminum, iron, and lead. The device is described in Appendix B. The operational principle of the SHEEBA detector is the same as for a sampling calorimeter: RCFs are sensitive to charged particles; in particular, the change in their optical density after exposure is proportional to the released energy (absorbed dose). Electrons with higher energy penetrate up to the deepest RCF layers in the stack. The detector is able to provide both the angular distribution, due to its 2-D feature (no pinholes or slit are needed), and the spectrum of the incoming electron bunch. Thus, once the optical density versus dose for a single RCF layer is known and the energy released in each layer of the actual RCFs-absorbers stack is calculated with a Monte Carlo code for a set of discrete kinetic-energy points, then the spectrum of the incoming bunch can be retrieved by means of an iterative algorithm (see Appendix B).

The results obtained with SHEEBA have been correlated with the previous results from both the beam profile monitor and the magnetic spectrometer to check the consistency of the outcomes. As a representative case, results obtained with the 4 mm diameter nozzles will be shown in detail in the following. However, analysis of SHEEBA results obtained with all the nozzles has been performed, and it confirms the previous statement that the larger nozzles are not as performing as the shortest ones in terms of electron acceleration.

As a global warning, it has to be noted that all the data presented herebelow from the SHEEBA device have been obtained for an integration over 10 consecutive laser shots. Being SHEEBA an intrinsically single-shot diagnostics, as it requires the vacuum interaction chamber to be opened for removal of the RCFs for post-irradiance processing, it was chosen to maximize the recorded signal (i.e. the number of recorded events) by maintaining the same RCFs exposed to multiple incident electrons bunches, that is to several consecutive laser shots. Furthermore, the SHEEBA device was placed ∼20 mm after the nozzle entrance, and subtended a solid angle $\Delta\Omega \approx 0.7$ sr.

The reconstructed electron spectra for the bunches accelerated form the largest 10 mm diameter nozzle with helium backing pressure of 100 bar is shown in fig. 3.23, together with the energy spectrum obtained with the 5 mm nozzle operated at 30 bar He pressure. As it is evident from the spectra for the 5 mm and 10 mm nozzles, no monochromatic components are present in either of them.

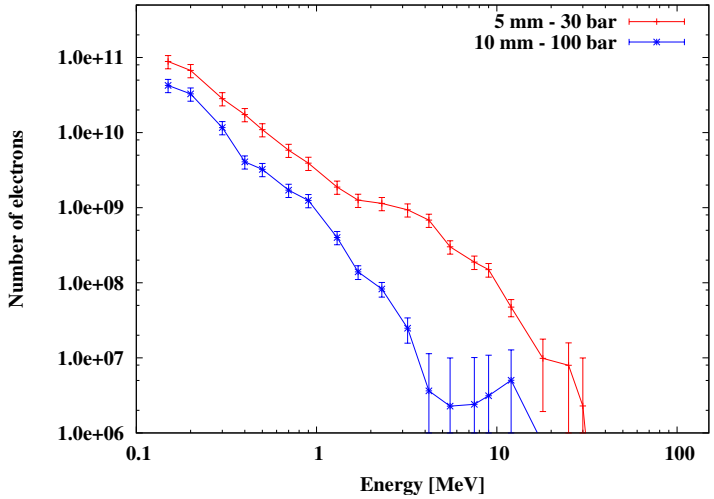

FIGURE 3.23: Electron spectra for the 5 mm diameter nozzle operated at 30 bar helium backing pressure and for the 10 mm nozzle at 100 bar He pressure.

It has to be noted that, even if the spectrum referred to 10 mm nozzle presents a peak at energies around 12 MeV, it is fully masked by the error bars, which lower its significance due to the fact that the reconstructed electron number for that energy does not emerge from the background noise signal. As a reference, the threshold for background was set at 10^6 electrons, below which the calculations of the reconstruction algorithm generated numerical errors with larger magnitude than the signal.

The electron spectrum obtained with the 5 mm diameter nozzle is also plotted in fig. 3.23, to show that even in this case the electron energy distribution is approximately thermal with no particular energy peak except for a slight "knee" from 2 to 8 MeV. A completely different scenario arises when considering the acceleration in the smallest plasmas originated by the gas columns from 0.6, 2 and 4 mm diameter nozzles. Figure 3.24 shows the geometry of the experimental arrangement with respect to the electron source for shots with the 4 mm diameter nozzle. Five exposed RC layers are also shown, with indication of their position in the stack of SHEEBA detector. Furthermore, fig. 3.25 presents the whole set of RCFs taken out from the detector after 10 laser shots on the gas-jet delivered by the 4 mm nozzle. Some considerations can be drawn even from a qualitative point of view from the electron traces in the RCFs of fig. 3.25. As a first point, it is noteworthy that every layer is impressed by the electron passage, as testified by the optical density spots in the center of each film. The spot in the last layers, up to the 19^{th} one, is related to the most energetic electrons, that are not suppressed by the absorber through their path in the whole device length. From a comparison with the earlier layers, it is evident that the most

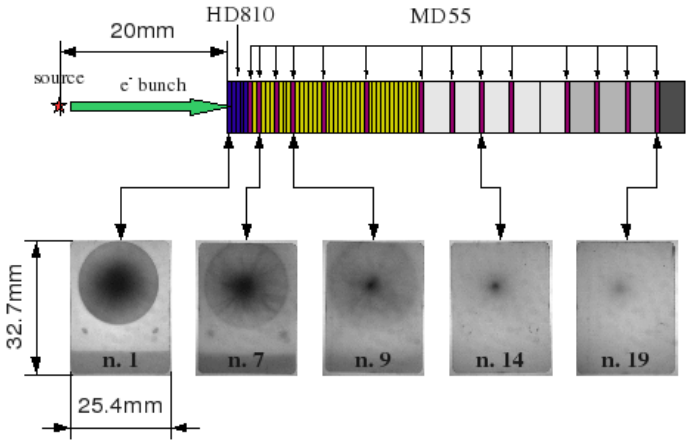

FIGURE 3.24: Raw images of some RCFs after exposure to 10 consecutive laser shots at different depths in the stack. The optical density variation in correspondence to the electron signal is clearly visible on each layer. The sizes of components in the image are not in scale.

energetic and penetrating electron component is present in the central part of the bunch, while the outer regions have an optical density that decreases with RCF number. By the way, the raw data of fig. 3.25 present up to layer #10 some radial structures originating from the central spot and extending up to the circular bounds of the imaging open window. This feature has been also reported by the beam profile monitor diagnostics: it is fairly evident from data in fig. 3.15 and in the following fig. 3.26, which shows three quickly-comparable data with a color scale suitable for visible recognition of such structures. Due to the fact that from the 11^{th} layer onwards the patterns show basically only a single spot in the center, it comes out that the radial structures in the early layers are due to some low-energy electron populations. In fact, they are found to disappear in the subsequent layers on, since only the high-energy electrons survive beyond the absorber materials. The central spot present in all the RCFs is thus the footprint of high-energy, well-collimated, and stable electron bunches integrated over ten laser shots. The pointing position of the electron beams is found to remain very constant, leading to an angular divergence of less than 100 mrad for the ten shots integration. If compared to the single-shot Lanex data, this result is a further convalidation of the electron-beam quality. A possible explanation for the presence of the radial electron structures can be found considering the results of the numerical simulations that are presented in section 3.4, which describe the multiple injection of several electron buckets in a trail of plasma waves behind the laser pulse. This event can thus be responsible

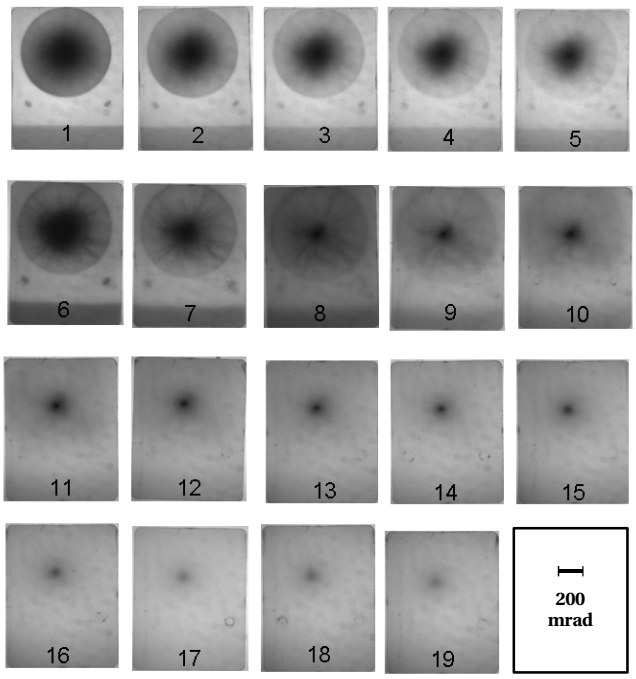

FIGURE 3.25: Raw data extracted from the SHEEBA device after ten laser shots. Layer number increases with distance from the electron source. The position of the two reference nail holes that will be exploited for image alignment by the reconstruction algorithm are also evident in the lower part of each layer. A blank image with angular scale indication is also shown.

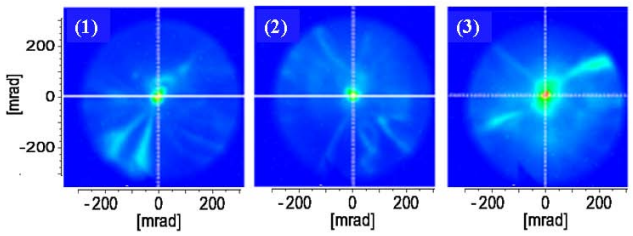

FIGURE 3.26: Electron spots recorded by the beam-profile monitor showing radial structures in the electron signal.

for acceleration to different energies of more than one packet of electrons, whose signal is recorded by the monitoring diagnostics as the ensemble of collimated, high-energy bunches together with uncollimated, radially expanding electron blades.

The spectra obtained for the cases of 0.6, 2 and 4 mm nozzles are shown in fig. 3.27. Except for the 0.6 mm case, both for 2 mm and 4 mm nozzles some

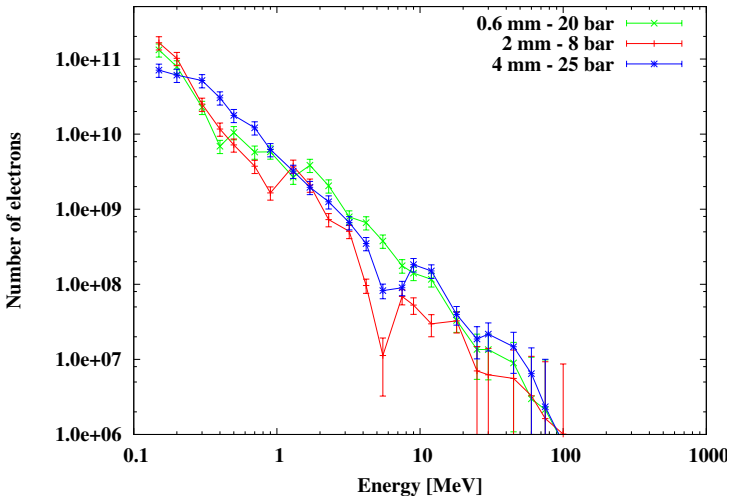

FIGURE 3.27: Electron spectra for the 0.6 mm diameter nozzle operated at 20 bar helium backing pressure, for the 2 mm nozzle at 8 bar He pressure and for the 4 mm diameter nozzle at 25 bar.

monokinetic structures are present, in the former case there is a double peak at energies of ~ 7 and 12 MeV, while in the latter case the peak is centered at about 10 MeV; with both nozzles, a "knee" is present at energies of about 20 MeV. On the opposite of the previous case referred to the larger nozzles, this time the retrieved integrated electron number is significantly above the numerical noise threshold.

The analysis algorithm described in Appendix B extracts from the scanned raw images of the RCFs the number and the angular distribution of electrons at fixed values of kinetic energy. The sampling energies have been chosen to simplify the numerical calculation and range in an interval from 0.1 Mev to $\sim$400 MeV (the last two energies of $\sim$350 MeV and $\sim$400 MeV being taken as highest dummy stop-values). The results are shown in fig. 3.28 for a set of electron energies from 3.2 MeV to 100 MeV.

In the lower energy profiles, the above discussed radial structures are again recognizable, while the central spot is still quite large with more than 200-mrad divergence. As the energy increases, the structures drop away, and the more collimated low-divergence spot remains at the center of the image. It is then

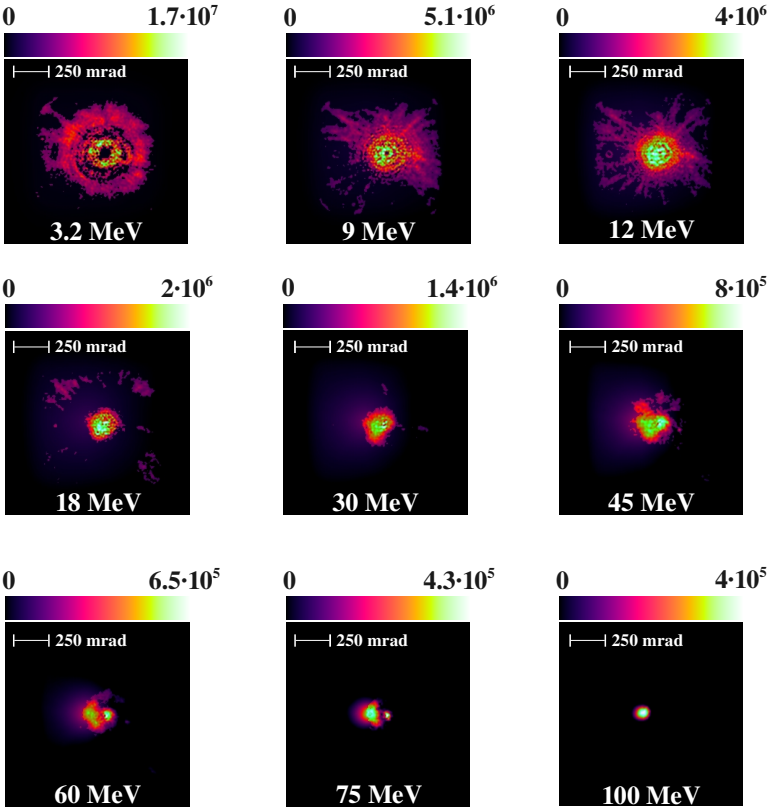

FIGURE 3.28: Spatially resolved spectral data of the accelerated electrons from the SHEEBA detector for energies ranging from 3.2 MeV to 100 MeV. These electron spatial profiles at different energies are referred to the raw data scanned patterns of fig. 3.25.

clear that the electron population with lower energy is less collimated, and partially originates by unstable regions in the laser wake. For this particular series of shots, the analysis reveals the presence at higher energies of at least two spatially separated lobes. This occurrence is fully consistent with single-shot results from the beam profile monitor in fig. 3.15 and can be seen as the result of a very stable process, in which the integration over multiple shots does not smear the angular divergence of the electron bunches that are accelerated with high collimation and stable pointing direction. In case of several consecutive shots, as the ten-in-a-row recorded by SHEEBA, the presence of multiple spot may arise either from single bunches accelerated in different shots and with different pointing, or from multiple bunches from the same shot. The overall good spatial collimation is however a marking point for both the possible explanations and testifies the quality of the results.

Furthermore, as presented above, data relevant to the number and the spatial distribution of electron bunches are possible to be retrieved for different fixed kinetic energies. Then, in order to draw some considerations on the measurement of the electron angular divergence, a two-fold analysis can be performed: a first one, based on electron energy, aimed to measure the angular divergence of single monokinetic bunches, and a second one based on the whole signal (integrated in energy) left by all the electrons in the bunch. This kind of distinction is useful to study the characteristics of monokinetic electrons if an extraction of a given energy component is planned (e.g. by means of bunch shielding).

For first, it is possible to measure the angular divergence of the most energetic electron buckets recorded by SHEEBA (the ones that have enough kinetic energy to penetrate to the deeper layers). Looking at fig. 3.28 and considering only the 60 MeV energy snapshot, it is evident that there are two most intense spots. That image is reported in fig. 3.29 next to the horizontal lineout of the electron distribution taken in correspondence to the double spot. An angular divergence of approximately 50 mrad is retrieved for the more collimated peak. This is in agreement with data from the beam profile monitor. From the lineout of fig. 3.29 the presence of two distinct spots is easily recognizable.

As second consideration, one can consider the integration over electron energy from (*i*) 1.3 MeV to 350 MeV and (*ii*) from 12 MeV to 350 MeV. Both cases are presented in fig. 3.30. From this figure emerges the feature of higher collimation associated with the more energetic electron components in the produced bunch. While in fig. 3.30(a) the overall energy distribution contributes to smear the spatial distribution over a total large spot of a few hundreds of mrad, increasing the threshold to 12 MeV (fig. 3.30(b)) makes the single and more intense spots emerge with possibility of evaluating their much less angular spread.

Finally, the number of electrons resulting from the integration over electron

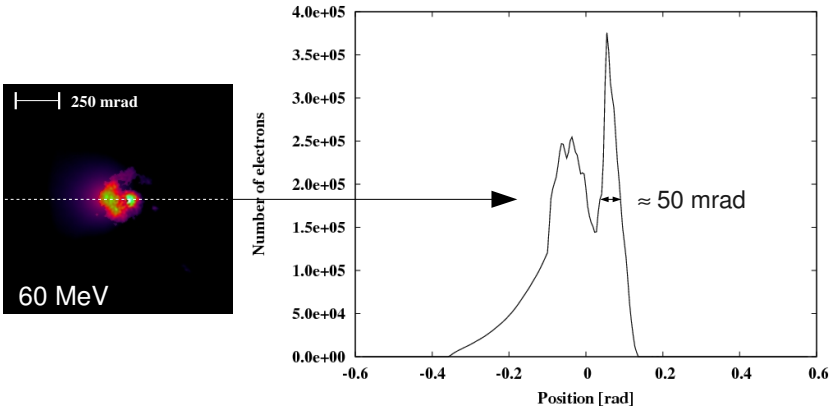

FIGURE 3.29: Horizontal lineout of the electron distribution referred to the 60 MeV reconstructed image from SHEEBA.

energy from 3.2 MeV to 350 MeV is found to be $3.08 \cdot 10^{11}$ for the whole 10 consecutive shots. This data is useful to be compared with the results obtained from the photo-nuclear activation of a ^{197}Au target described in the following section.

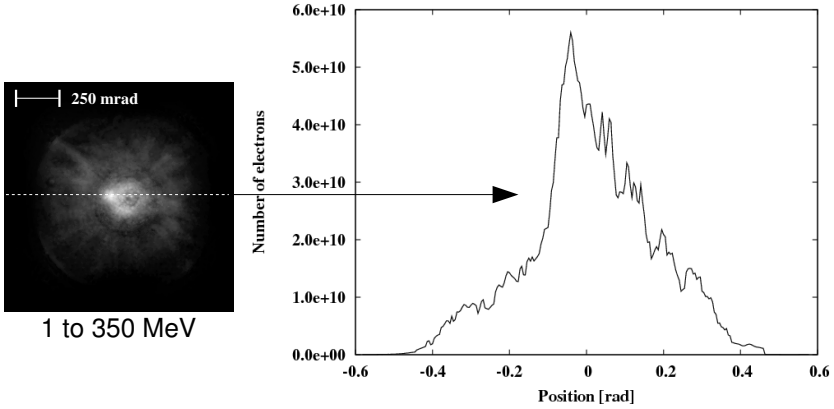

(a)

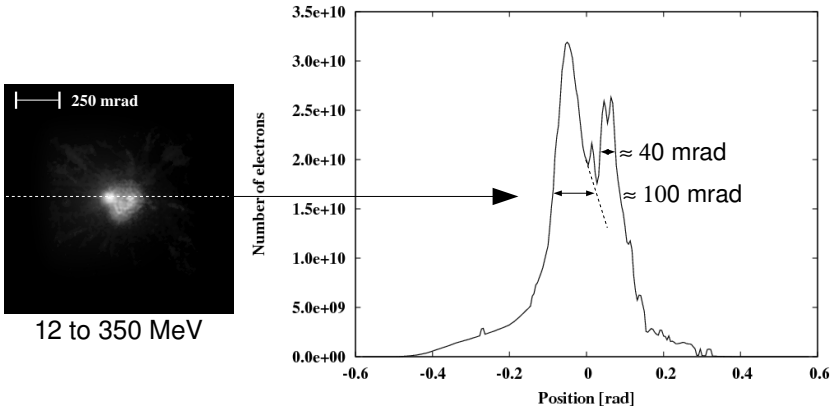

(b)

FIGURE 3.30: Horizontal lineout of the electron distribution referred to the integration of reconstructed image from SHEEBA corresponding to electron energies of (a) 1.3 MeV to 350 MeV; (b) 12 MeV to 350 MeV. The approximate FWHM measurement of angular divergence is also indicated for some recognizable structures.

3.3 Results of photo-activation of ^{197}Au

A further diagnostics has been employed in the experiment: the photo-activation of a sample of ^{197}Au, that has been carried out in collaboration of researchers of the Institute for Transuranium Elements (ITU) of Karlsruhe, Germany. This method enables an accurate measurement of the electron beam flux, including information on the uncertainty associated with this data.

The method consists basically of three separate steps. First, a ^{197}Au foil is irradiated by a flux of bremsstrahlung photons originating from the laser-produced electrons in a tantalum slab "radiator". In this way, radioactive nuclei are produced in the gold sample through the photo-nuclear reaction ^{197}Au(γ,n)^{196}Au. Then, the total radioactivity induced by the bremsstrahlung photons is measured by means of post-irradiation spectroscopy of the gold sample with a high-purity germanium detector. Finally, the absolute number of incident photons (and then indirectly of the primary electrons) is evaluated from the obtained data coupled to a dedicated Monte Carlo modelization of the interaction[1].

The sample of ^{197}Au was chosen for its nuclear properties. In general, in fact, photo-activation is particularly efficient for photons of energy close to the Giant Dipole Resonance (GDR) of many nuclei. The GDR was investigated about 60-70 years ago as a strong resonance, that was denoted to have electric dipole nature [114, 115]. The GDR is enhanced for incoming particles with energy in the range 10-30 MeV, depending on the target material, and the photo-absorption cross section assumes a Lorentzian shape:

$$\sigma(E) = \frac{\sigma_m}{1 + [(E^2 - E_m^2)^2 / E^2\Gamma^2]} \tag{3.2}$$

where E_m, σ_m and Γ are the resonance energy, maximum cross section and FWHM respectively [116]. The experimental cross section for the reaction ^{197}Au(γ,n)^{196}Au is shown in fig. 3.31, from which it can be evinced that E_m = 13.52 MeV, σ_m = 529.2 mb and Γ = 4.5 MeV [117]. Data from the previously described diagnostics on electron bunches indicate that the energy ranges of ^{197}Au GDR and of the produced electrons are suitably matched.

3.3.1 Set-up and obtained results

The layout of the experimental arrangement of radiator and gold slab after the source of electrons is shown in fig. 3.32. A 2 mm thick tantalum foil was placed 35 mm after the nozzle to act as source of bremsstrahlung gamma radiation originating from the interaction with the plasma-accelerated electrons. The ^{197}Au slab, with cross-sectional area of 1.9x1.9 cm^2 and 4 mm thickness, was

[1] Nuclear activation of materials initiated by electrons from a laser-plasma accelerator was demonstrated for interactions on solid [112] or gaseous targets [113].

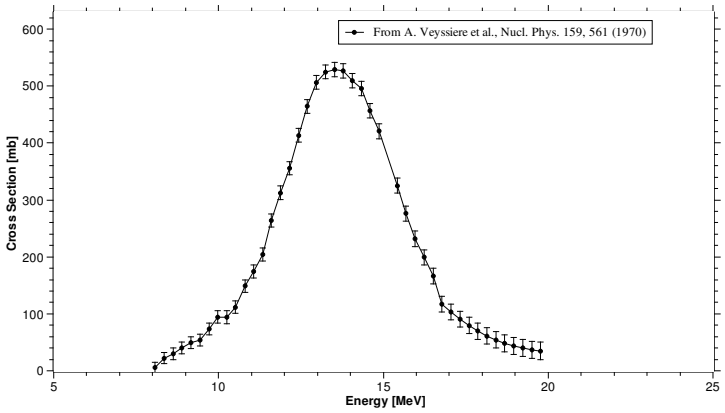

FIGURE 3.31: Experimental cross section for the reaction ^{197}Au(γ,n)^{196}Au (from [118]).

put 50 mm after the Ta radiator and was irradiated by the gamma radiation. Both Ta and gold samples were aligned to be parallel with respect to each other and perpendicular to the laser propagation plane. The energy range of the ac-

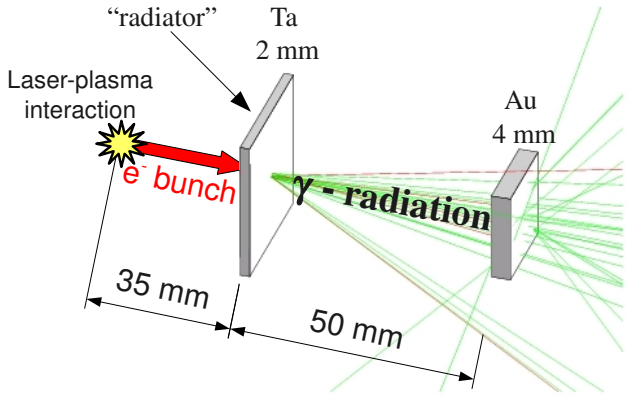

FIGURE 3.32: Experimental set up for photo-activation measurements.

celerated electrons implies that the predominant photo-activation reaction to take place in the gold slab is ^{197}Au(γ,$x \cdot n$)^{196}Au with $x = 1$, even if a small number of reaction involving higher x takes also place.

The set-up for measurement of nuclear activation was exposed to irradiation

for a time period of approximately one hour, during which 106 laser shots were fired. After that, the gold slab has been taken from the vacuum chamber and put in a germanium detector (p-i-n semiconductor diode).In fact, the radio-active nuclei of ^{196}Au, generated out of the stable ^{197}Au population in the slab, emit two primary photons at 333 keV and 355 keV. The spectrum of this radiation was measured by the germanium detector after ensuring low temperature operation of 80 K (to avoid thermally induced leakage currents) and lead shielding from background radiation. The post-irradiation monitoring time in the germanium detector was 143 hours, after which the gamma ray spectrum reported in fig. 3.33 was obtained. To obtain the real number of produced ^{196}Au nuclei, a

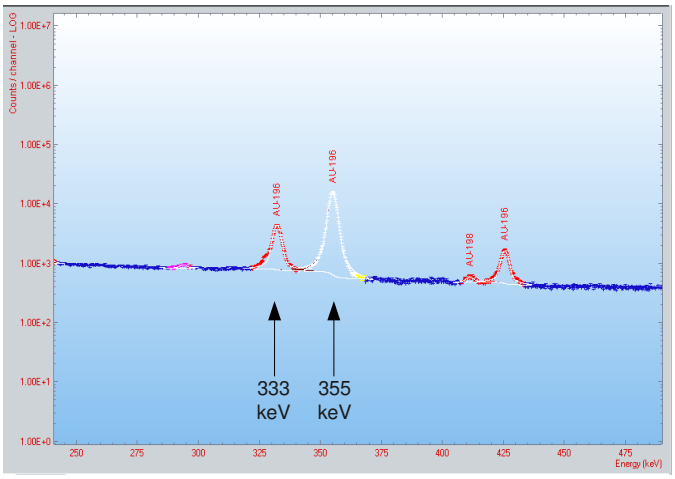

FIGURE 3.33: Gamma ray spectrum in the energy range of interest measured by the germanium semiconductor detector. The characteristic gamma lines at 333 keV and 355 keV are indicated.

corrective factor has to be applied to the measurement of the Ge detector: due to the finite dimension of the (non-pointlike) gold slab, absorption and scattering of the gamma radiation in the gold target were considered in a Monte Carlo code to model the detector response. The result is a factor of 3.25 to be multiplicand by the raw measurements, and the corrected activity is calculated in table 3.1 for both decay lines after background subtraction.

The trend of measured counts by the Ge detector with time enabled also a consistency check of the half-life of ^{196}Au: the retrieved value of 6.09±0.26 days agrees with the tabulated value of 6.17 days from nuclear data sheets [117].

The nuclear activation technique is able to provide the absolute number of electrons (at given energies) that gave rise to the production of the mea-

Gamma line	Relative line intensity	Activity (Bq)	Number of atoms	Uncertainty
333 keV	22.9 %	144.3	$1.11 \cdot 10^8$	4.28 %
355 keV	87 %	161.2	$1.24 \cdot 10^8$	4.24 %

TABLE 3.1: Results from gamma spectroscopy of the produced ^{196}Au nuclei after irradiation of ^{197}Au slab.

sured number of ^{196}Au nuclei. The measured radio-activity, correlated with a Monte Carlo simulation of the interaction performed with the experimental geometry, a relative incoming electron spectrum and the differential cross section of the photonuclear reactions as inputs, weights and corrects the simulation results giving the accurate absolute number of the incoming electrons. The electron bunch spectrum was adjusted in order for the spectrum of the generated bremsstrahlung radiation to fit the measured experimental data, which is shown in fig. 3.34.

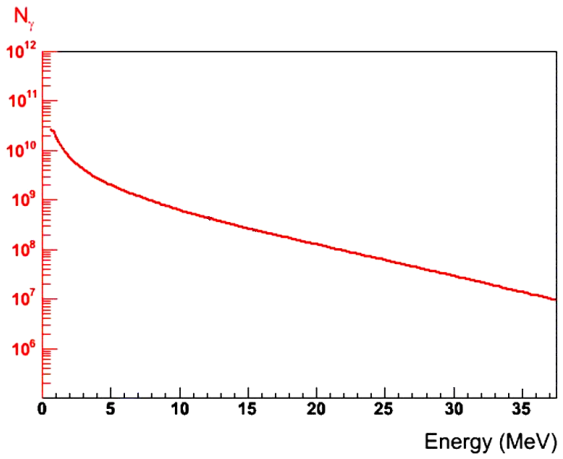

FIGURE 3.34: Spectrum of the bremsstrahlung radiation impinging on the gold slab target as calculated from the (γ,n) reaction yield.

As inputs of the simulation, performed with CERN GEANT4 libraries [119], the cross section of fig. 3.31 and an electron spectrum integrated over 22 consecutive laser shots (to account for shot-to-shot variations) were considered. The integrated image obtained from the sum of the 22 consecutive shots and the related relative spectrum are shown in fig. 3.35. The overall obtained results for bremsstrahlung and electron beam fluxes are specified in table 3.2.

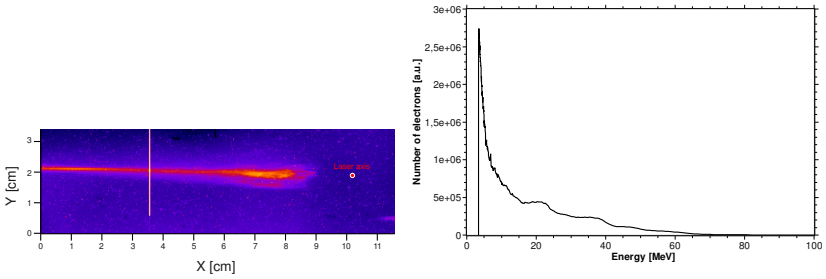

(a) (b)

FIGURE 3.35: Magnetic spectrometer integrated result for 22 consecutive laser shots with 4 mm nozzle at 25 bar. (a) raw data; (b) reconstructed energy spectrum. The position of laser axis is also shown.

	Calculated yield
$N_{(\gamma,n)}$	$(1.24\pm0.05)\cdot10^{8}$
$N_{\gamma}^{8\rightarrow17.5MeV}$	$(2.78\pm0.12)\cdot10^{10}$
$N_{e}^{\geq8MeV}$	$(7.76\pm0.33)\cdot10^{11}$
$N_{e}^{\geq3.4MeV}$	$(3.34\pm0.14)\cdot10^{12}$

TABLE 3.2: Calculated yields for the ^{197}Au(γ,n)^{196}Au reaction and for the corresponding bremsstrahlung and electron beam fluxes.

As it follows from the results of the photo-nuclear analysis, the absolute reaction rate is as high as $1.46 \cdot 10^6$ per joule of incident laser energy, while the number of electrons with energy higher than 3.4 MeV is $(3.15 \pm 0.13) \cdot 10^{10}$. This latter data can be compared with the SHEEBA result referred to the electron number obtained after integration in energy from 3.2 MeV up, which is $3.08 \cdot 10^{10}$ per laser shot, making it evident the consistency of the independent measurements.

Even though the high efficiency of the photo-activation process initiated by electrons from a laser-plasma cathode has been well established [120], however, due to the low cross sections of photo-nuclear processes studied in experiments, a large number of shots are required to obtain a detectable amount of nuclear reactions. In literature, cumulation of 10^3 to 10^4 laser shots are reported for the efficient ignition of a large number of reactions in several nuclear targets [113, 121, 122]. In the presented experiments, only 106 laser shots were sufficient to provide a competitive ^{197}Au(γ,n)^{196}Au reaction rate. The efficiency of the tested electron acceleration process is testified by this comparison [123].

3.4 Results of 3D-PIC numerical simulations

In order to better comprehend the physical mechanisms that come into play in the self-injection and acceleration of the electron bunches during the laser-plasma interaction, a set of numerical simulation has been performed by Nicolas Bourgeois (LULI-École Politechnique, France) and Xavier Davoine with the supervision of Erik Lefebvre (CEA/Bruyères-le-Châtel, France) with the 3-D particle-in-cell code CALDER [124]. The CALDER code is fully relativistic and is parallelized by using a orthogonal and regular spatial domain decomposition [125]. The numerical simulation presented here has been performed with a co-moving frame window with the laser pulse and accounts for the interaction of 10 TW, 65 fs linearly polarized laser pulse, focused in a 15 μm waist to moderately relativistic intensity (I$\approx$8.5$\cdot$10^{18} W/cm^2, $a_0 \sim 1.5$) with a 4 mm long plasma. The longitudinal electron density profile of the plasma was assumed to have linear ramps of 500 μm on entrance and exit edges and a constant plateau with electron density of $\approx$2$\cdot$10^{19} cm^{-3}. This value of density implies $\lambda_{pe} = 7.5$ μm and thus the laser pulse length is approximately more than twice the plasma wavelength. The parameters of the simulation were chosen as follows: the spatial steps were takes as $\Delta x = 0.25$, $\Delta y = 0.18$ and $\Delta z = 0.18$ in units of $\lambda_l/2\pi$ (so that $\Delta x = 0.0318$ being $\lambda_l = 0.8$ μm and x the direction of laser propagation). The time step is $\Delta t = 0.24\ \omega_l^{-1}$, where ω_l is the laser pulsation. The grid was made by 2480x220x220 cells (2480 cells in the longitudinal x direction and 220 in both the transverse directions y and z), resulting in a 79x50x50 μm^3 simulation box, in which 5 particle per cell were considered for the electron density. Finally, ions were treated as immobile background.

Figure 3.36 shows the modification of the laser envelope during the propagation of the pulse in the plasma, and the consequent excitation of plasma waves in its wake. At very early times in the pulse propagation (fig. 3.36(a)), the laser pulse begins to excite plasma waves in its back. After 2.1 ps, the pulse has undergone modest self-focusing and temporal compression, as the plasma electron density grows in its wake. However, it is still approximately two times longer than the λ_{pe}. The pulse compression is enhanced in the following path through the plasma and, jointly, self-phase modulation and pulse compression contribute to split the laser pulse into pulselets capable of exciting large amplitude plasma waves, as shown in fig. 3.36(c). Finally, after $\sim$2.5 mm of propagation, the laser pulse shows significant depletion and defocusing that lead to an attenuation of the plasma wave, as shown in fig. 3.36(d).

The results of the simulation in terms of the electron density distribution in the wake of the driving laser pulse are meaningful for the comprehension of the occurred process of electron injection and acceleration. Snapshots describing the situation of the plasma wake at different times during laser propagation are shown in fig. 3.37. The simulated electron density shows a nonlinear plasma

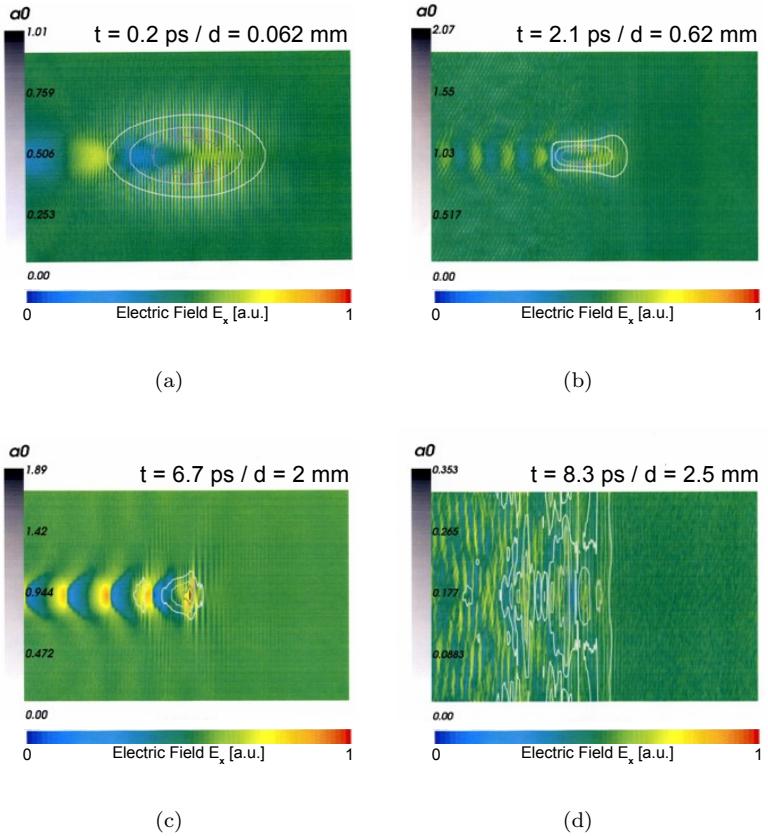

FIGURE 3.36: Snapshots of the electrical field distribution during the laser pulse propagation at (a) 0.062 mm, (b) 0.62 mm, (c) 2 mm and (d) 2.5 mm in the plasma. Contour lines describe different values of a_0 in the laser pulse envelope. The laser comes from the left-hand side.

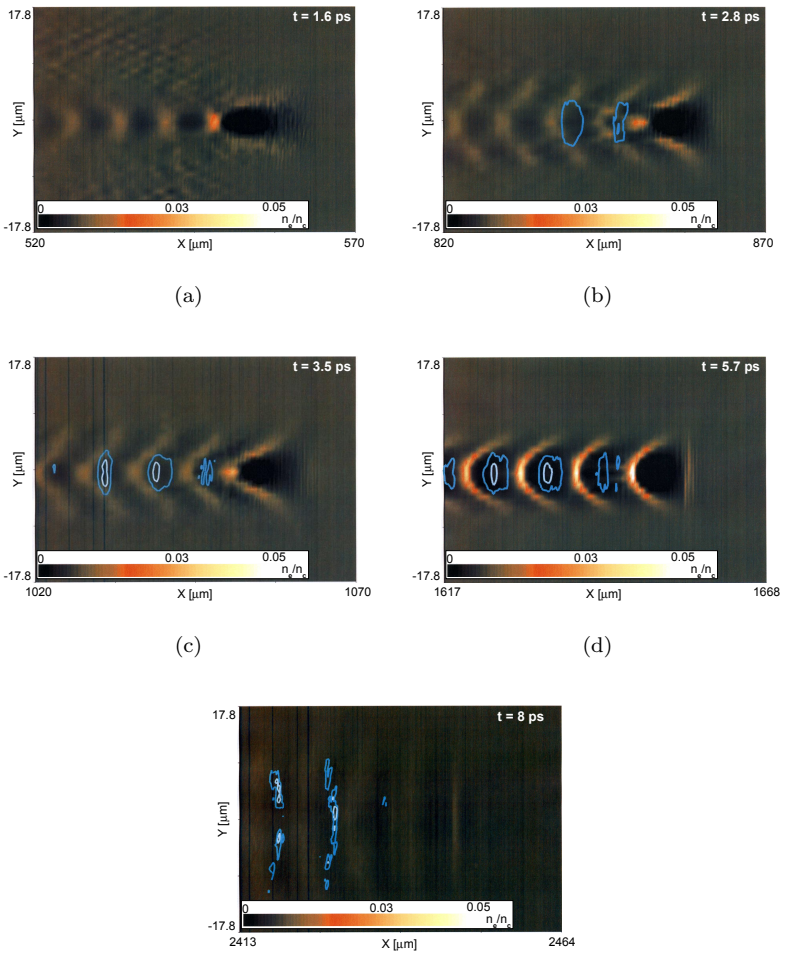

FIGURE 3.37: Snapshots of the electron density distribution in the wake of the laser pulse at different times during its propagation in the plasma. The blue contours identify electron bunches with energy higher than 5 MeV. The laser comes from the left-hand side.

wave growth with a clear progressive transverse bending of the wave front. Looking at the electron plasma wavefronts excited by the laser propagation after 0.5 mm (fig. 3.37(a)) to 1 mm (fig. 3.37(c)), the non-linear nature of the interaction is evident from the steepening of the fronts, correspondent to highly peaked density oscillations. The plasma wave then reaches the wave breaking limit ($5{\cdot}10^{11}$ V/m) and electrons originating from the back of the first plasma wave period are injected into the accelerating region of the wave. Electron trapping begins indeed to occur in the first two buckets behind the laser pulse, and as it travels forward, loads more charge also in the subsequent periods of plasma (the third and the fourth in fig. 3.37(c) and fig. 3.37(d)). The electron density distribution when the pulse is about 1.65 mm after the entrance shows the efficiency of beam loading (the electron bunches with E>5 MeV are identified by the blue contour lines). It has to be noted that, because of the non-linear interaction strongly driven by the laser pulse in the plasma, the wavefronts are clearly curved in the transverse direction assuming the "horse-shoe" profile. The curvature radius of each plasma wavefront evolves with time becoming smaller for farther wave periods. It become than possible also for transverse wavebreaking to occur even in buckets behind the first plasma period [17]. Most of the electrons are in fact efficiently accelerated in the third and fourth plasma periods. As mentioned above, after little more than 2 mm of propagation in the plasma, the laser pulse depletes and defocuses, loosing its capability to sustain large amplitude waves. The accelerated electrons then exit from the plasma maintaining the gained energy and collimation.

The energy gained by the self-injected electrons in the simulation is shown in fig. 3.38 for four significant moments in the simulation. The snapshots show the electron momentum distribution along the propagation axis when the pulse is at about 1 mm (fig. 3.38(a)), 1.65 mm (fig. 3.38(b)), 2.15 mm (fig. 3.38(c)) and 2.45 mm (fig. 3.38(d)), respectively. The electron bunches are accelerated up to 42 MeV, then the depletion of the laser pulse stops the excitation of the plasma wave. The electron bunches are then no longer accelerated and propagate in the last part of the gas-jet.

3.4.1 Discussion on consistency of simulation and experimental results

A set of consideration can be drawn from the comparison of the numerical simulation outputs and the experimental results. First, the determination of the laser pump depletion distance explains the trend of the acceleration efficiency as a function of the nozzle diameters. In fact, from the simulations it turns out that after a propagation distance of approximately 2.5 mm, the pump depletes and doesn't excite high-amplitude plasma waves in the following travel through the gas-jet. This aspect, evident in the snapshot of the simulated electric field

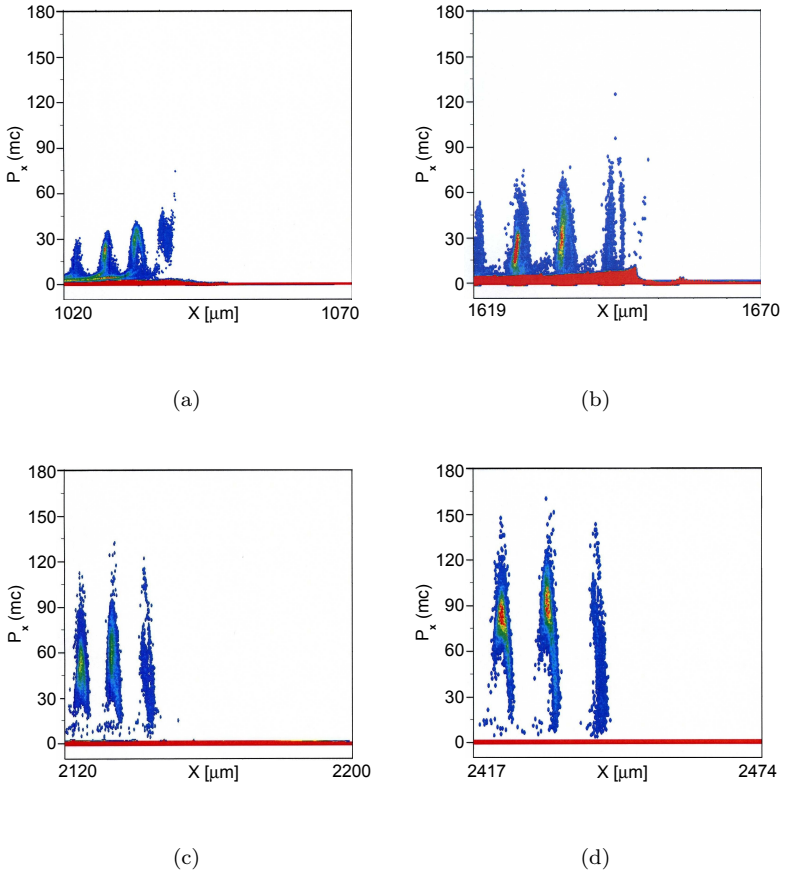

FIGURE 3.38: Electron momentum distribution at different instants in the propagation of the laser pulse through the plasma. Snapshot are referred to distances traveled by the laser of approximately (a) 1 mm, (b) 1.65 mm, (c) 2.15 mm, (d) 2.45 mm.

associated to the laser propagation of fig. 3.36(d), is consistent with the experimental verification that with nozzles larger than 4 mm the output in terms of electron energy gain and spatial collimation was much lower than with the smaller nozzles. Even if in some shots some monochromatic electron bunches have been recorded by the magnetic spectrometer, when ten shots integration is considered (i.e. the SHEEBA results), no monokinetic structures emerges from the thermal spectrum of accelerated electrons: see for example fig. 3.23. The attenuation of the accelerating structure, that even breaks spreading the loaded electrons in neighbour plasma periods or in the background, results in a smearing of the spectrum, even in case of presence of early phase-matched bunches.

A second point of interest that emerges from the numerical modeling of the interaction concerns the simultaneous self-injection of buckets of electrons in several plasma periods which follows the first behind the driving laser pulse. This feature is linked to several experimental observations: (*i*) the presence of multiple spots (see for example figures 3.15, 3.30(b)) and/or radial structures linked to low energy electron blades (figures 3.25, 3.26) in the angular distribution of high-energy electrons after the gas-jet, recorded by the beam profile monitor and by SHEEBA device, (*ii*) the presence of more than one monokinetic component in the spectrum as recorded by the magnetic spectrometer and SHEEBA (figures 3.22, 3.27), (*iii*) the high-charge measured with SHEEBA and with the nuclear activation of a ^{197}Au sample. While the inner, most energetic component of the accelerated electron current remains basically stable in position and with a good collimation, a component made up by electrons with lower energy coming from different plasma periods may result, after propagation through different distances the plasma, in separate spots in the recorded angular distribution. Furthermore, the occurring dephasing of a fraction of electrons (even from different buckets) contributes to the low-energy measured structures. The overall generated current, however, groups all the energetic components in the spectrum and reaches the nC level, taking advantage of the injection of many bunches in subsequent plasma periods. Finally, the non-linear character of the process accounts for the shot-to-shot fluctuation in the peak energy observed in the experiment.

Chapter 4

Perspectives for applications of the laser-plasma source

4.1 Rationale for the chapter

The availability of a source of electrons like the one presented in the previous chapter makes it natural to conceive possible applications in several science and medicine fields. For this discussion, it is useful to distinguish between two main classes of usage of the electrons produced in the laser-plasma accelerator: (*i*) as primary beam, as they come out from the plasma; (*ii*) as source of secondary radiation, after the interaction with a converter medium.

(*i*) Relativistic electron beams are directly used for various purposes. The fields of employment related to medicine are however the most relevant in terms of attracted attention and oriented research. Electron accelerators are used in hospitals either as a clinical tool, in the radiotherapy treatment of oncological diseases [126], and to sterilize medical products from typical contamination by microorganisms on the surfaces of medical instruments [127]. In the following, I will mainly consider the radiotherapeutic application: electrons are in fact used for the treatment of superficial tumors in external-beam radio-therapy (RT) or in the so-called Intra-Operative Radiation Therapy (IORT) directly on the tumor bed during the surgical resection procedure. In section 4.2 the likely benefits from a laser-plasma electron accelerator for RT and IORT treatments are discussed, with emphasis on the potentiality of the electron source described in the previous chapter.

(*ii*) Multi-MeV electrons from a laser-plasma cathode are also used to generate energetic bremsstrahlung photons, via their passage through a thick absorber material with high atomic number. The conversion efficiency of this conversion usually lies in the 10% order and, in case of monochromatic electron bunch, the produced γ-rays have a continuous energy spectrum that ranges from 0 MeV up to the electron energy. Like the previous case, the interest for this kind of radiation is triggered by several perspectives of employment. For example, the possibility to perform high-resolution imaging of biological or complex material samples has been demonstrated: the bremsstrahlung photons have been used to perform radiographies of dense objects with fine internal structures for which a compact γ-source is needed [128]. Alternatively, secondary gammas can be used to initiate nuclear reactions in irradiated suitable samples. This kind of application has been widely investigated in experiments of electron acceleration in laser-solid and laser-gasjet interactions, for two main reasons: the first is the chance to perform nuclear experimental studies on a day-to-day basis, which would never be allowed at a standard electron accelerator facility, with a compact source of radiation with ultra-short duration; the second relies on the possibility to induce with high efficiency nuclear reactions like activation, transmutation, fission and fusion that have, in addition to research impact, also a societal importance (e.g. production of radioisotopes for nuclear medicine or transmutation of nuclear waste product). In section 4.3 a brief review of this application is reviewed.

Beyond the above two classes of usage, it is worth citing a third application that is attracting increasing consideration: the set-up of a free electron laser (FEL) seeded by laser-plasma accelerated electrons. A FEL is a source of tunable, coherent, high power radiation, based on the emission of laser-like radiation by relativistic electrons that undergo a slalom trajectory through an arrangement of magnets called "undulator" [129]. Several schemes are under study to employ laser-plasma accelerators as drivers of FEL radiation, since it would impact on two major issues for FEL technology: limited cost and overall size of the device (electrons are currently accelerated in kilometer-long linear accelerators[1]) and short time duration of the generated radiation. Furthermore, FEL generating X-ray radiation (XFELs) based on laser-plasma electrons are meant to be capable of ultra-high brightness outputs (10^{12} photons/pulse in the 0.1% bandwidth) which, jointly with the intrinsic ultra-short duration, makes them a powerful tool for several scientific tests (e.g. the probing of ultrafast molecular processes) as well as industrial and medical purposes [130]. Much work is being carried on from the theoretical point of view to optimize the

[1] As an example, the European XFEL Project (http://www.xfel.eu) will rely on a 2.1 km long linear accelerator

brightness of the driving electron beams (see for example [131]), although extreme conditions (1 nC of electrons at 1 GeV energy) are required for practically implement a laser-plasma based XFEL [132].

4.2 Application of laser-plasma accelerated electrons in medical radiotherapy

Due to the constant increase of tumor occurrences in worldwide population, clinical treatments based on radio-therapy (RT) with bunches of relativistic electrons are very frequently performed as auxiliary therapy to surgical removal of oncologic diseases. Advances in radio-frequency based linear accelerators (RF-linacs) have made several major industrial suppliers (Varian, Siemens, Sordina, Philips and many others) produce medical devices capable of producing electron bunches with energy from 2 to ∼15 MeV to release dose rates in the treated region of tens of Gy/min. Besides the external RT performed after the surgical removal of the tumor mass, a technique called Intra-Operative Radiation-Therapy (IORT) is an innovative additional option, which consists in direct irradiation of residual specific areas of a tumor bed during a surgical procedure. IORT enables irradiation of a limited volume of tissue next to the tumor area (it has been observed that the 85% of recurrences happen in the scar tissue area [126]) with a major visual control of the target volume and mapping of the irradiation field, from which the surrounding healthy structures can be displaced [133]. In IORT treatments, a typical dose of the order of 20 Gy/min is released in sequences of electron bunches from a RF-linac. From the biologic point of view, single-dose IORT effectiveness is hypothesized to be two to three times the one of fractionated radiotherapy, so that 15 Gy of IORT is equivalent to 30-45 Gy of fractionated external beam irradiation [134].

The requests for a RF-linac are mainly oriented to guarantee stability and reliability of the electron bunches, while the overall dimensions and weight limit the flexibility of usage and the cost of the device exceeds the economic supportability by small medical centers or underdeveloped countries. Furthermore, a RF-linac has to be used in a surgery room and specific equipment are mandatory to satisfy the surgical-theatre requirements to access and operate in a clean environment while preserving either safety radiation protection of personnel and easy performances of control and manoeuvre.

In general, the achievable properties of the electron beams produced in a laser-wakefield accelerator have stimulated wide discussions about the application of laser-driven electron sources in clinical RT and IORT [135, 136, 137, 138, 139]. In principle, laser-plasma accelerators (LPA) can deliver the same dose in the same overall time period with electrons of the same kinetic energy. A series of advantages characterize the use of a LPA in IORT treatments: first, a T^3 laser

system can ensure more compactness and a lighter structure of the mechanical layout. This is also due to the much shorter acceleration length (few mm's) with respect to a RF cavity (order of one meter), and may reflect in a higher mobility and in the possibility to simultaneously serve multiple gantries (i.e. multiple patients) by optically splitting and guiding the laser pulse. Moreover, the all-optical mechanism of generation of relativistic electrons does not require a radio-protected environment except for the source-to-skin distance (SSD). A wide energy range is accessible with a LPA by tuning only the interaction condition (not a severe retuning of the accelerator is needed as opposite to a RF-linac), with the possibility to easily reach higher energies up to 50 MeV in order to reach deep seated tumors [140]. Finally, the absence of thermoionic valves as well as of ultra-high-vacuum requirements enhance the easiness of maintenance operation. However, the main difference is that electron bunches from a LPA are many orders of magnitude shorter (picoseconds) than in the RF-Linac case (microseconds). Consequently, the electron bunch peak current can reach the kA level, one million times higher than the previous case. The effects of such huge currents on biological matter and their therapeutic potential are basically unknown.

In the following, a brief comparison between the currently operating medical RF-linacs and the laser-plasma cathode optimized in the CEA/Saclay experiment will be carried out, stressing the major tasks to be addressed for the clinical purposes with a laser-driven linac.

4.2.1 Discussion on the application of the CEA/Saclay electron source

In chapter 3, the relativistic electrons produced in the experiment performed at CEA-Saclay (France) have been characterized in detail with several advanced diagnostics in energy spectrum, number, angular divergence and stability over many days and laser shots. A charge higher than 1.5 nC per laser shot has been obtained in reproducible, fairly collimated, and quasi-monochromatic electron bunches, whose peak energy moved shot by shot in the range 10-45 MeV. As it is evident from fig. 3.35(b), the electron energy spectrum integrated over a large number of shots was found to peak at 21 MeV, with a FWHM energy spread of $\approx$8 MeV. This kind of integrated spectrum is suitable for IORT class of cancer therapy.

Comparison of the main parameters of electron bunches produced by two commercial RF Hospital accelerators for IORT treatment and those of this laser driven accelerator is shown in the Table 4.1.

As it emerges from the comparison, most of the performances of the experimental laser driven electron accelerator set-up at CEA-Saclay are comparable with presently used conventional accelerators. However, while the dose delivered

Accelerator type	IORT-NOVAC7	LIAC	Laser-driven accelerator
Producer	HITESYS S.p.A	SORDINA S.p.A	ref. [123]
Electron energy	$\leq$ 10 MeV (3, 5, 7, 9 MeV)	$\leq$ 12 MeV (4, 6, 9, 12 MeV)	$\geq$ 10 MeV (10 - 45 MeV)
Peak current	1.5 mA	1.5 mA	>1.6 kA
Bunch duration	4 μs	1.2 μs	$<$ 1 ps
Bunch charge	6 nC	1.8 nC	1.6 nC
Repetition rate	5 Hz	5-20 Hz	10 Hz
Mean current	30 nA (5 Hz)	18 nA (10 Hz)	16 nA (10 Hz)

TABLE 4.1: Basic performances of two commercial medical linacs compared with the laser-plasma electron accelerator set up in the CEA/Saclay experiment described in chapter 3.

for each shot is also comparable, the electron bunch duration is about six orders of magnitude higher in the case of the LPA. Consequently, the peak current is 10^6 times higher. The biological and therapeutic effect of such huge difference is still unknown. In addition, it has to be noted that electrons from a LPA have an intrinsic angular divergence of a few hundreds of mrad. This feature, that represents a drawback in the framework of competition with large-scale accelerators like the CERN's LHC, is in this case an advantage: in fact, standard RF-linacs need the produced electron beams to be widened and then collimated to 2 to 8 cm diameters.

The dose rate delivered by the electron beams accelerated in the CEA/Saclay laser-plasma cathode can be evaluated by multiplying their "effective fluence" on irradiation target by the mass stopping power for water [135]:

$$D = \frac{\epsilon}{e} \cdot \frac{I}{A} \cdot \frac{dE}{\rho dx} \tag{4.1}$$

in which ϵ is the fraction of electrons that reach the target, e is the electron charge, I is the current, A is the target cross section $dE/\rho dx$ describe the energy loss in a medium with density ρ. For a water phantom, $\rho = 1$ g/cm^3 and $dE/dx \sim 2$ MeV/cm. Considering 2 nC of charge at 10 Hz, the 10% of which reaches a region of 25x25 cm^2 of the patient (standard value for external RT), equation (4.1) implies that the released dose rate is approximately 0.1 Gy/min, i.e. more than one over twenty the clinical request. However, if smaller areas of treatments are considered, like the ones irradiated during IORT procedures of 4 to 6 cm diameter [141], significant dose rates for medical purposes can be reached once that an adequate repetition rate is provided.

4.2.2 Perspectives for practical application of the CEA/Saclay accelerator

The implementation of a medical device based on the results obtained in the CEA/Saclay experiment, that will be taken as example for the whole class of laser-plasma sources of high-energy electron beams, should face a series of problems that range from the basic comprehension of therapeutic benefits to mechanical prototyping of the device.

As pointed out before, the major basic task consist to assess the effects of an LPA electron beam characteristics (ultra-high currents administered in ultra-short bunches) on biological targets. Their therapeutic potential is basically unknown and might add relevant information in radiobiology and radiotherapy planning. As principle experiment, the irradiation of biological sample (starting from DNA and molecular samples up to animal with implanted glioma) should be performed, in order to evaluate the induced damage via proteomic analysis and imaging techniques. In fact, damage to normal tissues remains the most important limiting factor in the treatment of cancer by radiotherapy. Vascular injury is one of the most common effects of radiotherapy on normal tissues, and endothelial cells are considered to be very radiosensitive. One possible scenario is that electron beams from a LPA may permit a dramatic reduction of vascular damage. To this purpose, comparative studies between a LPA and a RF-linac should be performed to validate or discourage the application of ultra-short bunches in radio-therapy.

The deliverables of such a systematic study would impact both on basic radiobiology scientific research and also represents a benchmark for the effective employment of LPAs in clinical practice. It is also possible that equivalent therapeutic effects could be obtained at lower dose rate with ultra-short electron bunches with reduced side effects for the patient. Furthermore, the proposed original study represents a milestone toward the possibility of use of a LPA in customized radiation therapy treatments.

From an engineering point of view, some optimizations should be yielded to the layout of a practical device, to make it possible for the outgoing electrons to reach the sensitive region in the patient. In the previous section it has been evidenced that the angular spread of the electron beams from a LPA is intrinsically as wide as necessary for treatment, altough minor adjustments should be performed. The usual technique adopted to resize the beam in medical RF-linacs is to scatter it through a scattering foil system and then collimate it with an external applicator shaped as a 60 cm long tube usually made of Perspex material [142]. The possibility to avoid scattering foils or to shorten the applicator can result in a decrease of unwanted X-ray radiation or secondary electron components with significant different energy. Figure 4.1, taken from [137], shows a

hypothetical layout of a future medical linac.

Moreover, the need to go to high repetition rates for the synchronized laser-gas-jet interaction represents a further problem to be overcome. Up to now, this task is one of the most limiting issues for an effective employment of a LPA in systematic treatments: in fact, high repetition rates are usually off-limits due to the load of gas emitted by the gas-jet in the vacuum chamber, that is not unloaded by the pumps with sufficient velocity.

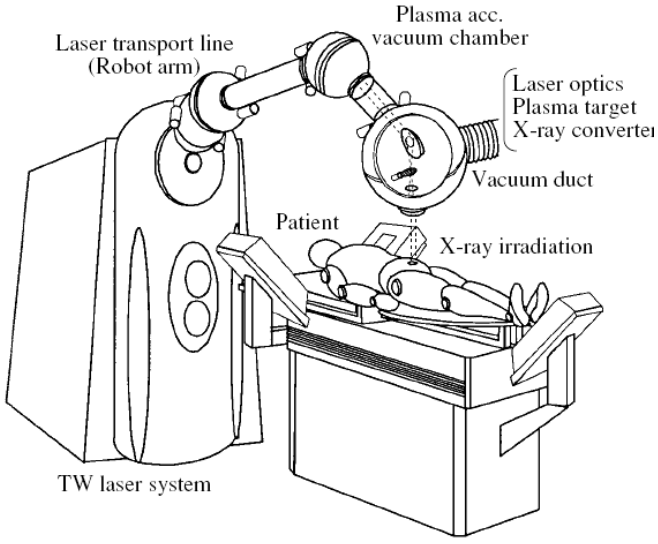

FIGURE 4.1: Artist's view of a laser-driven medical linac prototype (from [137]).

4.3 Application of laser-plasma accelerated electrons for nuclear studies

As anticipated above, the nuclear science obtains from laser driven electron sources a brand new input to perform interesting measurements in the context of many laboratories equipped with ultrashort powerful lasers. The ultrashort duration of the accelerated bunches represents a further attractive feature for these kinds of studies. Although electrons themselves are capable of triggering nuclear reactions, their cross section is at least two orders of magnitude smaller than for photon-induced reactions, which represent the dominant processes [143].

In the following I will focus on nuclear reactions induced by gamma radiation produced by bremsstrahlung of laser-produced electrons in suitable targets. This case is usually mentioned as "photo-activation" and is particularly efficient for photons of energy close to the Giant Dipole Resonance (GDR) of many nuclei. The GDR, already introduced in section 3.3, is common to all nuclei and has form and width that depend on material atomic weight A; this behavior was addressed to collective protons vibrations towards neutrons as a restoring force applies when a particle passes nearby the nucleus. The GDR lies in the range 10-30 MeV for most of the medium and heavy nuclei.

4.3.1 Survey of laser-triggered nuclear reactions relevant for applications

A laser-based activation experiment consists in concept of three stages: the first stage is the "accelerator", in which the laser, interacting with matter, produces relativistic electrons; this can be obtained either in laser-solid and in laser-gas interactions. The second stage, called in the following "radiator", converts the relativistic electrons in γ-rays via bremsstrahlung in a solid. The third stage, called in the following "activation sample" or simply "sample", consists of a target whose material is partially activated by the γ-rays. Efficient conversion is found to take place for converter thickness from 0.3 to 0.5 times the mean range of the incident electrons [144], depending on electron energy. A widely used material for bremsstrahlung conversion is tantalum.

With reference to (3.2), table 4.2 lists the GDR key parameters for photo-absorption reactions for a variety of elements that have been employed in experimental tests with laser-plasma electrons.

As a rule of thumb, the threshold energy for photo-induced reactions decreases with increasing mass number (as a consequence of the decrease in neutron binding energy), while the peak cross-section increases. Energy threshold for heavier nuclides like thorium and uranium is as low as about 5 MeV, so that these nuclei were considered as target in the very first experiments of irradiation with bremsstrahlung photons. The chance of fissioning nuclei with intense lasers was first proposed in 1988 [145], and represents an exciting opportunity which is also promising for applications. Laser intensities exceeding 10^{19} W/cm^2 are required to initiate photo-fission reactions of heavy nuclei. Indeed, first evidence of uranium fission was obtained in extreme intensity laser-solid experiments: Cowan et al. with LLNL Nova Petawatt laser (US) operating at $3{\cdot}10^{20}$ W/cm^2 used a slab of gold as accelerator and radiator and produced $7{\cdot}10^4$ ^{238}U fissions per Joule of laser energy [146], while Ledingham et al. with VULCAN laser at RAL laboratory (UK) used tantalum as accelerator and radiator obtaining approximately the same reaction rate [147]. Finally, Schwoerer et al. used tantalum for both accelerator and radiator but in two separate targets and the Jena

Target Nucleus	Reaction	E_{thr}(MeV)	σ_m(mbarn)	E_m(MeV)	Γ(MeV)
^{12}C	(γ,n)	18.7	8.73	23.4	6
^{63}Cu	(γ,n)	10.8	78.6	16.6	6
	(γ,2n)	19.7	10	23.7	6.5
	(γ,3n)	31.4	-	-	-
^{65}Cu	(γ,n)	9.9	96	17	5
^{129}I	(γ,n)	8.8	-	-	-
^{181}Ta	(γ,n)	7.6	221	12.8	2.1
	(γ,3n)	22.1	21	27.7	5.6
^{197}Au	(γ,n)	8.1	529.2	13.5	4.5
	(γ,2n)	14.7	106.7	16.8	7
	(γ,3n)	23.1	13.6	27.1	>6
^{232}Th	(γ,f)	6	54	14.2	7
^{238}U	(γ,f)	5.8	175	14.3	8.5

TABLE 4.2: Threshold energy, cross-section maximum, resonance energy and FWHM for different photo-induced reactions (from IAEA Photonuclear Data Library [117]). (γ,f) stands for photo-fission reaction.

15 TW laser system at an intensity of 10^{20} W/cm^2. A 50 μm first foil employed for the accelerator and a second slab of 1 mm that acted as radiator [121]. As a result, 10^4 fission events per Joule of laser energy of ^{232}Th and ^{238}U, placed behind the second tantalum layer, were obtained with a reaction rate of the order of 1 event per laser shot.

However, a critical point in the retrieving of the number of nuclear reactions in laser-solid experiments is that there is no control on the spectrum of the electrons accelerated in the interaction, as well as the acceleration mechanism is uncertain and difficult to fit in a predictable scheme. In most cases the electron energy distribution is assumed to be Boltzmann-like and deconvolutions are performed starting from this assumption.

As described in section 3.3, high reactions rate are also achievable in "laser-into-gasjet" experiments, in which electron bunches with a higher energy and a lower angular spread can be generated. To connect with the above mentioned case of indirect laser-induced fission, it's interesting to note how laser-gas jet production of electron can enhance the number of photo-induced fissions in ^{238}U of roughly one order of magnitude with respect of experiments on solid targets cited above: this has been recently proved by Reed et al. [148], by firing only 72 times a 30 fs pulse with intensity of 10^{19} W/cm^2 on a 2 mm He jet at $3{\cdot}10^{19}$ cm^{-3} plasma electron densities. A number of ^{238}U fissions as high as $3{\cdot}10^5$ was obtained by means of a careful optimization of the electron beam spatial profile, total charge and energy by varying nozzle position and gas density.

In principle, all types of photo-induced reactions can be accessible with bremsstrahlung photons produced by laser-plasma accelerated electrons, depending on the relation between the reaction energy threshold and cross-section with photons energy and flux. Table 4.2 lists other obtained nuclear reactions, of the form (γ,xn) with x=1,2,3,.... Among them, transmutation of elements that are of environmental risk, like ^{129}I, have been investigated: for example, ^{128}I was successfully obtained from ^{129}I by Magill et al. in 2003 and by Ledingham et al. in the same year [122, 149]. In the first case the Jena laser delivering 1 J at intensities up to 10^{20} W/cm^2 was focused on a 2 mm tantalum sheet (accelerator and radiator): photo-neutron reactions were found to be 2 per laser shot. In the latter case, a single VULCAN laser pulse of 360 J, focused at $5{\cdot}10^{20}$ W/cm^2 on a 4 mm thick gold target, generated about $3{\cdot}10^6$ nuclei of ^{128}I. In the next section, the relevance of these results is addressed and discussed.

4.3.2 Discussion on the relevance of laser-triggered nuclear reactions

The presented overview on attained results describes a well-established reality in the research currently performed with high-intensity lasers. Beyond the proof-of-principle experiments, in which the feasibility of the processes is demonstrated, practical applications are object of discussion and foresight.

Laser-driven photo-fission of uranium and thorium, in which the fission energy is supplied by the incident photons, enables to decouple from standard neutron-induced fission. The relevance of this novel method relies in the fact that in the first case the cross-sections are higher than for the latter for those two key nuclear waste products [150].

As mentioned above, transmutation of long-lived ^{129}I ($T_{1/2}$=15.7 Ma) has been also obtained. Iodine-129 is a representative case, since it is the most radiotoxic of the fission products and the ratio of stable ^{127}I to radioactive ^{129}I in the environment have increased since 1950s of about two orders of magnitude [151]. In fact, natural abundance of ^{129}I (mainly produced by spallation processes of xenon in the atmosphere and by spontaneous geofissions) have been increased by great amounts of man-made releases, mainly from nuclear tests and reprocessing plants dedicated to nuclear power production, at a rate of 2000 kg/year. The possibility to induce iodine-129 transmutation with high-intensity lasers is thus attracting, but the path for large scale treatment is still long: in general, transmutation of nuclear waste must be taken to industrial scale, while the reaction rates attainable with lasers are many orders of magnitude lower than the required one for an efficient disposal [122].

The medical field can benefit as well of the laser-triggered radio-activation processes, specifically for what concerns the production of radioisotopes usually employed for clinical imaging as positron emission tomography (PET) or

scintigraphy. ^{11}C, ^{13}N, ^{18}F, ^{99}Tc, ^{128}I are typical isotopes used in nuclear medicine, but their abundance is getting remarkably limited, in spite of a world-wide number of diagnostic images as high as 70,000. As an example, consider that in Canada the closure of a single nuclear-reactor facility in 2007 caused the cancellation of 50,000 medical procedures and much panic in physicians and patients [152]. In general, only a few facilities can afford the space and cost requirements (in addition to the safety shielding housing) to host big machines necessary for the production of the above radio-isotopes. In fact, PET isotopes are currently produced in cyclotrons or Van de Graaf accelerators via (p,n) and (p,α) reactions. The possibility to use a high-intensity beam of photons to generate the same yield (800 MBq sources are needed for a patient's dose of radiopharmaceutical) is on the way to future development of extreme-light sources.

Significant advances in laser peak power and repetition rate are needed to cope with the requirements of nuclear research and nuclear medicine. In the next future, table-top laser systems capable of exceeding intensities of 10^{22} W/cm^2 [153] with high repetition rate (more than 1 shot per minute) will make the above requirements accessible with dramatic reduction in costs and devices compactness.

Conclusions

In conclusion, the performed experimental activities concerning the interaction of high-intensity, ultra-short laser pulses with gas-jet and plasmas, aimed to study the propagation and the production of high-energy electrons through wakefield processes have been presented. The effects of propagation of the UHI10 10 TW, 65 fs laser pulse operating at CEA of Saclay (France) in presence and in absence of the pre-plasma produced by its Amplified Spontaneous Emission nanosecond pedestal has been investigated. The presence of the pre-plasma contribute to a spatial filtering of the crossing pulse, while its propagation in absence of the pre-plasma is affected by a series of non-linear effects in the external spatial region of the pulse. The ASE pedestal is found to possibly create favorable conditions in laser wakefield acceleration of electrons by creating pre-formed plasma channels able to optically guide the fs pulse.

Experimental conditions in which relativistic electrons are efficiently generated have been found and characterized in a second experiment carried out with the same UHI10 laser and a supersonic helium nozzle. Several diagnostics have been independently employed to monitor the plasma key parameters and the electron signal. The data analysis shows the consistence of the obtained results. Electron bunches with energies in the range 10-45 MeV and high-charge have been efficiently accelerated even over several days of data-taking. Such particles can be used for many nuclear applications as well as seed for external injection acceleration experiments. The correlation between electron energy and gas-delivering nozzle diameter has been studied also with the aid of a modeling of the experiment via numerical simulations. At last, the use of a laser-plasma based electron accelerator for medical treatment of tumors and for nuclear studies has been considered and discussed.

Appendix A

The interferogram analysis technique

A.1 From fringe pattern to phase map

One of the most common methods to measure plasma key properties such as electronic density and shape or dimension is optical interferometry. Interferometry constitutes an all-optical tool to measure the index of refraction of a plasma without perturbing the probed system. It usually makes use of two electromagnetic waves whose propagation is modified by the electric properties of the plasma. In an interferometer, a probing laser beam is split in two arms, one of which crosses the sample to be analyzed, that then are recombined interfering by coherent superposition of their electric fields. The intensity resulting on a detector is then modulated by the constructive or destructive interference of the two waves, depending on the respective phase. The laser beam that travels through the sample does not perturb it, since the plasma frequency $\nu_{pe} = \omega_{pe}/2\pi \approx 9 \cdot 10^3 \sqrt{n_e[cm^{-3}]}$, where ω_{pe} is given by (1.6), is usually much less than any optical frequency ($\nu = 2.4 \cdot 10^{15}$ for a 800 nm Ti:Sa laser pulse).

To measure the refractive index η of the plasma by the phase delay $\Delta\phi$ of the wave that probes the sample with respect to the reference one, we use the following relation that holds in WKB approximation [154]:

$$\Delta\phi = \int (k_p - k_0)\, dl = \int (\eta - 1)\frac{\omega}{c}\, dl \tag{A.1}$$

in which k_p is the wavenumber of the beam crossing the plasma and $k_0 = \omega/c$ is the wavenumber of the reference beam that travels in vacuum. The index of refraction can be expressed in terms of the plasma electron density since, as it

follows from section 1.2.2,

$$\eta^2 = 1 - \frac{\omega_{pe}^2}{\omega^2} = 1 - \frac{n_e}{n_c} \tag{A.2}$$

where $n_c = 1.1 \cdot 10^{21} \lambda_{[\mu m]}^{-2}$ cm^{-3} is the critical density. It follows that a measure of the electron density can be inferred from the phase delay:

$$\Delta\phi = \frac{\omega}{c} \int \left[\left(1 - \frac{n_e}{n_c} \right)^{1/2} - 1 \right] dl \tag{A.3}$$

that for very underdense plasma ($n_e \ll n_c$) reduces to:

$$\Delta\phi = -\frac{\omega}{2 \cdot c \cdot n_c} \int n_e \, dl \ . \tag{A.4}$$

Once that the relation between $\Delta\phi$ and n_e has been established, the phase shift has to be determined and then the formulas above must be inverted to obtain the plasma electron density. In order to describe the analysis procedure, it is helpful to present an exemplary interferogram, obtained with the set-up described in section 2.3. In figure A.1 the elements that characterize

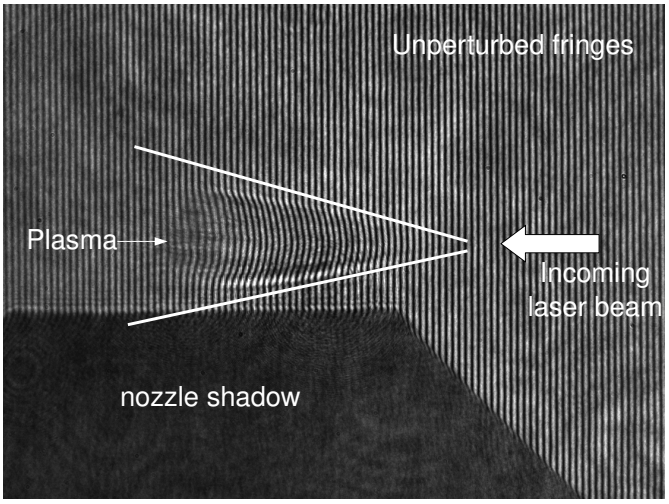

FIGURE A.1: Interferogram obtained with the set-up described in section 2.3. In the figure the nozzle shadow, and the set of fringes both unperturbed and shifted by the presence of the plasma are shown. The withe arrow indicates the propagation direction of the pump pulse, while the white lines show the optical divergence of it after the focus.

the interferogram are shown. The set of fringes that depart from straight lines corresponds to the presence of the plasma, while the nozzle results as a shadow in the picture. The propagation direction of the pump pulse responsible for

the ionization of the gas is indicated by the arrow, while its optical diffraction results in a shaped profile of the curved fringes that follows the beam aperture. The deviation of fringes from straight lines is proportional to the phase shift of the probe beam that crosses the plasma. By analyzing such a pattern with an algorithm capable of quantitatively retrieve the phase shift (it is worth noting how the first quantitative analysis of fringe departure from linearity were made by eye [155]), equation (A.3) can be used to get the electron density spatial distribution for the created plasma.

A bi-dimensional interferometric image represents a continuous intensity function with the form [156, 157]

$$\begin{aligned} I(x,y) &= a(x,y) + b(x,y) \cdot \cos[2\pi(\omega_0 x + \phi(x,y)] = \\ &= a(x,y) + \frac{1}{2} b(x,y) e^{i\phi(x,y)} e^{2\pi i \omega_0 x} + \frac{1}{2} b^*(x,y) e^{-i\phi(x,y)} e^{-2\pi i \omega_0 x} \end{aligned} \tag{A.5}$$

in which $a(x,y)$ and $b(x,y)$ are modulations induced by variations in the background or in the fringe visibility in the interferogram, ω_0 is the spatial carrier frequency of fringes and $\phi(x,y)$ is the phase. In order to extrapolate $\phi(x,y)$ from eq. (A.5), the most common method relies on performing the fast Fourier transform (FFT) of the equation, so that a narrow filter can eliminate the term $a(x,y)$, and then taking the complex logarithm (shifted toward the origin) to have $\log[1/2\, b(x,y)] + i\phi(x,y)$. At this point the phase in the imaginary term is separated from the unwanted modulation $b(x,y)$, and can be reconstructed for the whole interferogram. However, the problem of the evaluation of $\phi(x,y)$ is ill-posed, since the retrieved phase is indeterminate by some factors of 2π that must be added to the calculated value. In fact, in general computer-based routines using the arctangent function return values in the range $[-\pi,\pi]$, so that the phase difference $\Delta\phi(x,y)$ lies in the region $[-2\pi,\pi]$. These values are usually wrapped back to the original $[-\pi,\pi]$ range so that, in the following procedure step, unwrapping of the phase can be performed. The discontinuity can be adjusted by adding an offset value to the calculated phase, depending on the difference of two contiguous sampling points: in fact, this difference is much low than 2π for continuous phase distributions, but grows as high as 2π in proximity of a phase jump. The correct integer multiple of 2π is thus added to each phase value [156].

Although the method based on FFT has been effectively employed in analysis of experimental data [158], in case of local small case structures that depart only a little from the background it can be necessary to resolve those features with more flexibility (for example, this is the case in which there is no clear separation between the scales of noise, background and signal). This improvement is achievable if continuous wavelet transform (CWT) are used instead of FFT. CWT permits to have a spatial resolution added to the frequency description of the obtained signal. This improvement is enabled by the idea of chopping

the signal of interest into several parts to be analyzed separately. The cutting window is chosen to be modulated in a fully scalable way according to the pitch of the signal considered [159]. The signal is thus decomposed into a set of basis functions (the wavelets) obtained from scaling and translation of the *mother*-wavelet $\Psi_{s,\tau}(t)$:

$$\Psi_{s,\tau}(t) = \frac{1}{\sqrt{s}}\Psi\left(\frac{t-\tau}{s}\right) \tag{A.6}$$

in which s is the scale factor and τ is the translation factor. As a choice for ψ, the so-called Morlet base can be taken: $\Psi(k) = \exp(i\omega_0 k)\exp(-k^2/\tau^2)$, while the wavelet coefficients can be calculated via a sampling of the parameters τ and s such as $\tau \to \tau_i, i = 1 \dots N$ and $s \to s_j = 2^{-j/N_v}, j = 1 \dots M$, where N, M, N_v depend on the refinement required by the analysis [91]. In case of a frequency-modulated signal (like an interferogram), the wavelet transform is concentrated in the neighborhood of a curve called the "ridge" of the transform [160]. In the example interferogram of fig. A.1, in which the grey-level map of fringes has an oscillating behavior like (A.5), CWT can be performed and the ridge extracted so that noise and background are automatically ruled out. The ridge sequence for that interferogram is shown in fig. A.2 for a choice of $N_v = 12$.

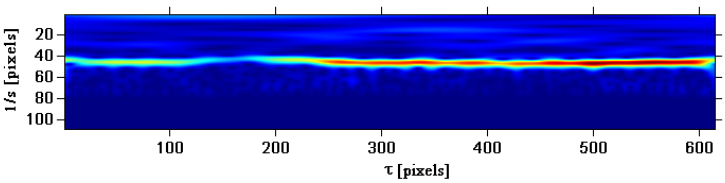

FIGURE A.2: Ridge estimate for the signal recorded in interferogram A.1.

At this point, following the procedure explained in ref. [91], the phase shift map can be extracted for the interferogram: this is plotted in fig. A.3.

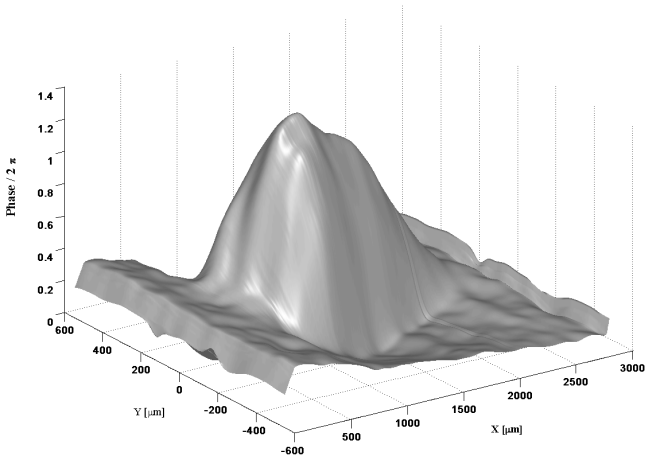

FIGURE A.3: Phase shift map evaluated with CWT method after removal of background and noise perturbations via ridge cutting for the fringe pattern of fig. A.1.

A.2 From phase map to electron density map

In order to invert the equation (A.3), that relates the phase shift induced on a probe beam by the crossing of a plasma with the electron number density of the plasma itself, the search of some symmetries in the sample can ease the computation. Very many laser produced plasmas in gas-jets are assumed to be cylindrically symmetric, since they are created by the expansion of a radial shock wave after the first ionization induced by laser energy deposition in the gas through its propagation. Thus, in a cylindrical coordinate system (r, θ, z) they are independent of θ (and z). This symmetry enables the treatment of the analytical problem to be faced with the well-known mathematical tool of the Abel transform. In this way, the radial distribution of the refractive index of the plasma (and therefore its density) can be deduced from the measured phase shift value along the chords of the path of the probe beam through the medium. In general, Abel inversion gives in a straightforward way the formula for obtaining the radial profile of a quantity (let's call it $q(r)$) once that chord integrals $Q(y)$ of it, given by the integral of $q(r)$ between extremes of the form $\pm\sqrt{a^2 - y^2}$, are known:

$$q(r) = -\frac{1}{\pi}\int_r^a \frac{dQ}{dy}\frac{dy}{\sqrt{y^2 - r^2}} \ . \tag{A.7}$$

For what concerns plasma density reconstruction from phase shift map $\delta\phi$, it translates to:

$$n_e(r, z) = -n_c\frac{\lambda_{pe}}{\pi^2}\int_r^\infty \frac{\partial}{\partial\xi}\delta\phi(\xi, z)\frac{d\xi}{\sqrt{\xi^2 - r^2}} \tag{A.8}$$

where the phase map expands along its symmetry axis y_0 in the plane (y, z) and two half-maps can be determined as:

$$\begin{aligned} \delta\phi^+(\xi, z) &= \delta\phi(y - y_0, z) \quad y > y_0 \\ \delta\phi^-(\xi, z) &= \delta\phi(y_0 - y, z) \quad y < y_0 \ . \end{aligned} \tag{A.9}$$

For a better comprehension of the geometry of the problem that is being considered, as well as for the coordinate system that is used, refer to fig. A.4.

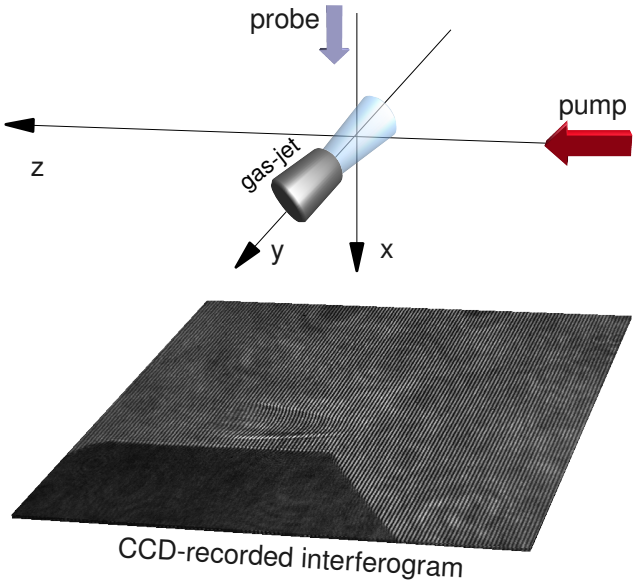

FIGURE A.4: Geometry of the coordinate system considered in the text for the description of the interferogram analysis procedure. The plasma has a rough cylindrical symmetry along the z axis. The pump laser pulse propagates along the z axis, while the probe pulse orthogonally crossed the plasma along the x direction.

The algorithm employed in this thesis for evaluation of plasma electron density maps makes use of a generalization of Abel inversion that extends the ability of deconvolution even to plasma distributions that slightly differ from the cylindrical symmetry. This technique is briefly addressed in the following after the paper by Tomassini and Giulietti of 2001 [92].

The assumption at the basis of the generalization procedure rely on the factorization of the 3D density distribution $n_e(r, z, \theta)$ by a Legendre polynomial expansion in the angular coordinate, such that:

$$n_e(r, z, \theta) = \sum_{l=0}^{L} n_l(r, z) P_l(\cos(\theta)) \tag{A.10}$$

in which $P_l(\cos(\theta))$ are the orthonormal Legendre polynomials. The hypothesis under this factorization is that the density n_e does not present in any point discontinuities or abrupt changes. Then, it can be shown that in (A.10) $L = 1$, so that $n_e(r, z, \theta) = n_0(r, z) + n_1(r, z)\cos(\theta)$ [92].
The terms n_0 and n_1 are finally retrieved from the generalized Abel inversion:

$$\begin{aligned} n_0(r,z) &= -\frac{n_c\lambda_{pe}}{\pi^2}\int_r^\infty \frac{\partial}{\partial\xi}\left(\delta\phi_s(\xi,z)\right)\frac{d\xi}{\sqrt{\xi^2-r^2}} \\ n_1(r,z) &= -\frac{n_c\lambda_{pe}}{\pi^2}\int_r^\infty \frac{\partial}{\partial\xi}\left(\frac{\delta\phi_a(\xi,z)}{\xi}\right)\frac{d\xi}{\sqrt{\xi^2-r^2}} \end{aligned} \tag{A.11}$$

in which $\delta\phi_s(\xi, z)$ and $\delta\phi_a(\xi, z)$ are the symmetrized and antisymmetrized half maps built from (A.9) [91, 161]:

$$\begin{aligned} \delta\phi_s(\xi,z) &= \frac{1}{2}\left(\delta\phi^+(\xi,z) + \delta\phi^-(\xi,z)\right) \\ \delta\phi_a(\xi,z) &= \frac{1}{2}\left(\delta\phi^+(\xi,z) - \delta\phi^-(\xi,z)\right) \end{aligned} \tag{A.12}$$

As it turns out from this description, the procedure to compute the density map of a plasma by exploiting the generalized Abel inversion starts (as the usual cylindrically symmetric Abel inversion technique) from the recognition of a best symmetry axis, at a height in the interferogram called above y_0. Furthermore, this algorithm doesn't take into account any departure from mirror symmetry with respect to a plane orthogonal to the probe propagation axis (plane y-z in fig A.4).

For what concerns the example interferogram of fig. A.1, the electron density profile as reconstructed with the generalized Abel inversion technique is shown in fig. A.5. It is evident that the plasma electron density distribution has an asymmetric shape with respect to its longitudinal axis (z). The resulting electron density is approximately $2 \cdot 10^{19}$ cm^{-3} on axis, with an extension of about 2 mm and a radius of about 500 μm.

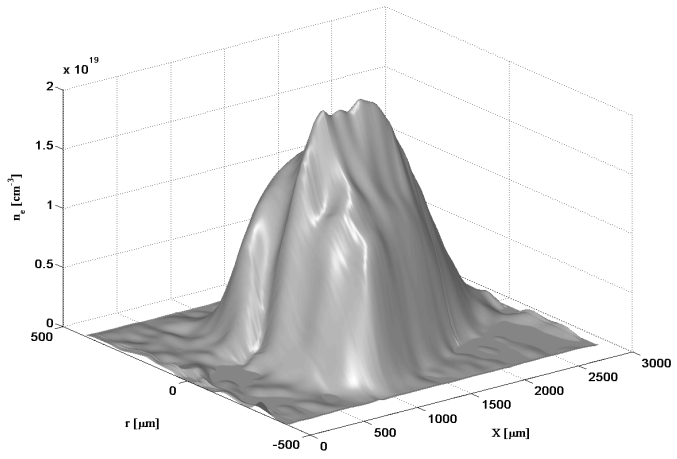

FIGURE A.5: 3D electron density map of the plasma reconstructed from interferogram of fig. A.1.

Appendix B

Description of the SHEEBA device

Further information on the principal characteristics of the accelerated electron bunches, namely their charge, angular distribution and energy spectra, were obtained with aid of a diagnostics developed at the ILIL laboratory of IPCF-CNR in Pisa. The Spatial High Energy Electron Beam Analyzer (SHEEBA) can simultaneously give those information once it is placed behind the electron source [110].

B.1 The layout of the detector

The SHEEBA device is a multilayer detector based on sensitive radiochromic films (RCFs) that acts as a sampling calorimeter. It exploits the properties of RCFs for which, when they are exposed to high-energy particles, the active layers within the film change their optical density due to the absorption of energy. As particles penetrates through matter, they lose energy in their path, depending on the initial particle's kinetic energy. Provided that several layers of RCFs are stacked in an assembly, the depth at which a certain particles has been able to penetrate can be directly linked to its initial kinetic energy. To avoid the employment of a large number of radiochromic films, absorbing materials with different thickness are inserted in the overall device construction, so that stopping shields are interposed between each sensitive layer. It follows that electrons with higher energy penetrate up to the deepest RCF layers in the stack. By accurately knowing the layout of the stack, it is then possible to extract the energy of electrons in an impinging bunch that impressed the sensitive RCFs. One of the simpler advantages of SHEEBA is the possibility to have a quick qualitative information on both the angular spread and of particle's

energy by looking at the exposed films soon right after the interaction.

The set-up employed for the presented experiment is shown in fig. B.1. The

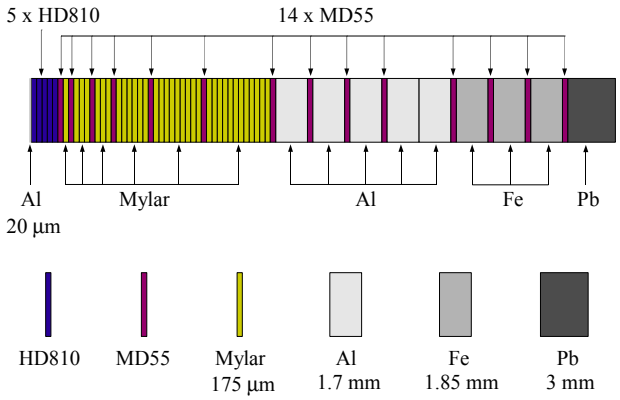

FIGURE B.1: The SHEEBA stack of radiochromic sensitive layers and different absorbing materials. Each component is shown in the lower part of the image.

employed sensitive layers are GAFCHROMIC® HD810 and MD55 radiochromic dosimetry films. The HD810 RCFs are made up of a single 6.5 μm thick active layer coated on $\sim$ 100 μm polyester surface, while the MD55 RCFs are made up by two 16 μm thick active layers (the two faces are thus sensitive to energy deposition) laminated together and shielded by two surfaces of $\sim$ 70 μm clear polyester. When the active layer in HD810 and MD55 films is exposed to radiation, it reacts and forms a blue colored polymer. The main advantages of such kind of films are the following: it does not need after-exposure working out, the released energy density by an impinging electron is proportional to the increase of RCF optical density during exposure and each kind of film is calibrated in energy, being provided the relation between the optical density and the absorbed dose. Furthermore, the detector is able to provide both the angular distribution, due to its 2D feature with no need for pinholes or slit.

The SHEEBA set-up is completed by the absorbers that are interposed between the RCFs, which are mylar of 175 μm thickness, 1.7 mm aluminium, 1.85 mm iron and 3 mm lead layers, whose disposition in the assembly is shown in the upper part of fig. B.1. Figure B.1 also shows the thin 20 μm aluminium foil used to shield the calorimeter from direct laser light.

B.2 The reconstruction algorithm

B.2.1 Results from particles tracking code

The algorithm for electron energy spectrum reconstruction exploits Monte Carlo tracking simulations performed with CERN GEANT 4.2 libraries [119]. Monochromatic electron beams impinging on an array of elements structured like the SHEEBA device are simulated in order to get the released energy density in each radiochromic layer. A good fit for the released energy in each RCF layer by electrons of given initial energy, as it is obtained with the Monte Carlo code, is given by:

$$S_i(E, \mathbf{r}) = A(E, i) \exp\left(-\frac{|\mathbf{r}|^2}{2 \cdot s_w^2(E, i)}\right) , \tag{B.1}$$

in which i is the layer number, $\mathbf{r}$ is the coordinate vector, $A(E, i)$ is the maximum of the released energy distribution and s_w is its width.

The results of Monte Carlo simulations concerning the mean energy released by an electron in each RCF layer for a layout like the one in fig. B.1 are shown in fig. B.2. The first five curves (indicated by numbers 1 to 5 in figure) are relative to the HD810 RCFs, while the subsequent are relative to the MD55 ones. As it

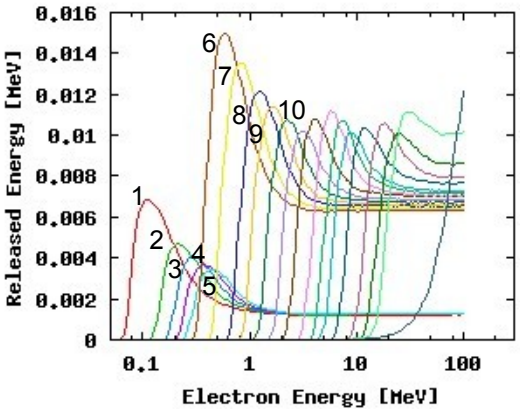

FIGURE B.2: Simulation results for the mean energy released by electrons in each sensitive layer. Layers up to number 10, the first 5 of which are referred to HD810 RCFs, are labelled on their own curve.

appears from the figure, for a given electron initial energy, an amount of energy is released in the device starting from the first radiochromic layers until the particle is stopped at a certain depth from the very first RCF. The higher the energy, the farther layer is reached, being the energy deposition in the earlier layers approximately constant.

B.2.2 Data treatment and analysis

The two main issues to be addressed in order to get to the final deconvolved spectrum of the electron bunch concerns the alignment of the experimentally exposed RCFs to be compared with the simulation results and the comparison and deconvolution of raw optical density distribution with the simulated data. The first issues is faced as follows: each exposed RCF layer of the stack is scanned in transmission with red light (in order to enhance the dosimetry film response) to a TIFF file; then a parameter file is composed in which, for each layer, the position of a region with no signal and regions with the marks of holding nails are indicated. Finally, translations and rotation on each image but the first (that is used as reference) are performed for the overall alignment.

At this point a spectrum reconstruction algorithm has been developed to extract the energy information out of the scanned and aligned raw images of the RCFs. For a layer response to monochromatic and monodirectional electrons like the simulated one of eq. (B.1), the released energy in the ith layer is given by the convolution relation:

$$I_i(\mathbf{r}) = \int f(E,\rho) S_i(E, \mathbf{r}-\rho)\, dE\, d^2\rho \tag{B.2}$$

where I_i is the energy released in the layer i, $f(E,\rho)$ is the energy spectrum of the incoming electrons and S_i is given by eq. (B.1). In eq. (B.2) I_i is retrieved by measuring the optical density of every RCF and S_i is given by the Monte Carlo simulations. The energy spectrum f is then the only unknown that can be calculated by inverting eq. B.2. To do so, a first algorithm has been implemented to get a first rough estimate of the spectrum f: the Fourier transform of eq. B.2 is performed:

$$I_i(\mathbf{k}) = \int f(E,\mathbf{k}) S_i(E,\mathbf{k})\, dE \tag{B.3}$$

in which the only integration variable is the energy E and the deconvolution can be performed separately for every $\mathbf{k}$. With a suitable sampling of the electron energies E [162], it is then possible to invert the formula and to get to a relationship for f. This procedure, being a deconvolution, can be numerically unstable but can be used as starting point for a second algorithm aimed to find the minimum differences between the experimentally obtained images and the reconstructed ones, once that an estimate of the spectrum of the incoming electrons is known. In other words, if a hint for a possible electron spectrum f is given, by finding the absolute minimum of the distance:

$$d^2 = \sum_i \frac{\int |I_i(\mathbf{r}) - Im_i(\mathbf{r})|^2 \mathrm{d}^2\mathbf{r}}{\int |Im_i(\mathbf{r})|^2 \mathrm{d}^2\mathbf{r}} \tag{B.4}$$

in which Im_i is the optical density distribution of the scanned image of the experimentally exposed layer i.

A resume of the operative procedure for SHEEBA data analysis is sketched in fig. B.3.

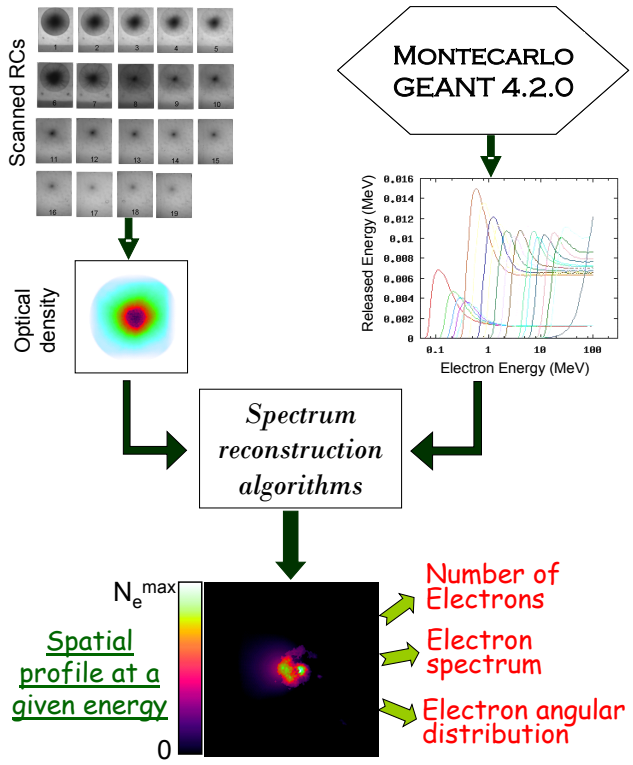

FIGURE B.3: Diagram of the analysis procedure performed to evaluate the key parameters of the electron bunches that impinge on the SHEEBA detector. As a result, the spatial profiles at given incident electron energies are retrieved.

Publications of the author

In the following, the peer-reviewed paper publicated by the author are listed.

1. A.Ya. Faenov, A.I. Magunov, T.A. Pikuz, I.Y. Skobelev, D. Giulietti, S. Betti, M. Galimberti, A. Gamucci, A. Giulietti, L.A. Gizzi, L. Labate, T. Levato, P. Tomassini, J.R. Marquès, N. Bourgeois, S. Dobosz, T. Ceccotti, P. Monot, F. Réau, H. Popescu, P. D'Oliveira, P. Martin, Y. Fukuda, A.S. Boldarev, S.V. Gasilov, V.A. Gasilov *Non-adiabatic cluster expansion after ultrashort laser interaction* Laser Part. Beams, **26**, 69-82 (2008)

2. A. Gamucci, N. Bourgeois, T. Ceccotti, S. Dobosz, P. D'Oliveira, M. Galimberti, J. Galy, A. Giulietti, D. Giulietti, L.A. Gizzi, D.J. Hamilton, L. Labate, J.R. Marquès, P. Monot, H. Popescu, F. Réau, G. Sarri, P. Tomassini, P. Martin *Advanced Diagnostics Applied to a Laser-Driven Electron-Acceleration Experiment* IEEE Trans. Plasma Sci., **36**, 1699-1706 (2008)

3. A. Giulietti, N. Bourgeois, T. Ceccotti, X. Davoine, S. Dobosz, P. D'Oliveira, M. Galimberti, J. Galy, A. Gamucci, D. Giulietti, L.A. Gizzi, D.J. Hamilton, L. Labate, E. Lefebvre, J.R. Marquès, P. Monot, H. Popescu, F. Réau, G. Sarri, P. Tomassini, P. Martin *Intense γ-Ray Source in the Giant-Dipole-Resonance Range Driven by 10-TW Laser Pulses* Phys. Rev. Lett., **101**, 105002 (2008)

4. D. Giulietti, S. Betti, M. Galimberti, A. Gamucci, A. Giulietti, L.A. Gizzi, P. Köster, L. Labate, T. Levato, P. Tomassini *Ionizing radiation sources based on laser produced plasmas and applications* Radiat. Eff. Defects Solids, **163**, 411-417 (2008)

5. A.Ya. Faenov, A.I. Magunov, T.A. Pikuz, I.Y. Skobelev, D. Giulietti, S. Betti, M. Galimberti, A. Gamucci, A. Giulietti, L.A. Gizzi, L. Labate, T. Levato, P. Tomassini, J.R. Marquès, N. Bourgeois, S. Dobosz, T. Ceccotti, P. Monot, F. Réau, H. Popescu, P. D'Oliveira, P. Martin, Y. Fukuda,

A.S. Boldarev, S.V. Gasilov, V.A. Gasilov *X-ray spectroscopic diagnostics of ultrashort laser-cluster interaction at the stage of the nonadiabatic scattering of clusters* JETP Lett., **86**, 178-183 (2007)

6. A. Gamucci, M. Galimberti, D. Giulietti, L.A. Gizzi, T. Hosokai, L. Labate, C. Petcu, P. Tomassini, A. Giulietti *Production of plasma channels in gas-jets* Proceedings of International Conference on Charged and Neutral Particles Channeling Phenomena II, Editor: Sultan B. Dabagov, **6634**, 66341J (2007)

7. A. Giulietti, M. Galimberti, A. Gamucci, D. Giulietti, L.A. Gizzi, P. Köster, L. Labate, P. Tomassini, T. Ceccotti, P. D'Oliveira, T. Auguste, P. Monot, P. Martin *Search for stable propagation of intense femtosecond laser pulses in gas* Laser Part. Beams, **25**, 513-521 (2007)

8. A. Gamucci, M. Galimberti, D. Giulietti, L.A. Gizzi, L. Labate, C. Petcu, P. Tomassini, A. Giulietti *Production of hollow cylindrical plasmas for laser guiding in acceleration experiments* Appl. Phys. B, **85**, 611-617 (2006)

Bibliography

[1] T. Tajima & J. Dawson. *Laser electron accelerator.* Phys. Rev. Lett. **43** (4), 267–270 (1979)

[2] D. Strickland & G. Mourou. *Compression of amplified chirped optical pulses.* Opt. Comm. **56** (3), 219–221 (1985)

[3] L. Keldysh. *Ionization in the Field of a Strong Electromagnetic Wave.* Sov. Phys. JETP **20**, 1307–1314 (1965)

[4] S. Augst, D. Strickland, D. Meyerhofer, S. Chin & J. Eberly. *Tunneling ionization of noble gase in high-intensity laser field.* Phys. Rev. Lett. **63** (20), 2212–2215 (1989)

[5] W. Kruer. *The physics of laser plasma interaction.* Addison-Wesley Publishing Company (1988)

[6] D. Bohm & E. P. Gross. *Theory of plasma oscillations. A. Origin of medium-like behavior.* Phys. Rev. **75** (12), 1851–1864 (1949)

[7] F. Pegoraro. *Equations of state for high-temperature plasmas.* In S. Eliezer & R. Ricci (Editors), *Proceedings of the International School of Physics "Enrico Fermi", Course CXIII*, 465–486. North-Holland, Amsterdam (1991)

[8] J. Huba. *NRL Plasma Formulary.* Beam Physics Branch, Plasma Physics Division, Naval Research Laboratory, Washington, DC 20375 (2007)

[9] R. Bingham, U. De Angelis, M. R. Amin, R. A. Cairns & B. McNamara. *Relativistic Langmuir waves generated by ultra-short pulse lasers.* Plasma Phys. Control. Fusion **34** (4), 557–567 (1992)

[10] E. Esarey, P. Sprangle, J. Krall & A. Ting. *Overview of Plasma-Based Accelerator Concepts.* IEEE Trans. Plasma Sci. **24** (2), 252–288 (1996)

[11] W. B. Mori & T. Katsouleas. *Wavebreaking of longitudinal plasma oscillations.* Physica Scripta **T30**, 127–133 (1990)

[12] A. I. Akhiezer & R. V. Polovin. *Theory of wave motion of an electron plasma.* Sov. Phys. JETP **3** (5), 696–705 (1956)

[13] J. Dawson. *Nonlinear electron oscillations in a cold plasma.* Phys. Rev. **113** (2), 383–387 (1959)

[14] J. Dawson. *One-dimensional plasma model.* Phys. Fluids **5** (4), 445–459 (1962)

[15] J. R. Marquès, J. P. Geindre, F. Amiranoff, P. Audebert, J. C. Gauthier, A. Antonetti & G. Grillon. *Temporal and Spatial Measurements of the Electron Density Perturbation Produced in the Wake of an Ultrashort Laser Pulse.* Phys. Rev. Lett. **76** (19), 3566–3569 (1996)

[16] N. Matlis, S. Reed, S. Bulanov, V. Chvykov, G. Kalintchenko, T. Matsuoka, P. Rousseau, V. Yanovsky, A. Maksimchuk, G. Shvets & M. Downer. *Snapshots of laser wakefields.* Nat. Phys. **2**, 749–753 (2006)

[17] S. V. Bulanov, F. Pegoraro, A. Pukhov & A. S. Sakharov. *Transverse-Wake Wave Breaking.* Phys. Rev. Lett. **78** (22), 4205–4208 (1997)

[18] A. Yariv. *Quantum Electronics.* 3rd edition. John Wiley and Sons (1989)

[19] E. Esarey, P. Sprangle, J. Krall & A. Ting. *Self-Focusing and Guiding of Short Laser Pulses in Ionizing Gases and Plasmas.* IEEE J. Quantum Electron. **33** (11), 1879–1914 (1997)

[20] P. Sprangle, E. Esarey, J. Krall & G. Joyce. *Propagation and guiding of intense laser pulses in plasmas.* Phys. Rev. Lett. **69** (15), 2201–2203 (1992)

[21] C. G. Durfee III & H. M. Milchberg. *Light pipe for high intensity laser pulses.* Phys. Rev. Lett. **71** (15), 2409–2412 (1993)

[22] P. Volfbeyn, E. Esarey & W. Leemans. *Guiding of laser pulses in plasma channels created by the ignitor-heater technique.* Phys. Plasmas **6**, 2269–2277 (1999)

[23] V. Kumarappan, K. Kim & H. Milchberg. *Guiding of Intense Laser Pulses in PlasmaWaveguides Produced from Efficient, Femtosecond End-Pumped Heating of Clustered Gases.* Phys. Rev. Lett. **94**, 205004 (2005)

[24] H. Sheng, K. Kim, V. Kumarappan, B. Layer & H. Milchberg. *Plasma waveguides efficiently generated by Bessel beams in elongated cluster gas jets.* Phys. Rev. E **72**, 036411 (2005)

[25] F. Amiranoff, S. Baton, D. Bernard, B. Cros, D. Descamps, F. Dorchies, F. Jacquet, V. Malka, J. R. Marquès, G. Matthieussent, P. Miné, A. Modena, P. Mora, J. Morillo & Z. Najmudin. *Observation of Laser Wakefield Acceleration of Electrons.* Phys. Rev. Lett. **81** (5), 995–998 (1998)

[26] B. Cros, C. Courtois, G. Malka, G. Matthieussent, J. R. Marquès, F. Dorchies, F. Amiranoff, S. Rebibo, G. Hamoniaux, N. Blanchot & J. L. Miquel. *Extending plasma accelerators: guiding with capillary tubes.* IEEE Trans. Plasma Sci. **28**, 1071–1077 (2000)

[27] W. Leemans, B. Nagler, A. Gonsalves, C. Toth, K. Nakamura, C. Geddes, E. Esarey, C. Schroeder & S. Hooker. *GeV electron beams from a centimetre-scale accelerator.* Nat. Phys. **2**, 696–699 (2006)

[28] A. Gonsalves, T. Rowlands-Rees, B. Broks, J. VanDerMullen & S. Hooker. *Transverse Interferometry of a Hydrogen-Filled Capillary Discharge-Waveguide.* Phys. Rev. Lett. **98**, 025002 (2007)

[29] A. G. Litvak. Sov. Phys. JETP **30**, 344 (1969)

[30] C. E. Max, J. Arons & A. B. Langdon. *Self-Modulation and Self-Focusing of Electromagnetic Waves in Plasmas.* Phys. Rev. Lett. **33** (4), 209–212 (1974)

[31] P. Sprangle, C. M. Tang & E. Esarey. *Relativistic self-focusing of short-pulse radiation beams in plasmas.* IEEE Trans. Plasma Sci. **PS-15**, 145–153 (1987)

[32] P. Sprangle, E. Esarey & A. Ting. *Nonlinear theory of intense laser-plasma interactions.* Phys. Rev. Lett. **64** (17), 2011–2014 (1990)

[33] J. Faure, V. Malka, J.-R. Marquès, P.-G. David, F. Amiranoff, K. Ta Phouc & A. Rousse. *Effects of pulse duration on self-focusing of ultra-short lasers in underdense plasmas.* Phys. Plasmas **9**, 756 (2002)

[34] L. Chen, H. Kotaki, K. Nakajima, J. Koga, S. Bulanov, T. Tajima, Y. Gu, H. Peng, X. Wang, T. Wen, H. Liu, C. Jiao, C. Zhang, X. Huang, Y. Guo, K. Zhou, J. Hua, W. An, C. Tang & Y. Lin. *Self-guiding of 100 TW femtosecond laser pulses in centimeter-scale underdense plasma.* Phys. Plasmas **14**, 040703 (2007)

[35] J. Krall, A. Ting, E. Esarey & P. Sprangle. *Enhanced acceleration in a self-modulated-laser wake-field accelerator.* Phys. Rev. E **48** (3), 2157–2161 (1993)

[36] S. P. D. Mangles, T. A. G. R., O. Lundh, F. Lindau, M. C. Kaluza, A. Persson, C.-G. Wahlstr´m, K. Krushelnick & Z. Najmudin. *On the stability of laser wakefield electron accelerators in the monoenergetic regime.* Phys. Plasmas **14**, 056702 (2007)

[37] C. Joshi. *The development of laser- and beam-driven plasma accelerators as an experimental fieldv.* Phys. Plasmas **14**, 055501 (2007)

[38] A. Modena, Z. Najmudin, A. Dangor, C. Clayton, K. Marsh, C. Joshi, V. Malka, C. Darrow, C. Danson, D. Neely & F. Walsh. *Electron acceleration from the breaking of relativistic plasma waves.* Nature **377**, 606–608 (1995)

[39] K. Nakajima, D. Fisher, T. Kawakubo, H. Nakanishi, A. Ogata, Y. Kato, Y. Kitagawa, R. Kodama, K. Mima, H. Shiraga, K. Suzuki, K. Yamakawa, T. Zhang, Y. Sakawa, T. Shoji, Y. Nishida, N. Yugami, M. Downer & T. Tajima. *Observation of Ultrahigh Gradient Electron Acceleration by a Self-Modulated Intense Short Laser Pulse.* Phys. Rev. Lett. **74** (322), 4428–4431 (1995)

[40] A. Amiranoff, F. amd Antonetti, P. Audebert, D. Bernard, B. Cros, F. Dorchies, J. Gauthier, J. Geindre, G. Grillon, F. Jacquet, G. Matthieussent, J. Marquès, P. Miné, P. Mora, A. Modena, J. Morillo, F. Moulin, Z. Najmudin, S. A.E. & C. Stenz. *Laser particle acceleration: beat-wave and wakefield experiments.* Plasma Phys. Control. Fusion **38**, A295 – A300 (1996)

[41] V. Malka, S. Fritzler, E. Lefebvre, F. Aleonard, M.M. Burgy, J. Chambaret, J. Chemin, K. Krushelnick, G. Malka, S. Mangles, Z. Najmudin, M. Pittman, J. Rousseau, J. Scheurer, B. Walton & A. Dangor. *Electron Acceleration by a Wake Field Forced by an Intense Ultrashort Laser Pulse.* Science **298**, 1596–1600 (2002)

[42] W. P. Leemans, P. Catravas, E. Esarey, C. G. R. Geddes, C. Toth, R. Trines, C. B. Schroeder, B. A. Shadwick, J. van Tilborg & J. Faure. *Electron-Yield Enhancement in a Laser-Wakefield Accelerator Driven by Asymmetric Laser Pulses.* Phys. Rev. Lett. **89** (17), 174802 (2002)

[43] J. Faure, Y. Glinec, S. Pukhov, A. andKiselev, S. Gordienko, E. Lefebvre, J. Rousseau, F. Burgy & V. Malka. *A laser-plasma accelerator producing monoenergetic electron beams.* Nature **431**, 541–544 (2004)

[44] C. Geddes, C. Toth, J. van Tilborg, E. Esarey, C. Schroeder, D. Bruhwiler, C. Nieter, J. Cary & W. Leemans. *High-quality electron beams from a laser wakefield accelerator using plasma-channel guiding.* Nature **431**, 538–541 (2004)

[45] S. P. D. Mangles, C. D. Murphy, Z. Najmudin, A. G. R. Thomas, J. L. Collier, A. E. Dangor, E. J. Divall, P. S. Foster, J. G. Gallacher, C. J. Hooker, D. A. Jaroszynski, A. J. Langley, W. B. Mori, P. A. Norreys, F. S. Tsung, R. Viskup, B. R. Walton & K. Krushelnick. *Monoenergetic beams of relativistic electrons from intense laser-plasma interactions.* Nature **431**, 535–538 (2004)

[46] A. Pukhov & J. Meyer-Ter-Vehn. *Laser wake field acceleration: the highly non-linear broken-wave regime.* Appl. Phys. B **74**, 355–361 (2002)

[47] V. Malka, J. Faure, Y. Glinec, A. Pukhov & J. P. Rousseau. *Monoenergetic electron beam optimization in the bubble regime.* Phys. Plasmas **12**, 056702 (2005)

[48] B. Hidding, K. U. Amthor, B. Liesfeld, H. Schwoerer, S. Karsch, M. Geissler, L. Veisz, K. Schmid, J. G. Gallacher, S. P. Jamison, D. Jaroszynski, G. Pretzler & R. Sauerbrey. *Generation of Quasimonoenergetic Electron Bunches with 80-fs Laser Pulses.* Phys. Rev. Lett. **96**, 105004 (2006)

[49] A. Thomas, Z. Najmudin, S. Mangles, C. Murphy, A. Dangor, C. Kamperidis, K. Lancaster, W. Mori, P. Norreys, W. Rozmus & K. Krushelnick. *Effect of Laser-Focusing Conditions on Propagation and Monoenergetic Electron Production in Laser-Wakefield Accelerators.* Phys. Rev. Lett. **98**, 095004 (2007)

[50] S. Bulanov, N. Naumova, F. Pegoraro & J. Sakai. *Particle injection into the wave acceleration phase due to nonlinear wake wave breaking.* Phys. Rev. E **58** (5), R5257–R5260 (1998)

[51] H. Suk, C. Kim, G. H. Kim, I. S. Ko & H. J. Lee. *Energy enhancement in the self-injected laser wakefield acceleration using tapered plasma densities.* Phys. Lett. A **316**, 233–237 (2003)

[52] P. Tomassini, M. Galimberti, A. Giulietti, D. Giulietti, L. Gizzi, L. Labate & F. Pegoraro. *Production of high-quality electron beams in numerical experiments of laser wakefield acceleration with longitudinal wave breaking.* Phys. Rev. ST Accel. Beams **6**, 121301 (2003)

[53] C. G. R. Geddes, K. Nakamura, G. R. Plateau, C. Toth, E. Cormier-Michel, E. Esarey, C. B. Schroeder, J. R. Cary & W. P. Leemans. *Plasma-Density-Gradient Injection of Low Absolute-Momentum-Spread Electron Bunches.* Phys. Rev. Lett. **100**, 215004 (2008)

[54] F. Amiranoff, D. Bernard, B. Cros, F. Dorchies, F. Jacquet, V. Malka, J. R. Marquès, G. Matthieussent, P. Miné, A. Modena & Z. Najmudin.

The laser wakefield acceleration experiment at Ecole Polytechnique. Nucl. Instrum. Methods Phys. Res. A **410** (3), 364–366 (1998)

[55] F. Dorchies, F. Amiranoff, V. Malka, J. R. Marquès, A. Modena, D. Bernard, F. Jacquet, P. Miné, B. Cros, G. Matthieussent, P. Mora, A. Solodov, J. Morillo & Z. Najmudin. *Acceleration of injected electrons in a laser wakefield experiment.* Phys. Plasmas **6** (7), 2903–2913 (1999)

[56] W. H. Urbanus, W. van Dijk, S. B. van der Geer, G. J. H. Brussaard & M. J. van der Wiel. *Front-to-end simulations of the design of a laser wakefield accelerator with external injection.* J. Appl. Phys. **99**, 114501 (2006)

[57] D. F. Gordon, R. F. Hubbard, J. H. Cooley, B. Hafizi, A. Ting & P. Sprangle. *Quasimonoenergetic electrons from unphased injection into channel guided laser wakefield accelerators.* Phys. Rev. E **71** (2), 026404 (2005)

[58] M. J. H. Luttikhof, A. G. Khachatryan, F. A. van Goor & K.-J. Boller. *The effect of the vacuum-plasma transition and an injection angle on electron-bunch injection into a laser wakefield.* Phys. Plasmas **14** (8), 083101 (2007)

[59] D. Giulietti et al. *PLASMONX - Conceptual Design Report.* Technical report, INFN (2005)

[60] URL `http://loasis.lbl.gov`

[61] A. Ting, E. Esarey & P. Sprangle. *Nonlinear wake-field generation and relativistic focusing of intense laser pulses in plasmas.* Phys. Fluids B **2** (6), 1390–1394 (1990)

[62] C. Geddes, C. Tóth, J. van Tilborg, C. Esarey, E.and Schroeder, D. Bruhwiler, C. Nieter, J. Cary & W. Leemans. *Production of high-quality electron bunches by dephasing and beam loading in channeled and unchanneled laser plasma accelerators.* Phys. Plasmas **12**, 056709 (2005)

[63] J. Faure, C. Rechatin, A. Norlin, A. Lifschitz, Y. Glinec & V. Malka. *Controlled injection and acceleration of electrons in plasma wakefields by colliding laser pulses.* Nature **444**, 737–739 (2006)

[64] S. Karsch, J. Osterhoff, A. Popp, T. P. Rowlands-Rees, Z. Major, M. Fuchs, B. Marx, R. Hörlein, K. Schmid, L. Veisz, S. Becker, U. Schramm, B. Hidding, G. Pretzler, D. Habs, F. Grüner, F. Krausz & S. M. Hooker. *GeV-scale electron acceleration in a gas-filled capillary discharge waveguide.* New J. Phys. **9** (11), 415 (2007)

[65] D. Giulietti, M. Galimberti, A. Giulietti, L. Gizzi, R. Numico, P. Tomassini, M. Borghesi, V. Malka, S. Fritzler, M. Pittman, K. TaPhouc & A. Pukhov. *Production of ultracollimated bunches of multi-MeV electrons by 35 fs laser pulses propagating in exploding-foil plasmas.* Phys. Plasmas **9** (9), 3655–3658 (2002)

[66] S. Gordienko & A. Pukhov. *Scalings for ultra-relativistic laser plasmas and monoenergetic electrons.* Phys. Plasmas **12**, 043109 (2005). Http://arxiv.org/e-print/physics/0410268

[67] W. Lu, M. Tzoufras, C. Joshi, F. Tsung, W. Mori, J. Vieira, R. Fonseca & L. Silva. *Generating multi-GeV electron bunches using single stage laser wakefield acceleration in a 3D nonlinear regime.* Phys. Rev. ST Accel. Beams **10**, 061301 (2007)

[68] C. K. Birdsall. *Particle-in-Cell Charged-Particle Simulations, Plus Monte Carlo Collisions With Neutral Atoms, PIC-MCC.* IEEE Trans. Plasma Sci. **19** (2), 65–85 (1991)

[69] D. Giulietti, L. A. Gizzi, A. Giulietti, A. Macchi, D. Teychenné, P. Chessa, A. Rousse, G. Cheriaux, J. P. Chambaret & G. Darpentigny. *Observation of Solid-Density Laminar Plasma Transparency to Intense 30 Femtosecond Laser Pulses.* Phys. Rev. Lett. **79** (17), 3194–3197 (1997)

[70] T. S. Clement, A. J. Taylor & D. J. Kane. *Single-shot measurement of the amplitude and phase of ultrashort laser pulses in the violet.* Opt. Lett. **20** (1), 70–72 (1995)

[71] J. Collier, C. Hernandez-Gomez, R. Allott, C. Danson & A. Hall. *A single-shot third-order autocorrelator for pulse contrast and pulse shape measurements.* Laser Part. Beams **19**, 231–235. (2001)

[72] D. J. Kane & R. Trebino. *Characterization of arbitrary femtosecond pulses usingfrequency-resolved optical gating.* IEEE J. Quantum Electron. **29** (2), 571–579 (1993)

[73] C. Iaconis & I. A. Walmsley. *Interferometry; Ultrafast optics; Pulse shaping; Ultrafast measurementsSpectral phase interferometry for direct electric-field reconstruction of ultrashort optical pulses.* Opt. Lett. **23** (10), 792–794 (1998)

[74] B. K. Garside & T. K. Lim. *Laser mode locking using saturable absorbers.* J. Appl. Phys. **44** (5), 2335–2342 (1973)

[75] M. P. Kalashnikov, E. Risse, H. Schönnagel & W. Sandner. *Double chirped-pulse-amplification laser: a way to clean pulses temporally.* Opt. Lett. **30** (8), 923–925 (2005)

[76] H. C. Kapteyn, M. M. Murnane, A. Szoke & R. W. Falcone. *Prepulse energy suppression for high-energy ultrashort pulses using self-induced plasma shuttering.* Opt. Lett. **16** (7), 490–492 (1991)

[77] G. Doumy. *Interaction laser matière à haut flux et fort contraste temporel.* Ph.D. thesis, Ecole Politechnique (2006)

[78] G. Doumy, F. Quéré, O. Gobert, M. Perdrix, P. Martin, P. Audebert, J. Gauthier, J. Geindre & T. Wittmann. *Complete characterization of a plasma mirror for the production of high-contrast ultraintense laser pulses.* Phys. Rev. E **69**, 026402 (2004)

[79] A. Lévy, T. Ceccotti, P. D'Oliveira, F. Réau, M. Perdrix, F. Quéré, P. Monot, M. Bougeard, H. Lagadec, P. Martin, J.-P. Geindre & P. Audebert. *Double plasma mirror for ultrahigh temporal contrast ultraintense laser pulses.* Opt. Lett. **32** (3), 310–312 (2007)

[80] C. Thaury, F. Quéré, J.-P. Geindre, A. Lévy, T. Ceccotti, P. Monot, M. Bougeard, F. Réau, P. D'Oliveira, P. Audebert, R. Marjoribanks & P. Martin. *Plasma mirrors for ultrahigh-intensity optics.* Nature Phys. **3**, 424–429 (2007)

[81] A. Gamucci, M. Galimberti, D. Giulietti, L. Gizzi, L. Labate, C. Petcu, P. Tomassini & A. Giulietti. *Production of hollow cylindrical plasmas for laser guiding in acceleration experiments.* Appl. Phys. B **85** (4), 611–617 (2006)

[82] A. Gamucci, M. Galimberti, D. Giulietti, L. A. Gizzi, T. Hosokai, L. Labate, C. Petcu, P. Tomassini & A. Giulietti. *Production of plasma channels in gas-jets.* Proceedings of International Conference on Charged and Neutral Particles Channeling Phenomena II, Editor: Sultan B. Dabagov **6634** (1), 66341J (2007)

[83] G. Ostrovskaya & A. Zaidel'. *Laser spark in gases.* Sov. Phys. Uspekhi **16** (6), 834–855 (1974)

[84] M. G. Nomarski. *Microinterféromètre différentiel à ondes polarisées.* J. Phys. Radium **16**, 9S–13S (1955)

[85] R. Benattar, C. Popovics & R. Sigel. *Polarized light interferometer for laser fusion studies.* Rev. Sci. Instrum. **50** (12), 1583–1586 (1979)

[86] M. Born & E. Wolf. *Principles of Optics.* seventh edition. Cambridge University Press, Cambridge, England (1999)

[87] P. Monot. *Interaction laser-gaz en champ intense.* Thèse nouveau doctorat, Université de Paris 11, Orsay, FRANCE (1993). 93 PA11 2239

[88] T. Auguste, M. Bougeard, E. Caprin, P. D'Oliveira & P. Monot. *Characterization of a high-density large scale pulsed gas jet for laser-gas interaction experiments.* Rev. Sci. Instrum. **70**, 2349 (1999)

[89] C. Grey Morgan. *Laser-induced breakdown of gases.* Rep. Prog. Phys. **38**, 621–665 (1975)

[90] S. Soubacq, P. Pignolet, E. Schall & J. Batina. *Investigation of a gas breakdown process in a laser-plasma experiment.* J. Phys. D: Appl. Phys. **37**, 2686–2702 (2004)

[91] P. Tomassini, A. Giulietti, L. Gizzi, M. Galimberti, D. Giulietti, M. Borghesi & O. Willi. *Analyzing laser plasma interferograms with a continuous wavelet transform ridge extraction technique: the method.* Appl. Opt. **40** (35), 6561–6568 (2001)

[92] P. Tomassini & A. Giulietti. *A generalization of Abel inversion to non-axisymmetric density distribution.* Opt. Comm. **199**, 143–148 (2001)

[93] C. G. Durfee III, J. Lynch & H. M. Milchberg. *Mode properties of a plasma waveguide for intense laser pulses.* Opt. Lett. **19** (23), 1937–1939 (1994)

[94] C. G. Durfee III, J. Lynch & H. M. Milchberg. *Development of a plasma waveguide for high-intensity laser pulses.* Phys. Rev. E **51** (3), 2368–2389 (1995)

[95] J. Kim, N. Hafz & H. Suk. *Electron trapping and acceleration across a parabolic plasma density profile.* Phys. Rev. E **69**, 026409 (2004)

[96] Y. B. Zel'dovich & Y. P. Raizer. *Physics of shock waves and high-temperature hydrodynamic phenomena.* Academic Press (1966)

[97] P. Sprangle, B. Hafizi, J. R. Peñano, R. F. Hubbard, A. Ting, A. Zigler & T. M. Antonsen. *Stable Laser-Pulse Propagation in Plasma Channels for GeV Electron Acceleration.* Phys. Rev. Lett. **85** (24), 5110–5113 (2000)

[98] P. Sprangle, B. Hafizi, J. Penano, R. Hubbard, A. Ting, C. Moore, D. Gordon, A. Ziigler, D. Kaganovich & T. Antonsen Jr. *Wakefield generation and GeV acceleration in tapered plasma channels.* Phys. Rev. E **63**, 056405 (2001)

[99] D. Giulietti, A. Giulietti, M. Lucchesi & M. Vaselli. *Intense diffraction of a laser beam due to self-focusing in underdense plasma.* J. Appl. Phys. **58** (8), 2916–2921 (1985)

[100] H. R. Griem. *Principles of plasma spectroscopy.* Cambridge University Press (1974)

[101] S. Dobosz, P. D'Oliveira, S. Hulin, P. Monot, F. Réau & T. Auguste. *Space- and time-resolved density measurements of a high-intensity laser-produced plasma for x-ray laser studies.* Phys. Rev. E **65**, 047403 (2002)

[102] A. Giulietti, M. Galimberti, A. Gamucci, D. Giulietti, L. Gizzi, P. Koester, L. Labate, P. Tomassini, T. Ceccotti, P. D'Oliveira, T. Auguste, P. Monot & P. Martin. *Search for stable propagation of intense femtosecond laser pulses in gas.* Laser Part. Beams **25**, 513–521 (2007). Accepted for publication on Laser Part. Beams

[103] A. Giulietti, P. Tomassini, M. Galimberti, D. Giulietti, L. Gizzi, P. Koester, L. Labate, T. Ceccotti, P. D'Oliveira, T. Auguste, P. Monot & P. Martin. *Prepulse effect on intense femtosecond laser pulse propagation in gas.* Phys. Plasmas **13**, 093103 (2006)

[104] A. M. Perelomov, V. S. Popov & M. V. Terent'ev. *Ionization of Atoms in an Alternating Electric Field.* Sov. Phys. JETP **23**, 924 (1966)

[105] A. M. Perelomov, V. S. Popov & M. V. Terent'ev. *Ionization of Atoms in an Alternating Electric Field: II.* Sov. Phys. JETP **24**, 207 (1967)

[106] A. M. Perelomov & V. S. Popov. *Ionization of Atoms in an Alternating Electrical Field. III.* Sov. Phys. JETP **25**, 336 (1967)

[107] M. Galimberti. *Probe transit effect in interferometry of fast moving samples.* J. Opt. Soc. Am. A **24** (2), 304–310 (2007)

[108] A. Gamucci, N. Bourgeois, T. Ceccotti, S. Dobosz, P. D'Oliveira, M. Galimberti, J. Galy, A. Giulietti, D. Giulietti, . A. Gizzi, D. J. Hamilton, L. Labate, J. R. Marquès, P. Monot, H. Popescu, F. Réau, G. Sarri, P. Tomassini & P. Martin. *Advanced Diagnostics Applied to a Laser-Driven Electron-Acceleration Experiment.* IEEE Trans. Plasma Sci. **36** (4), 1699–1706 (2008)

[109] S. P. D. Mangles, A. G. R. Thomas, M. C. Kaluza, O. Lundh, F. Lindau, A. Persson, Z. Najmudin, C. G. Wahlstr´om, C. D. Murphy, C. Kamperidis, K. L. Lancaster, E. Divall & K. Krushelnick. *Effect of laser contrast ratio on electron beam stability in laser wakefield acceleration experiments.* Plasma Phys. Control. Fusion **48**, B83–B90 (2006)

[110] M. Galimberti, A. Giulietti, D. Giulietti & L. Gizzi. *SHEEBA: A spatial high energy electron beam analyzer.* Rev. Sci. Instrum. **76**, 053303 (2005)

[111] Y. Glinec, J. Faure, A. Guemnie-Tafo, V. Malka, H. Monard, J. Larbre, V. De Waele, J. Marignier & M. Mostafavi. *Absolute calibration for a broad range single shot electron spectrometer.* Rev. Sci. Instrum. **77**, 103301 (2006)

[112] K. Ledingham, P. McKenna & R. Singhal. *Applications for Nuclear Phenomena Generated by Ultra-Intense Lasers.* Science **300**, 1107–1111 (2003)

[113] W. Leemans, D. Rodgers, P. Catravas, C. Geddes, G. Fubiani, E. Esarey, B. Shadwick, R. Donahue & A. Smith. *Gamma-neutron activation experiments using laser wakefield accelerators.* Phys. Plasmas **8** (5), 2510–2516 (2001)

[114] W. Bothe & W. Gentner. *Atomumwandlungen durch γ-Strahlen.* Z. Phys. **106**, 236 (1937)

[115] G. C. Baldwin & G. S. Klaiber. *Photo-Fission in Heavy Elements.* Phys. Rev. **71** (1), 3 (1947)

[116] J. Speth & A. VanDerWoude. *Giant resonances in nuclei.* Rep. Prog. Phys. **44**, 46 (1981)

[117] URL `http://www-nds.iaea.org/photonuclear/`

[118] A. Veyssiere, H. Beil, R. Bergere, P. Carlos & A. Lepretre. *Photoneutron cross sections of ^{208}Pb and ^{197}Au.* Nucl. Phys. A **159** (2), 561–576 (1970)

[119] S. Agostinelli et al. *GEANT4 - a simulation toolkit.* Nucl. Instrum. Methods Phys. Res. A **506** (3), 250–303 (2003)

[120] B. Liesfeld, K.-U. Amthor, F. Ewald, H. Schwoerer, J. Magill, J. Galy, G. Lander & R. Sauerbrey. *Nuclear reactions triggered by laser-accelerated relativistic electron jets.* Appl. Phys. B **79**, 1047–1052 (2004)

[121] H. Schwoerer, F. Ewald, R. Sauerbrey, J. Galy, J. Magill, V. Rondinella, R. Schenkel & T. Butz. *Fission of actinides using a tabletop laser.* Europhys. Lett. **61** (1), 47–52 (2003)

[122] J. Magill, H. Schwoerer, F. Ewald, J. Galy, R. Schenkel & R. Sauerbrey. *Laser transmutation of iodine-129.* Appl. Phys. B **77**, 387–390 (2003)

[123] A. Giulietti, N. Bourgeois, T. Ceccotti, X. Davoine, S. Dobosz, P. D'Oliveira, M. Galimberti, J. Galy, A. Gamucci, D. Giulietti, . A. Gizzi, D. J. Hamilton, E. Lefebvre, L. Labate, J. R. Marquès, P. Monot, H. Popescu, F. Réau, G. Sarri, P. Tomassini & P. Martin. *Intense gamma-Ray Source in the Giant-Dipole-Resonance Range Driven by 10-TW Laser Pulses.* Phys. Rev. Lett. **101** (10), 105002 (2008)

[124] E. Lefebvre, N. Cochet, S. Fritzler, V. Malka, M. Aleonard, J.-F. Chemin, S. Darbon, L. Disdier, J. Faure, A. Fedotoff, O. Landoas, G. Malka, V. Meot, P. Morel, M. Rabec Le Gloahec, A. Rouyer, C. Rubbelynck,

V. Tikhonchuk, R. Wrobel, P. Audebert & C. Rousseaux. *Electron and photon production from relativistic laser-plasma interactions.* Nucl. Fusion **43**, 629–633 (2003)

[125] O. Coulaud, M. Dussere, P. Hénon, E. Lefebvre & J. Roman. *Optimization of a kinetic laser-plasma interaction code for large parallel systems.* Parallel Comput. **29** (9), 1175–1189 (2003)

[126] U. Veronesi, E. Marubini, L. Mariani, V. Galimberti, A. Luini, P. Veronesi, B. Salvadori & R. Zucali. *Radiotherapy after breast-conserving surgery in small breast carcinoma: Long-term results of a randomized trial.* Ann. Oncol. **12** (7), 997–1003 (2001)

[127] Z. Bulhak, S. Kolyga, P. Panta & W. Stachowicz. *Fifteen years of experience in the sterilization of medical products with the linear electron accelerator LAE-13/9.* Int. J. Radiat. Appl. Instrum. Part C **34** (3), 395–397 (1989)

[128] Y. Glinec, J. Faure, L. LeDain, S. Darbon, T. Hosokai, J. Santos, E. Lefebvre, J. Rousseau, F. Burgy, B. Mercier & V. Malka. *High-Resolution gamma-Ray Radiography Produced by a Laser-Plasma Driven Electron Source.* Phys. Rev. Lett. **94**, 025003 (2005)

[129] D. A. G. Deacon, L. R. Elias, J. M. J. Madey, G. J. Ramian, H. A. Schwettman & T. I. Smith. *First Operation of a Free-Electron Laser.* Phys. Rev. Lett. **38** (16), 892–894 (1977)

[130] V. Malka, J. Faure, Y. Gaudel, E. Lefebvre, A. Rousse & K. TaPhouc. *Principles and applications of compact laser-plasma accelerators.* Nature Phys. **4**, 447–453 (2008)

[131] V. Petrillo, L. Serafini & P. Tomassini. *Ultrahigh brightness electron beams by plasma-based injectors for driving all-optical free-electron lasers.* Phys. Rev. ST Accel. Beams **11** (7), 070703 (2008)

[132] F. Grüner, S. Becker, U. Schramm, T. Eichner, M. Fuchs, R. Weingartner, D. Habs, J. Meyer-ter Vehn, M. Geissler, M. Ferrario, L. Serafini, B. van der Geer, H. Backe, W. Lauth & S. Reiche. *Design considerations for table-top, laser-based VUV and X-ray free electron lasers.* Appl. Phys. B **86** (3), 431–435 (2007)

[133] A. Rosi & V. Viti. *Guidelines for intra-operative radiation therapy.* Rapporti ISTISAN 03/1 IT, Istituto Superiore di Sanita' (2003)

[134] L. L. Gunderson, C. G. Willet, F. A. Calvo & L. B. Harrison (Editors). *Intraoperative Irradiation: Techniques and Results.* Humana Press (1999)

[135] C. Chiu, M. Fomytskyi, F. Grigsby, F. Raischel, M. C. Downer & T. Tajima. *Laser electron accelerators for radiation medicine: A feasibility study.* Med. Phys. **31** (7), 2042–2052 (2004)

[136] K. K. Kainz, K. R. Hogstrom, J. A. Antolak, P. R. Almond, C. D. Bloch, C. Chiu, M. Fomytskyi, F. Raischel, M. Downer & T. Tajima. *Dose properties of a laser accelerated electron beam and prospects for clinical application.* Med. Phys. **31**, 2053–2067 (2004)

[137] K. Kinoshita, T. Hosokai, T. Okhubo, A. Maekawa, A. Zhidkov & M. Uesaka. *Development of a laser-driven plasma cathode for medical applications.* Laser Phys. **16** (4), 660–665 (2006)

[138] E. Cartlidge. *Lasers slim down radiotherapy equipment.* Phys. World (2008). URL `http://physicsworld.com/cws/article/news/35891`

[139] M. Martin. *Laser Accelerated Radiotherapy: Is It On Its Way to the Clinic?* J. Natl. Cancer Inst. **101** (7), 450–451 (2009)

[140] M. Karlsson & B. Zackrisson. *Exploration of new treatment modalities offered by high energy (up to 50 MeV) electrons and photons.* Radiother. Oncol. **43** (3), 303–309 (1997)

[141] U. Veronesi, R. Orecchia, A. Luini, L. Galimberti, G. Gatti, M. Intra, P. Veronesi, M. C. Leonardi, M. Ciocca, R. Lazzari, P. Caldarella, N. Rotmensz, C. Sangalli, L. Santos Silvs & D. Sanchez. *Full Dose Intraoperative Radiotherapy With Electrons (ELIOT) During Breast Conserving Surgery - Experience with 1246 Cases.* ecancermedicalscience **2**, 65 (2008)

[142] URL `http://www.sordina.com`

[143] F. Ewald. *Laser-Triggered Nuclear Reactions.* Lect. Notes Phys. **694**, 25–45 (2006)

[144] M. J. Berger & S. M. Seltzer. *Bremsstrahlung and photoneutrons from thick tungsten and tantalum targets.* Phys. Rev. C **2**, 621 (1970)

[145] K. Boyer, T. S. Luk & C. K. Rhodes. *Possibility of optically induced nuclear fission.* Phys. Rev. Lett. **60** (7), 557–560 (1988)

[146] T. E. Cowan, A. W. Hunt, T. W. Phillips, S. C. Wilks, M. D. Perry, C. Brown, W. Fountain, S. Hatchett, J. Johnson, M. H. Key, T. Parnell, D. M. Pennington, R. A. Snavely & Y. Takahashi. *Photonuclear Fission from High Energy Electrons from Ultraintense Laser-Solid Interactions.* Phys. Rev. Lett. **84** (5), 903–906 (2000)

[147] K. Ledingham, I. Spencer, T. McCanny, R. Singhal, M. Santala, E. Clark, I. Watts, F. Beg, M. Zepf, K. Krushelnick, M. Tatarakis, A. Dangor, P. Norreys, R. Allott, D. Neely, R. Clark, A. Machacek, J. Wark, A. Cresswell & J. Sanderson, D.C.W. Magill. *Photonuclear Physics when a Multiterawatt Laser Pulse Interacts with Solid Targets.* Phys. Rev. Lett. **84** (5), 899–902 (2000)

[148] S. Reed, V. Chvykov, G. Kalintchenko, T. Matsuoka, P. Rousseau, V. Yanovsky, C. Vane, J. Beene, D. Stracener, D. Schultz & A. Maksimchuk. *Photonuclear fission with quasimonoenergetic electron beams from laser wakefields.* Appl. Phys. Lett. **89**, 231107 (2006)

[149] K. Ledingham, J. Magill, P. McKenna, J. Yang, J. Galy, R. Schenkel, J. Rebizant, T. McCanny, S. Shimizu, L. Robson, R. Singhal, M. Wei, S. Mangles, P. Nilson, K. Krushelnick, R. Clarke & P. Norreys. *Laser-driven photo-transmutation of 129I - a long-lived nuclear waste product.* J. Phys. D: Appl. Phys. **36**, L79–L82 (2003)

[150] *Handbook on Nuclear Activation Data.* Technical Report Series Vol. 273, IAEA, Vienna (1987)

[151] R. Michel, T. Ernst, D. Jakob, K. Klipsch, S. Szidat, H.-A. Synal & C. Schnabel. *Long-lived radionuclides in the environment: The case of Iodine-129.* In *Proceedings of the Forum for Nuclear Safety EUROSAFE, Nov. 4-5, 2002, Berlin* (2002)

[152] T. Ruth. *Accelerating production of medical isotopes.* Nature **457**, 536–537 (2009)

[153] G. A. Mourou, T. Tajima & S. V. Bulanov. *Optics in the relativistic regime.* Rev. Mod. Phys. **78**, 309–371 (2006)

[154] I. H. Hutchinson. *Principles of plasma diagnostics.* 2nd edition. Cambridge University Press (2002)

[155] A. Raven & O. Willi. *Electron-Density Structures in Laser-Produced Plasmas at High Irradiances.* Phys. Rev. Lett. **43** (4), 278–282 (1979)

[156] M. Takeda, H. Ina & S. Kobayashi. *Fourier-transform method of fringe-pattern analysis for computer-based topography and interferometry.* J. Opt. Soc. Am. **72** (1), 156–160 (1982)

[157] K. Nugent. *Interferogram analysis using an accurate fully automatic algorithm.* Appl. Opt. **24** (18), 3101–3105 (1985)

[158] L. Gizzi, D. Giulietti, A. Giulietti, T. Afshar-Rad, V. Biancalana, P. Chessa, C. Danson, E. Schifano, S. Viana & O. Willi. *Characterization*

of laser plasmas for interaction studies. Phys. Rev. E **49** (6), 5628–5643 (1994)

[159] W. C. Lang & K. Forinash. *Time-frequency analysis with the continuous wavelet transform.* Am. J. Phys. **66** (9), 794–797 (1998)

[160] R. A. Carmona, W. L. Hwang & B. Torresani. *Characterization of signals by the ridges of their wavelet transforms.* IEEE Trans. Signal. Process. **45** (10), 2586–2590 (1997)

[161] P. Tomassini, A. Giulietti, L. Gizzi, R. Numico, M. Galimberti, D. Giulietti & M. Borghesi. *Application of novel techniques for interferogram analysis to laser-plasma femtosecond probing.* Laser Part. Beams **20**, 195–199 (2002)

[162] M. Galimberti. *Sviluppo e analisi dati del rivelatore per elettroni veloci SHEEBA.* Technical Report 1/092001, Intense Laser Irradiation Laboratory, IPCF-CNR, Area della Ricerca CNR, Via G. Moruzzi 1, 56124 Pisa, Italy (2001)